IMPLEMENTATION AND EVALUATION OF 4D DIGITAL SUBTRACTION ANGIOGRAPHY AND 4D FLUOROSCOPY WITH VIRTUAL ENDOSCOPIC DISPLAY

by

Brian Joseph Davis

A dissertation submitted in partial fulfillment of the

requirements for the degree of

Doctor of Philosophy

(Biomedical Engineering)

at the

UNIVERSITY OF WISCONSIN - MADISON

2023

Date of oral examination: 13-Dec-2023

The dissertation is approved by the following members of the Final Oral Committee:

Michael A. Speidel, PhD., Associate Professor, Medical Physics

Justin Williams , PhD., Professor, Biomedical Engineering

Christopher Brace, PhD., Associate Professor, Biomedical Engineering

Wally Block, PhD., Professor, Medical Physics and Biomedical Engineering

Paul Laeseke, MD, PhD, Associate Professor, Radiology

Acknowledgments

I want to thank Charles A. Mistretta and Charlie Strother for their role in the conception of the 4D DSA technique and for their critical role in guiding this research. I also specifically thank Michael A Speidel, who has been instrumental in guiding the development of 4D-Virtual Fluoroscopy and 4D-Virtual Endoscopy, without whom the completion of this thesis would not have been possible. Additionally, I would like to thank Charles A. Mistretta for his patience and instruction and for providing an opportunity for me to grow intellectually from a 1D signal processing background to 2D, 3D, and, ultimately, 4D image processing. Though I have stated many times in the course of this research, "If only I would have chosen a 0D research topic many moons ago, I could have done it before I started".

I also would like Erick L. Oberstar for the many ideas and fruitful conversations resulting in many methods and ways to investigate problems and find solutions. Clinical data was provided by Charlie Strother, David Niemann, Beverly Aagaard-Keintz, Paul F. Laeseke, and Azam Ahmed of the University of Wisconsin-Madison. Phantom development was made possible with the help of Gary R. Frank of the Medical Physics Department Machine Shop and Instrument Lab. I would also like to acknowledge the contributions of Siemens Medical Solutions Gmbh for providing the preprocessing and forward projection software. I want to thank the contributions and numerous discussions with Michael Speidel, Erick Oberstar, Martin Wagner, Gabe Shaughnessy, Katrina Ruedinger, Michael Hughes, Lindsay Bodart, David Rutkowski, Markus Kowarschik, Kevin Royalty, and Sebastian Schafer, who aided in the development and research of 4D-DSA and 4D-Endoscopic View.

I would also like to thank my wife, Monica, sister, Heather Davis, and parents, Joe and Penny Davis, for their support and encouragement over the years and for allowing many back-of-the-head discussions to occur while I hovered over a laptop.

I especially want to thank Lori Davis, who always pursued and supported continuing education, and me, who was taken too soon from this earth. While science in healthcare has solved and cured many medical conditions, there are still those that still elude the scientific and medical community, sadly, both in treatment

and even in diagnosis in a timely manner. It has been my experience that certain aspects of the medical system require an overhaul.

Research reported in this effort was supported by the National Heart, Lung, and Blood Institute (NHLBI) of the National Institutes of Health under award number R01HL116567. The content is solely the responsibility of the author and does not necessarily represent the official views of the National Institutes of Health.

Abstract

Neurointerventional radiology procedures rely on contrast-enhanced Digital Subtraction Angiography (DSA) and x-ray fluoroscopy to diagnose vascular disease and guide catheter-based interventional devices. The complexity of these tasks ideally demands time-resolved 3D (4D) x-ray imaging techniques that have been traditionally difficult to achieve. This work reports the practical implementation and evaluation of 4D-DSA and 4D-Fluoroscopy, techniques which have been proposed to overcome the limitations of conventional 2D and 3D interventional x-ray imaging.

4D-DSA applies a novel reconstruction scheme to a conventional 3D-DSA rotational scan protocol to produce a temporal sequence of 3D images of the patient vasculature. A temporal volume is produced for each time point in the rotational acquisition by backprojecting the contrast information from each 2D frame onto a thresholded version of the 3D-DSA image. The 4D-DSA technique was implemented with a sparse GPU-based backprojector to achieve sub-second volume reconstruction (0.79 sec/volume) and total reconstruction time for all volumes in less than 27 seconds. The sparse backprojection reduced both RAM and persistent memory required to store the data. The spatial resolution of 4D-DSA evaluated with a wire phantom was similar to that of 3D-DSA.

4D-Fluoroscopy performs real-time 3D reconstruction of catheter devices based on the two x-ray fluoroscopy views from a bi-plane system. The device reconstruction is displayed relative to a vascular roadmap generated from a 3D-DSA. Rendering formats include Virtual Endoscopic Display, which provides a device-following viewpoint from inside the vessel, and External View, which uses an external rotatable viewpoint. A prototype system was developed and evaluated to demonstrate feasibility and utility. The prototype produced real-time 3D reconstructions of catheters and guidewires at the rate of x-ray imaging (15 frame/s). The 4D-fluoroscopy system was evaluated in a study asking participants to perform catheter navigational tasks in a 3D printed vascular phantom. In a questionnaire, users reported using 4D displays more often than 2D displays, and users preferred the 4D Virtual Endoscopic Display over the 4D External View. 4D-DSA and 4D-Fluoroscopy provide new and potentially useful methods for the time-resolved 3D visualization of patient vasculature and catheter based devices.

Contents

[1] The revised and adapted contents of this chapter have been previously published in the following journal article: Davis, Brian J. and Oberstar, Erick and Royalty, Kevin and Schafer, Sebastian and Mistretta, Charles, "Volumetric limiting spatial resolution analysis of four-dimensional digital subtraction angiography", Journal of Medical Imaging 3, 1 (2016), pp. 013503--013503.[1]

[2] Portions of this chapter have been previously published in the following journal article: Davis, Brian J., Martin G. Wagner, Sarvesh Periyasamy, Charles A. Mistretta, Charles M. Strother, Paul F. Laeseke, and Michael A. Speidel. “Evaluation of Real-Time Guidewire Navigation Using Virtual Endoscopic 4D Fluoroscopy.” In Medical Imaging 2020: Image-Guided Procedures, Robotic Interventions, and Modeling, 11315:1131515. International Society for Optics and Photonics, 2020. https://doi.org/10.1117/12.2549683.

[3]Portions of this chapter have been previously published in the following journal article: Davis, Brian J., Martin G. Wagner, Sarvesh Periyasamy, Charles A. Mistretta, Charles M. Strother, Paul F. Laeseke, and Michael A. Speidel. "Evaluation of Real-Time Guidewire Navigation Using Virtual Endoscopic 4D Fluoroscopy." In Medical Imaging 2020: Image-Guided Procedures, Robotic Interventions, and Modeling, 11315:1131515. International Society for Optics and Photonics, 2020. https://doi.org/10.1117/12.2549683.

List of Figures

List of Tables

1 Introduction to 4D-DSA and 4D-Fluoroscopy

1. Introduction

Approximately 1 in 10,000 persons in the United States will suffer from a subarachnoid hemorrhage as a result of a ruptured intracranial aneurysm[4]. This equates to approximately 27,000 affected people per year. Intracranial aneurysms are diagnosed and treated with minimally-invasive catheter-based techniques in the neurointerventional radiology suite. Typically, this involves coiling a platinum wire inside the aneurysm, which is then separated from the guide wire by application of an electric current. Neurosurgery or clipping is an alternative to coiling but is a more invasive procedure with higher risk[5]. The interventional x-ray angiography system is the system of choice for providing image guidance during the treatment of intracranial aneurysm, and other vascular diseases, such as arterial vascular malformation (AVMs), arterial stenosis, and stroke. These systems provide digital subtraction angiography (DSA) diagnostic imaging of contrast-enhanced vessels[6] and real-time x-ray fluoroscopy to navigate of catheter devices, such as coils, wires, angioplasty balloons, and stents. Modern x-ray systems in the neurointerventional radiology suite are bi-plane, consisting of two C-arms. In addition to providing time-resolved 2D imaging with one or both C-arms, these systems can perform a 3D rotational scan with a single C-arm to provide a static 3D image.

In procedures involving complex vascular anatomy, ideally the x-ray system would provide time-resolved 3D imaging capability for visualization of patterns of blood flow from any desired angle. However, current systems require a trade-off: one can either view time-resolved 2D images in a fixed angle (2D-DSA) or a 3D vasculature image from any angle but with no temporal resolution (3D-DSA). The interventionalist must mentally fuse these disparate acquired data sets to obtain a diagnostic evaluation of the patient's health, perform an intervention, and finally determine if the procedure was successful. 4D-DSA[7] is a recently introduced technique that combines the strengths of time-resolved 2D imaging and static 3D imaging into a single cohesive 4D (3D+time) image. 4D-DSA can be used for qualitative visualization of patterns of blood flow. Additionally, it has the potential to provide quantitative metrics of blood flow related to the outcome of the interventional procedure[8].

A similar problem exists during the device navigation phases of an interventional procedure. When the operator advances a catheter or wire through a complex vascular network, real-time imaging is limited to 2D projection views from one or both C-arms. A static 2D vessel roadmap can be superimposed on live imaging of the device; however, there may be considerable vessel overlap in a 2D projection of the actual 3D vessel tree. 4D fluoroscopy is a proposed new approach that fuses the two datasets and provides the interventional neuroradiologist with a means to navigate the vascular network with potentially increased efficiency [9]. Based on live 3D reconstruction of a catheter device from the two live 2D image streams provided by a bi-plane x-ray system, 4D-fluoroscopy can also provide views that are not currently possible, such as a virtual endoscopic display.

2. Objective

This dissertation aims to fill gaps in the angiographic suite that limit a neuroradiologist's ability to perform tasks as efficiently as possible. These gaps include the need for 1) diagnostic temporal views of the dynamics of the vascular network under study and 2) real-time 3D + time fluoroscopic navigation. This dissertation first describes the design and implementation of a 4D-DSA prototype. The prototype was then used to demonstrate that reconstruction times are feasible, provide acceptable image quality, and provide utility to the interventional neuroradiologist. The dissertation then describes the design and development of a prototype 4D-fluoroscopy with a virtual endoscopic display system providing virtual road maps with device overlay, device tracking, endoscopic views, and path planning. Participants were then asked to evaluate the system by performing a series of device navigation tasks through multiple paths of a complex neurovascular phantom. The objectives and quantitative outcomes of this work are:

1. Detailed design and development of a prototype system for 4D-DSA reconstructions utilizing GPGPU based software codes and the evaluation of the performance, memory, and storage requirements.
2. Determination of a key image quality metric of volumetric spatial resolution using the developed 4D-DSA software.
3. Detailed design and development of a 4D-fluoroscopy with endoscopic display system prototype with device tracking, navigation, and path planning features with discussion on key metrics of frame rate and latency the system can obtain.
4. Evaluation of the performance of the fully integrated real-time 4D-fluoroscopy with endoscopic display system prototype with device tracking, virtual road map, navigation, and path planning features by participants performing navigational tasks.

3. Chapter Descriptions

This dissertation has been divided into seven chapters. Chapter 1 is a brief synopsis of the current state of the art and prior work that has been done regarding 4D-DSA and 4D-fluoroscopy with endoscopic display. Chapter 2 provides a more detailed background on the prior work. Chapter 3 details the design considerations, implementation, and performance of 4D-DSA algorithms that satisfy the timeliness requirements of patient care. Chapter 4 details the volumetric spatial resolution performance of 4D-DSA and discusses the methods for determining the spatial resolution. 4D-fluoroscopy is described in Chapter 5, including the software requirements, design, and performance metrics including those relating to the the virtual endoscopic view software. An evaluation of the 4D-fluoroscopy prototype in a real time navigational task is presented in Chapter 6. Chapter 7 concludes the dissertation with a summary of conclusions and potential future directions for both 4D-DSA and 4D-fluoroscopy with endoscopic display.

2 Background

1. Interventional Diagnosis and Treatment of Neurovascular Disease

Minimally-invasive approaches to the diagnosis and treatment of neurovascular disease require intraprocedural imaging for the visualization of vascular structures and patterns of blood flow, and real-time imaging of the endovascular devices used to perform the procedures. These procedures are performed in an x-ray angiography suite, which offers rapid real-time acquisition, high spatial resolution, wide field-of-view, ease of imaging through anatomic structures, and compatibility with wires, catheters, and other devices. Digital Subtraction Angiography (DSA), first introduced in 1980[10, 11, 12, 13, 14], was a key technical facilitator. This advancement provided the ability to see anatomy projected in two dimensions and record the passage of an injected contrast agent through the blood vessels. Importantly, since DSA image formation involved subtraction of a pre-contrast ("mask") image from all later contrast-enhanced images, vessels could be visualized without distracting overlapping background anatomy (bones, tissues, etc.), facilitating treatment of aneurysms, arterial stenosis, ischemic stroke, and arteriovenous malformations (AVMs). The real-time digital processing platform implementing DSA also enabled other important features. For example, it was possible to retain the last image acquired in a frame buffer (capture-and-hold). This featured allowed the contrast injection and x-ray exposure to cease while still retaining the last image for viewing and resulted in decreased radiation and contrast dose to the patient. Recent advances have have led to the ability to perform time of arrival analysis providign a color view of the contrast enhancement of a series of sequential 2D DSA images from a fixed view angle[15].

In 1997, 3D volumetric reconstruction of a series of C-arm CT projections was made possible[16, 17]. The technique, referred to as C-arm cone-beam CT (C-arm CBCT), consists of a rotational acquisition followed by CT reconstruction using an algorithm designed for cone-beam geometry. The related technique of 3D DSA uses two rotational acquisitions: 1) a "mask" rotation acquired without injected contrast agent and 2) a "fill" rotation acquired with contrast agent. Mask projections are logarithmically subtracted from the fill projections prior to CT reconstruction, yielding a 3D volume of the contrast-enhanced vessels only. This

advance provided the interventional radiologist the ability to rotate a vascular network and obtain any view angle without further injection of contrast medium or x-ray dose, including gantry angles unobtainable by the C-arm system hardware. 3D-DSA does not portray the temporal dynamics present in the 2D rotational acquisitions; visualization of the temporal dynamics in a 3D view has remained unobtainable until recently.

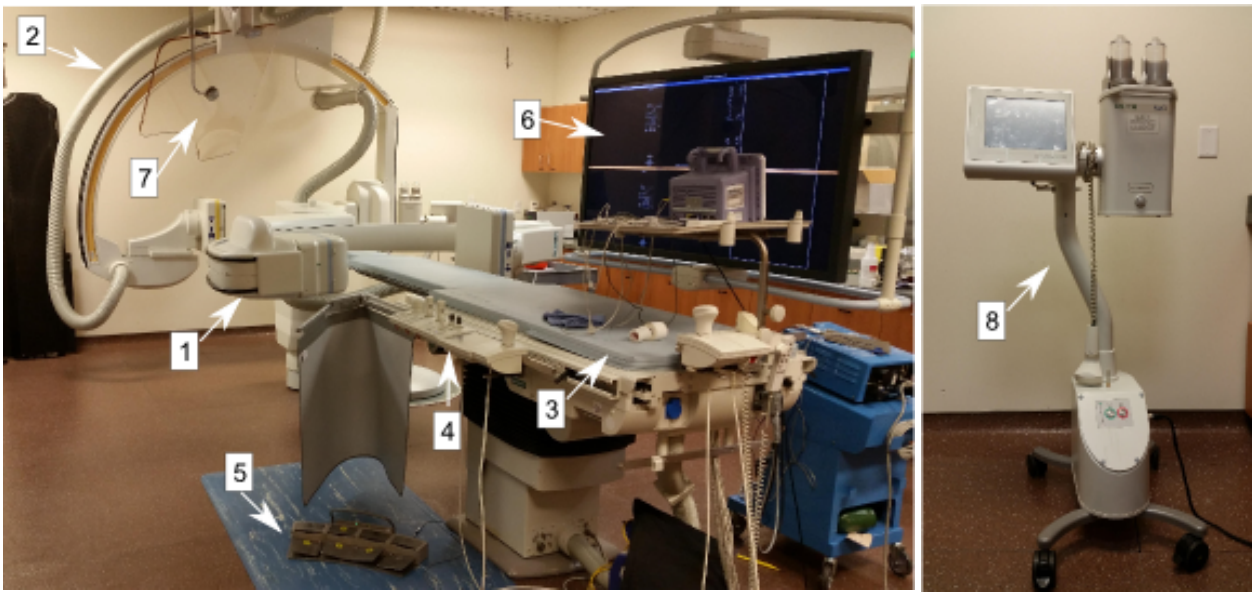

(a) Artis Zee Biplane System **(b)** Contrast and Saline Injector

Figure 2.1: Artis zee (Siemens Healthcare, Forchheim Germany) biplane unit shown in figure a) above with 1) plane-A (foreground) in patient position and 2) plane-B (background) in retracted position, 3) patient couch, 4) couch and plane orientation controls, 5) fluoroscopy capture foot pedals, 6) monitor, and 7) x-ray shield. Also shown is the 8) saline and contrast injector as shown in figure b

The modern interventional x-ray angiography system consists of a patient couch (table), one (single plane) or two (biplane) C-arms, a tableside human machine interface (HMI) for control, monitors for viewing the x-ray images and system status, foot pedals for activation of the image acquisition system(s), and an operator station in the control room. An example of a biplane system is shown in figure 2.1. Each C-arm has a high power x-ray tube on one end and a flat panel x-ray detector at the other. The patient couch provides a rigid radiolucent platform to support the patient between x-ray tube and detector. The patient is typically placed in the head first supine position, though patient orientation is flexible and procedure specific. The couch provides the capaiblility to the radiologist to move the patient to various positions in relation to the C-arm. Location of the HMI at the patient table allows for direct interaction with the system and patient, while providing close proximity of the controls to the radiologist when performing an intervention or catheter placement for diagnostic assessment. C-arms can be freely rotated to various view angles as long as the C-arms do not collide with the patient or couch and the limits of rotation are not reached. Static positioning of one or both C-arms is used for 2D imaging. If both C-arms are used simultaneously then the 2D images

are conventionally displayed side-by-side on the in-room monitors. 3D rotational acquisition utilizes a single floor-mounted C-arm. The operator station in the control room allows the reconstruction of 3D volumes from the 2D projections acquired in the rotational scan. Software also allows measurement of various metrics such as vessel length, diameter, and other parameters.

The C-arm x-ray system can be used for diagnostic or interventional use. Diagnostic use typically includes placement of a catheter and injection of contrast medium to assess patient health. Interventional use includes coil deployment, stent placement, thrombolysis/thrombectomy, and other interventional operations. The primary modes of operation for an interventional x-ray angiographic systems are: 2D radiography, 2D fluoroscopy, 2D digital subtraction angiography (2D-DSA), volumetric computed tomography (3D imaging), and 3D-DSA[18, 19]. 2D-DSA and 3D-DSA are considered the gold standard[20, 21] in the assessment and treatment of vascular diseases, excluding procedures in the heart, where motion artifacts preclude the use of DSA. For both catheter placement during diagnostic assessment or during an intervention, road maps[22] are created. A roadmap is created by performing short injection of contrast to opacify the vessel network. The live image of the device (without contrast enhanced vessels) is then subtracted from the roadmap to produce a display of both device and vessel positions. Biplane x-ray angiography systems allow for device guidance in particularly complicated 3D anatomy (e.g. cerebral vasculature). An operator of a biplane system can infer where the device is in three dimensions based on two separate live projection images.

The 3D capabilities of an interventional x-ray angiography system are CT-like but differ from conventional diagnostic CT in important ways. The C-arm rotation time for a 3D acquisition mode ranges from 5 to 20 seconds for a single rotation and more than double this for a 3D-DSA acquisition requires two rotations. The C-arm gantry system requires offline calibration[23, 24, 25]using a calibration phantom to account for the mechanical instability of the gantry. 3D-DSA works well when there is little or no patient motion or where registration algorithms can compensate for motion. However, motion during acquisition can cause artifacts in the appearance of contrast-enhanced vessels and misregistration of mask and fill projections. A 3D-DSA provides a single static image volume and a view of the vascular network from any angle. The 2D-DSA provides the temporal information of contrast enhanced blood flow through a vascular network. The combination of these feature sets eluded industry and the scientific community for quite some time[26]. One approach to adding temporal resolution to 3D interventional imaging is to perform multiple sweep acquisition. For example, Ganguly et. al.[27] reported a method with up to 6 bidirectional C-arm sweeps. Although this approach is straightforward, it demands long total acquisition times, provides relatively slow temporal dynamics, and can potentially increase radiation dose compared to 3D-DSA. In 2010 4D-DSA and 4D-Fluoroscopy were introduced[7]. 4D-DSA, in contrast to other methods, aims to achieve temporally-resolved

3D imaging from a conventional 3D-DSA style acquisition. The speed up in acquisition relative to standard multi-sweep approaches is made possible by the sparsity of vascular structures in 3D-DSA imaging. This sparsity allows a novel reconstruction strategy in which a 3D image volume is reconstructed for every single 2D projection image in the scan. Similarly, 4D-Fluoroscopy aims to provide live 3D device reconstructions by exploiting sparsity of the object (e.g. catheter). 4D-Fluoroscopy generates 3D reconstructions from just two biplane views. The live 3D device reconstructions are displayed relative to a static 3D-DSA of the vascular anatomy, in a manner analogous to displaying a conventional 2D device image relative to a static 2D vascular roadmap. Both techniques promise to bring new dimensions of imaging to the interventional suite using existing x-ray hardware.

2. Overview of 4D-DSA

4D DSA requires x-ray images of the subject acquired in two subsequent C-arm rotations, the first performed without contrast injection (mask) and the second performed with contrast injection (fill). The injection protocol is described in figure 2.2. The mask sweep is first acquired to capture the anatomy and vascular network. An injector delay, inserted before the fill sweep begins, prevents the vasculature from fully opacifying before the fill sweep begins. The fill sweep then captures the anatomy and dynamics of the contrast agent as it flows through the network. In a preprocessing step, angle-by-angle log subtraction of mask and fill images yield a set of 2D projections p as the source data for 4D DSA reconstruction. At the angle θ_i

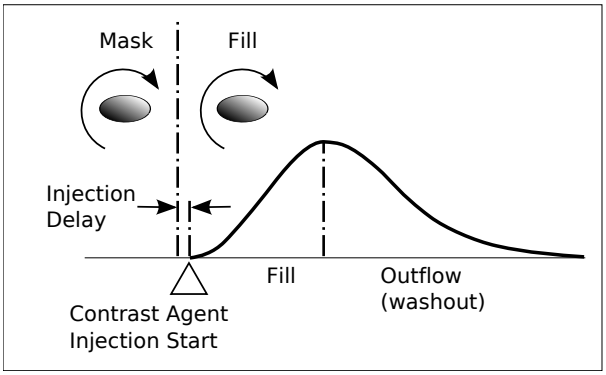

Figure 2.2: Modified injection protocol diagram showing the mask sweep, contrast injection start, and fill sweep. The ideal constraining image is generated form late projections provided the injection protocol provides the required number of frames.

$$p(t_i) = ln(p_{mask}(\theta_i)) - ln(p_{fill}(\theta_i))$$

where t_i is the time corresponding to angle θ_i in the fill rotation. The 4D DSA reconstruction then performs the following steps. First a standard 3D filtered back projection reconstruction algorithm f_{FBP} is applied to obtain a conventional 3D DSA volume displaying the contrast enhanced vascular anatomy. Second, an

intensity threshold f_{th} is applied to yield a sparse constrain image which is ideally non-zero only at the positions of the vessels. Using functions $f(.)$ to represent reconstruction and thresholding operations, the 3D constraining volume is given by

$$C(x, y, z) = f_{th}(f_{FBP}(p(t_1), p(t_2), p(t_3), \ldots, p(t_N)))$$

Next, a 3D weighting volume is generated for each time t_i. The purpose of a weighting volume is to provide multiplicative scaling factors at each voxel position to modify the intensities in the constraining volume so that they correspond to the intensities that existed at time t_i. Several approaches to forming the weighting volume have been reported[28, 19]. In the most basic method, the single 2D projection image for time t_i is normalized by a forward projection of the constraining volume at the angle θ_i This ratio of 2D projections is formed by

$$r(t_i) = \frac{p(t_i) * k_B}{p_C(\theta_i) * k_B} \tag{2.1}$$

where p_C is a forward projection of the constraining volume and k_B is a small blurring kernel used to reduce noise in the projection data with the convolution operator $*$. The weighting volume W for time t_i is then formed by unfiltered back projection of the single ratio image:

$$W(x, y, z, t_i) = f_{BP}(r(t_i))$$

Finally, the 4D DSA volume at time t_i is formed by element-wise multiplication of arrays using the Hadamard product operation $\circ$ of the constraining volume and the weighting volume:

$$I(x, y, z, t_i) = C(x, y, z) \circ W(x, y, z, t_i) \tag{2.2}$$

Variants of this method differ primarily in how the weighting volume is derived. In one method, termed the adjusted ratio method, the numerator is increased empirically by a small fraction of the maximum value of the blurred constrain image.

$$r(t_i) = \frac{p(t_i) * k_B}{p_C(\theta_i) * k_B + 1.05 \times max(p_C(\theta_i) * k_B)} \tag{2.3}$$

4D-DSA is made possible by combining the 3D-DSA volume and the 2D rotational projections containing

temporal information using the 4D-DSA algorithm described in figure 2.3. Constraining image reconstruction algorithms[29] allow for temporal modulation of a static constraining image without the requirement of the Nyquist sampling rate[26] thus decreasing the acquisition time while maintaining or even improving the signal-to-noise ratio (SNR).

The single projection used to obtain temporal information may contain vessel overlap, leading to image artifacts such as false retrograde filling. Several algorithms were developed to combat this problem. The first algorithm developed beyond the basic 4D-DSA single projection (SP) equation 2.2 was the separation angle (SA) algorithm. The variable τ is a temporal offset specified as a projection angle offset. The algorithm trades temporal resolution to mitigate the overlap artifact by taking a projection at the current angle, t_i, and a future angle, $t_{i+\tau}$, thus generating two weighting volumes are multiplied and the square root taken. The result of the square root operation thus approximates the desired value. Ideally, if the two weighting volumes are equal, the resulting values are only that of a single weighting volume. In practice, this is typically not the case. The SA algorithm is described by the equation:

$$\begin{aligned} I_{SA}(x,y,z,t_i) &= \sqrt{C(x,y,z) \circ W(x,y,z,t_i) \circ C(x,y,z) \circ W(x,y,z,t_{i+\tau})} \\ &= C(x,y,z) \circ \sqrt{W(x,y,z,t_i) \circ W(x,y,z,t_{i+\tau})} \end{aligned} \tag{2.4}$$

Experience with the SA algorithm indicated that further refinements were needed. This led to the development of the minimum within a search angle (MSA) algorithm. The term, $t_{min}(t_i)$, represents a 3D volume and results in finding the minimum value for each TAC on a per voxel basis over the temporal range of $t_i \ldots t_{i+\tau}$. The *argmin* operator selects the minimum value in the voxel TAC for each voxel over the time range specified using the 4D TAC data generated by the 4D-DSA reconstruction process, i_{4D}. The process yields a 3D volume, i_{MSA}, at time t_i. As the temporal index approaches the last projection the variable τ is allowed to approach zero. Again, temporal resolution is traded for signal recovery of the TAC during periods of vessel overlap. When MSA or SA algorithms are used, the temporal resolution can degrade to the worst-case time between the projections of 0.5 seconds typically[26].

$$t_{min}(x,y,z,t_i) = \underset{t' \in [t_i \ldots t_{i+\tau}]}{argmin} \left(I(x,y,z,t')\right) \tag{2.5}$$

$$I(x,y,z,t_i)_{MSA} = C(x,y,z) \circ \left(I(x,y,z,t_{min}(x,y,z,t_i)\right) \tag{2.6}$$

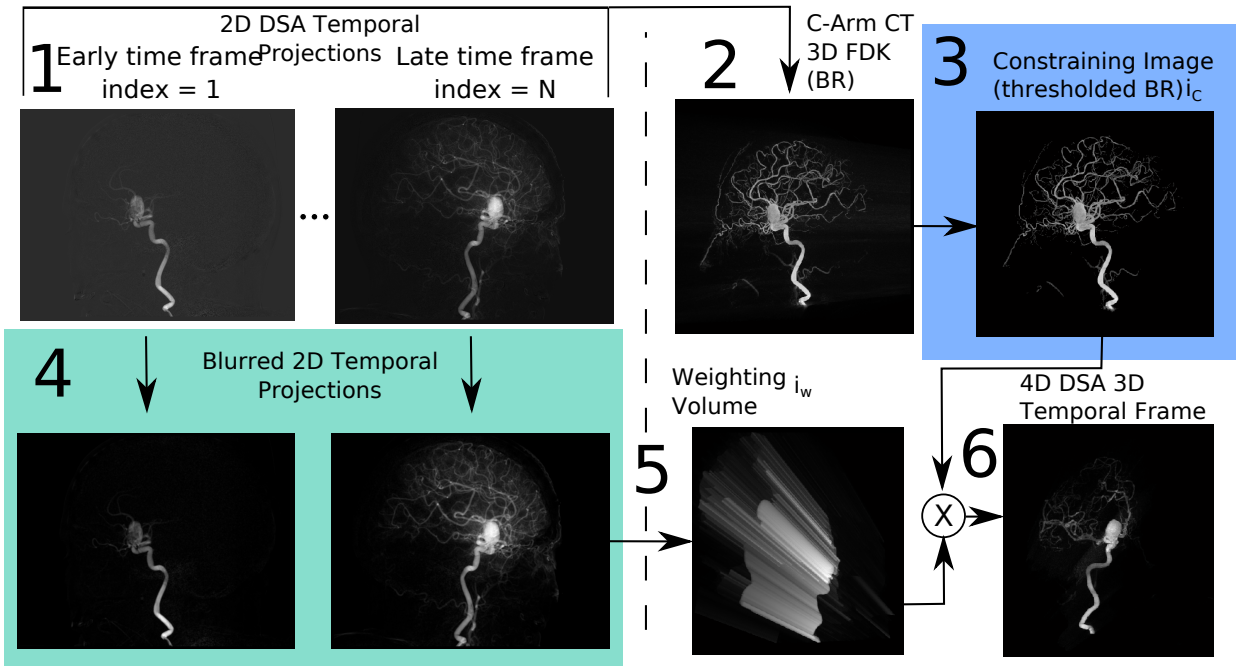

Figure 2.3: The 4D reconstruction process illustrates the projection space on the left of the dashed line and the 3D space on the right. The projections are first acquired in step 1. The volume is then reconstructed from projections as shown in step 2. Constraining image generation by which the 3D-DSA is thresholded is shown in step 3. The 2D blurring kernel is applied to the temporal projections and reprojection (not shown) of the constraining volume in step 4. The blurred temporal projections and reprojections are then divided (not shown). The normalized projections are then backprojected individually to create a weighting volume for each time frame, step 5, and the result is multiplied by the constraining image shown in step 6. The selector uses the time index, t_i, to select which projection to be backprojected to generate the weighting volume. The multiplication step activates voxels that are active in the time frame while leaving the remaining voxels inactive.

Investigations into 4D-DSA have shown that the temporal information can be useful in decreasing the visible complexity of vascular network by only showing early arterial or late venous vessels, as demonstrated by figure 2.4a. A study[30] of arteriovenous malformations imaged with 4D-DSA indicated that 4D-DSA provided superior visualization compared to 2D and 3D DSA. Specifically, this study demonstrated that visualization of the sequence of filling and draining and the various aspects of the AVM including venous obstruction, aneurysms, and fistula is possible. 4D-DSA provides temporal views of the vascular network without physical restrictions imposed by C-arm angle with an example shown in figure 2.4b. The capability to render difficult to obtain C-arm views helps minimize the x-ray dose and contrast agent dose that would normally be spent on additional acquisitions. Wagner et al.[31] investigated the application of 4D-DSA to the thorax and abdomen. Shaughnessy[8] et al. proposed a method for quantitative flow measurement utilizing 4D-DSA data. 4D-DSA aims to fix some of the deficiencies of 2D-DSA and 3D-DSA, as detailed in Forkert et. al.[32]

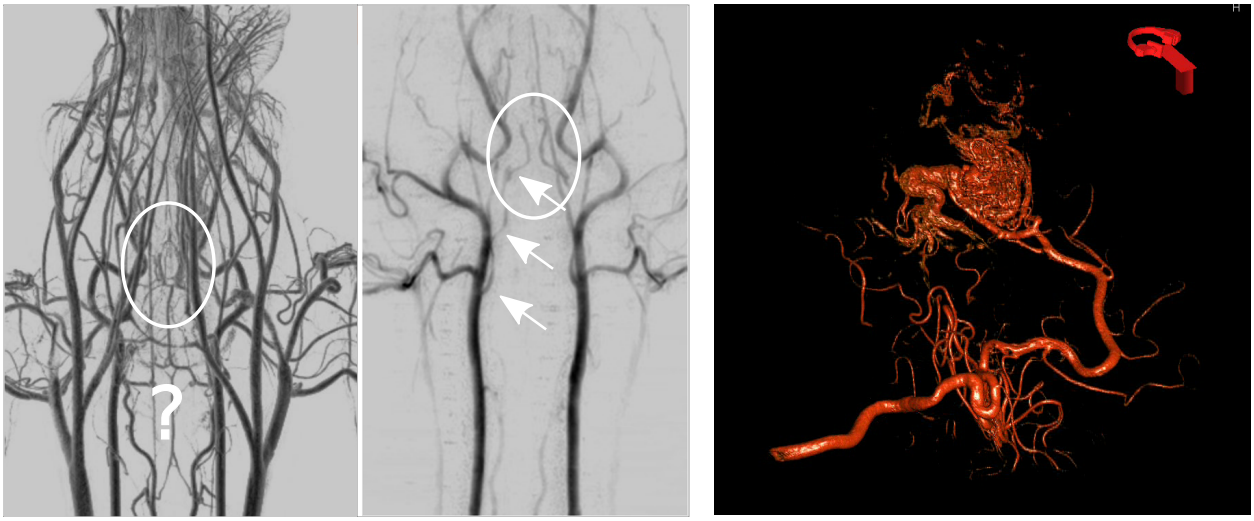

(a) **(b)**

Figure 2.4: a) On the left of the figure above is a 3D-DSA of a canine with vessels fully opacified[2]. Shown on the right is a 4D-DSA early time frame before the opacification of the venous return vessels. The 4D-DSA time frames provide an unobstructed view of arterial vessels. The presence of the veins obscures visualization of the internal carotid arteries (ICAs) in the 3D-DSA. White arrows highlight the course of the right ICA, which is clearly visible in the 4D-DSA view. The ellipse in the 3D-DSA highlights the distal segments of the ICAs for reference. Both 3D-DSA and 4D-DSA reconstructions can be viewed from any angle. However, only 4D-DSA can be viewed at any time. b) Image of an AVM processed by the 4D-DSA prototype provided by Siemens Medical Solutions Gmbh showing an otherwise unobtainable view made possible by using 4D-DSA. The red gantry icon indicates that the view is unobtainable by the gantry. However, 4D-DSA makes the view possible.

3. Overview of 4D-Fluorocopy and 4D Virtual Endoscopic Display

Neurointerventional radiology procedures involve the endovascular guidance of catheter devices through complex 3D cerebral vasculature. A biplane x-ray angiography system, capable of two simultaneous and typically orthogonal 2D projections of a patient, is a vital feature of the modern neurointerventional radiology suite. The two 2D views assist with the guidance task. However, the interventionalist is still left with the challenging problem of determining the 3D location of the catheter in relationship to the vascular anatomy provided only 2D fluoroscopic views and potentially a separate static 3D-DSA. It is left to the performing physician to mentally fuse these disparate information sources while performing a real-time navigational task. Complicating the task is the possibility that the view angle of the 2D projections may be sub-optimal, requiring the physician to physically reorient the C-arms, inject contrast to create 2D roadmaps at the new view angles, and then perform x-ray fluoroscopy at the new view angle(s). This iterative process requires additional time, contrast agent dose, and radiation dose to the patient.

Additionally, an optimal view angle[33] can be unobtainable due to the physical constraints of the system. When both C-arms of a biplane system are in use, there is potential for collision between the two C-arms,

the patient, and the couch. Certain view angles, such as pure superior-inferior projections, are impossible due to the C-arm's limited mechanical range of rotation. These view angles can result in a collision with the patient and increased radiation dose due to the large projected thickness in such orientations. Finally, it should be noted that even though the procedures are endovascular intrinsically, no commercially available systems provide an endoscopic view from within the vascular lumen to assist with the navigational task.

4D-Fluoroscopy aims to provide real-time 3D device visualization in any desired view angle and with potentially reduced use of contrast media[34, 19, 30, 35]. The two bi-plane fluoroscopy views are processed to obtain a real-time 3D reconstruction of curvilinear devices such as guidewires and catheters during the live navigation phase of the 4D fluoroscopy technique. The device is then displayed relative to a registered 3D vascular roadmap obtained from an intraprocedural 3D-DSA. Two methods of rendering the 3D information were implemented: 1) virtual endoscopic display and 2) external viewpoint display.

The virtual endoscopic display renders the lumen and interior wall of the vessel with the virtual camera positioned near the device tip and oriented towards the device tip with typically distal (depending on device orientation) views of the vessel provided. This display method is one of the subjects of the present work. Examples of navigating bifurcations from the viewpoint of the catheter tip are shown in figures 2.5a and 2.5b. The endoscopic mode can also provide a path plan or "yellow-brick-road"[36] feature highlighting the desired preplanned navigational path and endpoint location. It also allows the operator to pause, manipulate the camera view to "look around" the device site, and record internal views of vascular structures for diagnostic analysis. The external viewpoint provides a 3D roadmap view of the external vasculature with a device overlay, ensuring the complete device location is always visible regardless of the view angle. A "glass pipe" rendering allows the viewer to see the catheter device through a semi-transparent vascular network using the alpha blending technique, as shown in figure 2.5c. Both types of display provide a virtual 3D road map without the necessity of contrast injection and with flexibility in viewpoint[37]. It should be noted that 4D-fluoroscopy with a virtual endoscopic display is not meant to supplant conventional 2D-DSA but to augment existing display modes and provide operators with options for challenging navigational tasks.

The original implementation of 4D-Fluoroscopy was based on the backprojection of two simultaneous 2D projections [38]. It was soon discovered that this algorithm could cause 3D "replication artifacts" when the interventional device bends back on itself and self-overlaps in the 2D projections[38]. Generally, these artifacts arise from the attempt to use a CT-like backprojection algorithm, which tends to have high angular sampling requirements for complex objects. The current approach for 4D-Fluoroscopy is based on an epipolar reconstruction approach[39], which has been investigated by others[39, 40, 41, 42, 43, 44, 45, 46]. This algorithm amounts to 3D triangulation of each device point from 2D views, resulting in a 3D representation

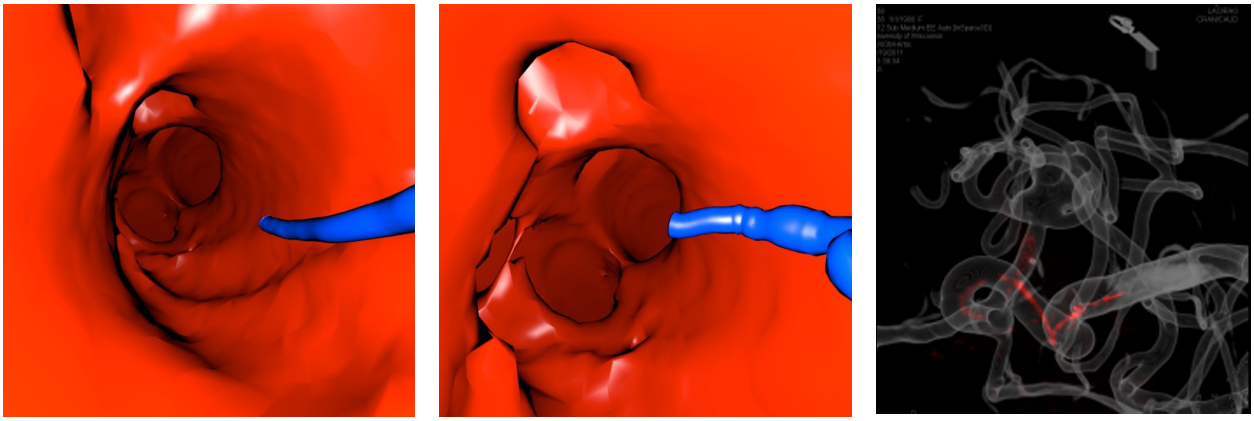

(a) (b) (c)

Figure 2.5: 4D-Fluoroscopy and 4D-Endoscopy mock-up views. a) Virtual endoscopic view of a virtual catheter nearing a bifurcation[3]. b) Virtual endoscopic view of a virtual catheter at a bifurcation[3]. c) 4D-Fluoroscopy glass pipe view of vessel network and virtual catheter shown red.

of the device centerline. During the reconstruction phase, the centerline is first extracted from plane A and plane B. Point correspondences are identified in the two 2D views, and a 3D centerline is then calculated using epipolar geometry. The device radius is also derived at each point along the centerline (if the radius is not manually specified). With the knowledge of the 3D coordinates of the device centerline and device radius, the rendering of the 3D surface of the device is then performed. It should be noted that this approach is not immune from the replication artifact without further processing to determine the most probable device representation.

The concept of virtual endoscopy has been used to explore diagnostic CT and MR scans. Application areas include spinal surgery[37, 47, 48, 49, 38], virtual colonoscopy[50, 51, 52, 37], and virtual exploration of pediatric congenital heart defects[53]. Endoscopic rendering of a 3D dataset simulates the viewpoint that is natural for examining internal structures and guidance of devices through these structures. For example, the study by Li-Ping Yao et al.[53, 54] used data gathered by diagnostic CT to investigate a common congenital heart defect, Tetralogy of Fallot (TOF). This work included a path-planning feature based on an operator-selected start and end points. The present system of 4D fluoroscopy with virtual endoscopic display builds on this basic concept of virtual endoscopy by 1) employing intraprocedural 3D DSA to generate the 3D vascular roadmap, 2) adding a live 3D reconstruction of the catheter device based on live biplane fluoroscopy, 3) rendering the 3D image scene from the viewpoint of the device tip, as it is advanced in real time, and 4) providing a multi-point path-planning feature. The last feature, multi-point path-planning, is needed for complex vascular networks because, as stated by a research colleague and interventional radiologist Dr. Charles Strother, “the shortest path may not be the desired path.” In addition to providing a natural viewpoint from the device’s perspective, the virtual endoscopic display addresses a

basic problem in live 3D image guidance: tasks performed in a 3D space must be formatted for the human visual system, which is best described as 2D or 2D stereo. Other approaches have been developed for combining 3D information into live image guidance. Söderman et al. [34] reported a 2D overlay method consisting of a reprojected 3D road map image in superposition with a live 2D fluoroscopic image. Similar fluoroscopic overlay approaches are now offered in commercially available x-ray angiography systems. A common feature of these approaches is that they fuse a color overlay with the grayscale fluoroscopy image, which introduces the potential for obscured device features, and the information displayed is restricted to the 2D fluoroscopic viewpoint dictated by the current C-arm orientation. In contrast, a virtual endoscopic display visually separates the 3D roadmap and 3D device information and does not restrict viewpoint. This thesis presents the implementation and integration of the components needed to create a full-featured and working real-time 4D fluoroscopy / endoscopic system.

4. Summary

The goal of this chapter was to provide the reader with a background and prior work leading up to the development of 4D-DSA and 4D-fluoroscopy with endoscopic display. The following chapters describe the design and implementation of a 4D-DSA prototype system, testing of the resolution of 4D-DSA as compared to 3D DSA, design and implementation of a 4D fluoroscopy system with endoscopic display, performance testing of the 4D fluoroscopy system, and finally conclusions with discussions of future work of the research.

3 4D-DSA Design and Implementation

1. Introduction

4D-DSA can potentially provide relevant and important diagnostic temporal information to the diagnostic and interventional radiologist. Providing this time series of images to the radiologist in a timely manner is of critical importance if 4D-DSA is to be of any utility. This chapter aims to elaborate on the technical details of the 4D-DSA reconstruction process and to demonstrate the reconstruction is possible, reconstruction times are acceptable, and once the data is available (reconstructed) that, it is of acceptable size to save in offline persistent storage systems such as hard drive or PACS. The motivation here is to shed light on a topic that has not been discussed in the detail necessary to understand the 4D-DSA reconstruction process fully. Various important topics shall be discussed, including the procedural steps of the reconstruction process, time and space (random access memory/persistent memory) requirements, reconstruction algorithms, accelerated parallel computing (GPGPU) hardware requirements, and algorithms; the need for a sparse 4D-DSA sparse backprojector and associated data structure (4D-DSA sparse reconstruction); and post-processing of the sparse reconstruction data set. While in Copland et al. [55] and Schmitt[56, 57], the math equations support a voxel-wise calculation, it is unclear whether or not a true sparse backprojector was implemented and from the reconstruction times of six (6) hrs and as stated in Copland[55] that improvement to the approach could be obtained by implementing the algorithms in CUDA it does not appear that a sparse backprojector was developed.

2. Methods

Early reconstruction times for 4D-DSA were not on the order necessary for utilization in the angio suite, for human patient use, or even research purposes for that matter, nor were the requirements on data storage acceptable. Later, a GPU implementation using a NVIDIA Tesla c1060 and CUDA codes allowed 30 fps, making feasible real-time calculations and rendering and thus useful for diagnostic purposes. The first method

investigated in 4D-DSA is known as the Backproject-Backproject (BPBP/BP^2) method. While this early method allowed 30 fps and research to progress, it still suffered from an inability to save the data compactly. As the name implies, this method requires at least two multiplies per 4D-DSA time frame. The separation angle (SA) approach and the minimum within a search angle (MSA) approach require several backprojections. The simplest form is mathematically shown for the separation angle in equation 2.4. SA and MSA algorithms were first developed using the BP^2 method and ultimately reimplemented using the sparse backprojection method. While fast operation can be obtained for small numbers of backprojections, the BP^2 approach suffers as the number of desired backprojections per frame increases. The approach also required each time frame volume to be either calculated on the fly or saved to disk. Keeping all volumes in memory or accessible by disk is not possible due to RAM and disk speed limitations for real time viewing using this approach. Due to the time and space constraints of performing the BP^2 method and storing the results, it became clear that an alternate approach of implementing the sparse backprojection would need to be pursued. The basic steps of 4D-DSA reconstruction are i) 3D DSA reconstruction, ii) Constraining volume generation, and iii) 4D-DSA time frame generation. Each step is described below, detailing the implementation and acceleration. This section will begin with a discussion of the reconstruction implementation and end with a discussion of the software architecture.

2.1 Reconstruction Implementation

2.1.1 3D DSA Reconstruction

Reconstruction of a 3D DSA is implemented in a voxel-driven filtered backprojection scheme, following the method of cone-beam CT reconstruction defined in Wiesent et al.[25] The starting point of reconstruction is a series of 2D projection images $p_\theta(u,v)$, acquired at incremental angles and having log-normalized, background-subtracted projection values p defined at discrete detector coordinates (u,v). The projection images are multiplied by cosine weights $w_{cos}(u,v)$ and Parker weights $w_{par,\theta}(u,v)$, and then the result is filtered along lines perpendicular to the axis of rotation. Representing the filtering operation with $h_{filt}\{...\}$, the filtered projection value q at position (u,v) and angle theta, θ, is

$$q_\theta(u,v) = h_{filt}\{p_\theta(u,v)w_{cos}(u,v)w_{par,\theta}(u,v)\} \tag{3.1}$$

For a given angle θ, the voxel-driven backprojection to a voxel position (x,y,z) is achieved through a three-step process. First, the point (x,y,z) is forward projected to the (u,v)-detector plane using a projection matrix

P_θ. The projection matrix for an angle θ defines a 3D-to-2D perspective transformation; these matrices are determined during pre-procedure system calibration [58][24][23]. Working in homogeneous coordinates, the $(x, y, z, 1)$-coordinate for the voxel is multiplied by P_θ to obtain a (u', v', w')-vector at the desired angle θ, and then the u' and v' values are divided by w' to obtain the $(u, v, 1)$-coordinate on the detector plane:

$$\begin{bmatrix} u' \\ v' \\ w' \end{bmatrix} = P_\theta \times \begin{bmatrix} x \\ y \\ z \\ 1 \end{bmatrix}$$

$$\begin{bmatrix} u \\ v \\ 1 \end{bmatrix} = \frac{1}{w'} \left(\begin{bmatrix} u' \\ v' \\ w' \end{bmatrix} \right) \tag{3.2}$$

The (x, y, z) coordinates of the voxels exist on a Cartesian grid with user-defined spacing. As such, there is no guarantee that the (u, v) coordinate computed by equation 3.2 will fall directly on one of the discrete (u, v)-coordinates of the filtered projection image defined by equation 3.1. Therefore, the second step of voxel-driven backprojection is to perform interpolation of the filtered projection values q_θ given the point (u, v) from equation 3.2. A variety of interpolation schemes are possible, including nearest neighbor, bilinear, and higher-order methods [59]. Keeping the notation general and using F_{q_θ} to represent the interpolant function for the filtered projection data q_θ, the interpolated projection value at point (u,v) is given by

$$q'_\theta(u, v) = F_{q_\theta}(u, v) \tag{3.3}$$

The third step is to assign the value of equation 3.3 to the (x, y, z) voxel that was originally traced forward in equation 3.2 and apply a multiplicative distance weighting factor $w_{dist,\theta}(x, y, z)$ for the voxel that accounts for beam divergence. Representing the reconstructed 3D image volume as V, the backprojection of q'_θ for a single angle θ is given by:

$$V_\theta(x, y, z) = q'_\theta(u, v) w_{dist,\theta}(x, y, z) = q'_\theta(u = u(x, y, z), v = v(x, y, z)) w_{dist,\theta}(x, y, z) \tag{3.4}$$

where the last part of equation 3.4 simply shows explicitly that the (u, v)-coordinates in the q'_θ function were initially determined from the (x, y, z) coordinates via the matrix transformations in equation 3.2. The

complete 3D DSA reconstruction is obtained by summing the result of equation 3.4 over all the projection angles theta and normalizing by the number of projections N_θ:

$$V(x,y,z) = \frac{1}{N_\theta} \sum_\theta V_\theta(x,y,z) \tag{3.5}$$

2.1.2 3D DSA Implementation and Acceleration Details

The projection filtering stage equation 3.1 used a hann filtering kernel. Filtering was implemented as frequency-domain multiplication with the filter transfer function rather than spatial-domain convolution. Furthermore, nearest neighbor averaging was used as the interpolation scheme as shown in equation 3.3 as $F_{q_\theta}(u,v)$. The backprojection stage (equations 3.2-3.5) was accelerated by exploiting the fact that in a voxel-driven scheme, the result at position (x,y,z) is not dependent on the results from any neighboring voxels. Therefore, in the GPU implementation, each (x,y,z) point had a GPU streaming processor thread, and backprojection occurred in parallel. Storage and indexing of volumetric data can be achieved by using three integer indices $[i,j,k]$ for the (x,y,z) coordinates, where the integer-indexed structure is related to equation 3.5 by

$$V^{'}[i,j,k] = V(x = i\Delta x, y = j\Delta y, z = k\Delta z) \tag{3.6}$$

and $(\Delta x, \Delta y, \Delta z)$ are the specified voxel dimensions. Likewise, the integer indices can be used to store 2D projection data with known detector element spacing $(\Delta u, \Delta v)$. To facilitate the data compression scheme used with 4D-DSA, volumetric data was represented as a single vector with a linear index i. For a volume with $Nx \times Ny \times Nz$ voxels, the mapping from linear index i to the real-world coordinate system (x,y,z) is defined in the following steps:

$$\text{Step 1: } slice_{dim} = N_x \times N_y \tag{3.7}$$

$$\text{Step 2: } z = \frac{i_{lin}}{slice_{dim}}$$

$$\text{Step 3: } j_{lin} = i_{lin} - (z_j * slice_{dim})$$

$$\text{Step 4: } y = \frac{j_{lin}}{N_y}$$

$$\text{Step 5: } x = j_{lin} \,\%\, N_x$$

with conversion back to the voxel index given by,

$$i_{lin} = z \times N_x \times N_y + y \times N_x + x$$

The vectorized representation of volume V with linear index i is referred to with the notation $V[i]$.

2.1.3 Constraining volume generation

The goal of constraining volume generation is to segment the 3D DSA into vascular and non-vascular voxels and set non-vascular voxels to zero. This step limits the voxel positions for which a 4D-DSA can have non-zero values. By applying a threshold to the 3D-DSA volume V, a constrain volume C is generated according to,

$$C(x,y,z) = \left\{ \begin{array}{cc} V(x,y,z) & V(x,y,z) > v_{th} \\ 0 & otherwise \end{array} \right\}, \tag{3.8}$$

where v_{th} represents the threshold value.

2.1.4 Constraining volume implementation and acceleration details

The threshold value v_{th} can be either user-specified or automatically generated. The percent area under the histogram was used with a fixed value for the automatic approach. If a user-specified threshold is chosen, the user can view the constrain volume via sagittal, coronal, and transverse MIP views as the threshold value v_{th} is adjusted. As with the 3D DSA, operations with the constraining volume employ a vectorized representation with linear voxel index:

$$C[i] = \left\{ \begin{array}{cc} V[i] & V[i] > v_{th} \\ 0 & otherwise \end{array} \right\}, \tag{3.9}$$

In a typical 3D DSA, a large fraction of the voxels are non-vascular. A sparsified representation is employed to avoid wasting memory on the storage of zeros for non-vascular voxels. Given the set of linear indices corresponding to the voxel positions,

$$I = 1, 2, 3, \ldots, N_{vox}, \tag{3.10}$$

a sparse set of indices is defined as

$$I_S = i \,|\, i \in I, V[i] > v_{th}, \tag{3.11}$$

and the sparsified constraining volume is

$$C[j] = C[j], j \in I_S \tag{3.12}$$

The CUDA compatible Thrust[60] library was used to implement the selection of indices given a threshold. The binary function (set_index_by_threshold) performs this step, returning 0 or the index value if the value is greater than the threshold at the index. The function was then used in a call to the thrust transform function, which provided the voxel data and indices. The index data would then contain values greater than zero where the threshold criteria were met. The index data was then filtered to remove zeros by performing a stable sort by key value (thrust::stable_sort_by_key) followed by a unique by key(thrust::unique_by_key) on the array indices data again utilizing the thrust API. This resulted in a linear array of voxel indices and voxel values at those voxel index locations. The values were saved to disk as 16-bit integers by employing thrust::minmax_element to find the min and max of the linear array to allow window and leveling of the data to the range 0-4095 (12-bit).

2.1.5 4D-DSA time frame volumes

The basic concept of 4D-DSA is to produce a sequence of volumes for times t by multiplying the 3D constraining volume with a backprojection of the 2D temporal information encoded in the projections acquired at times t. Working in Cartesian coordinates, if the constraining volume is $C(x, y, z)$, and $W(x, y, z, t)$ is the 'weighting volume' obtained by backprojection of 2D temporal information at time t, then the 4D-DSA images are given by

$$I(x,y,z,t) = C(x,y,z)W(x,y,z,t) \tag{3.13}$$

Formation of a weighting volume W for angle $\theta(t)$ begins with dividing the measured 2D projection $p_{\theta(t)}$ by the numerical forward projection $p_{C,\theta}$ of the constraining volume C for the same angle. The division process is stabilized by convolving each projection with a small blurring kernel k_B before division. The resulting ratio of projections,

$$r_{\theta(t)}(u,v) = \frac{p_{\theta(t)}(u,v) * k_B(u,v)}{p_{C,\theta}(u,v) * k_B(u,v)} \tag{3.14}$$

is a measure of how the projection values measured at time t (and angle $\theta(t)$) compare to the numerical projection through the time-averaged constraining volume. This ratio image is backprojected across the (x,y,z) positions to produce the weighting volume. Since the goal is to obtain a volume of weights that will modify the intensities in the constraining volume, the backprojection is performed without a distance weighting, i.e.

$$W_{\theta(t)}(x,y,z) = f_{BP}(r_{\theta(t)}(u = u(x,y,z), v = v(x,y,z))) \tag{3.15}$$

2.1.6 4D-DSA implementation and acceleration details

The filtration step described in equation 3.14 was implemented in frequency space. The blurring kernel operation was implemented using a 5 x 5 pixel square kernel on the projection data with a pixel spacing of 0.3080 mm, resulting in a 1.540 mm wide square, and was implemented using the conv2 function in MATLAB. Following the approach outlined for the constraining volume, the weighting volume is stored as a vector of values $W_{\theta(t)}[i]$ with linear voxel indices, and a sparse set of indices is employed to avoid wasting storage of weighting values for voxels where the constraining volume is zero-valued. The linearized and sparsified weighting volume is

$$W_{S,\theta(t)}[j] = W_{\theta(t)}[j], j \in I_S \tag{3.16}$$

With the sparsified representation of constraining and weighting volumes, the entire 4D-DSA reconstruction can be stored in a compact table where the columns correspond to the indices $j \in I_S$ of the non-zero elements of the image volume, the first row stores the sparse constraining image values $C_s[j]$, and the

subsequent rows correspond to the sparse weighting image values $W_{S,\theta(t)}[j]$ at times t. An example is shown in Table 3.1 in section 2.2.1. To retrieve the full, non-sparse 4D-DSA volume for any chosen time t, the sparse constraining volume row is retrieved, the sparse weighting volume row for time t is retrieved, the two rows are multiplied elementwise, and the result is assigned to a non-sparse vector at the linear indices j in a new table corresponding to the algorithm (SP, SA, or MSA) being performed. The vectorized volume can also be converted back to a 3D volume. Converting from a linear array of indices and values at the locations to a 3D volume is straightforward. First, allocate memory for the 3D volume and select indices or convert form indices to x, y, z coordinates within the volume and set the values defined by the steps starting with equation 3.7.

2.2 Software Architecture

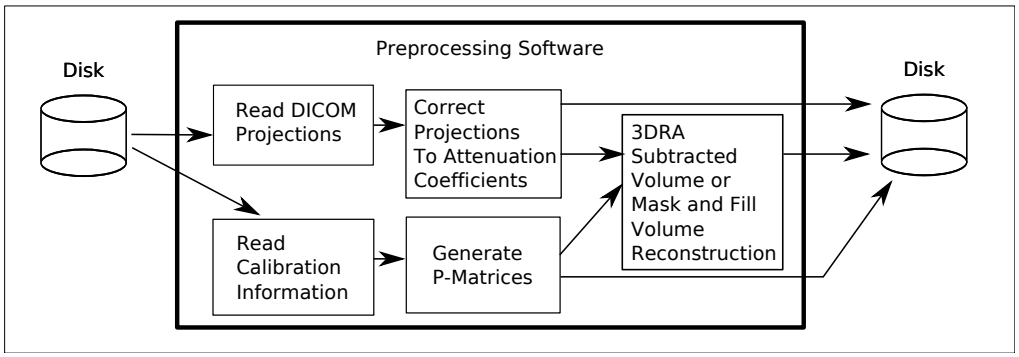

Figure 3.1: Siemens Preprocessing Software Diagram.

The first reconstruction stage consists of generating a 3D DSA volume using vendor-provided software, as shown in figure 3.1. The projection data, calibration p-matrices, and optionally the 3D volume, then enters the 4D-DSA Sparse reconstruction pipeline. A software block diagram of the remaining portions of the 4D reconstruction pipeline is shown in figure 3.2. The steps to create a 4D-DSA sparse data set are as follows. 1) Acquire 2D temporal rotational projections. 2) Reconstruct a 3D DSA constraint volume. 3) Threshold the 3D constrain volume. 4) Create a sparse constrain image. 5) Generate the 4D projections. 6) Perform a Sparse 4D-DSA reconstruction using the 4D projections to generate the raw temporal volume data. 7) Finally, the 4D-DSA overlap correction algorithms are applied to the Sparse 4D-DSA raw data.

The reconstruction process can be broken down into tasks performed on the GPU and CPU. These tasks can also be grouped into categories that are part of the 3D reconstruction and those that are part of the 4D reconstruction. This breakdown is shown in the 3D and 4D reconstruction tasks outlined below.

- 3D Recon

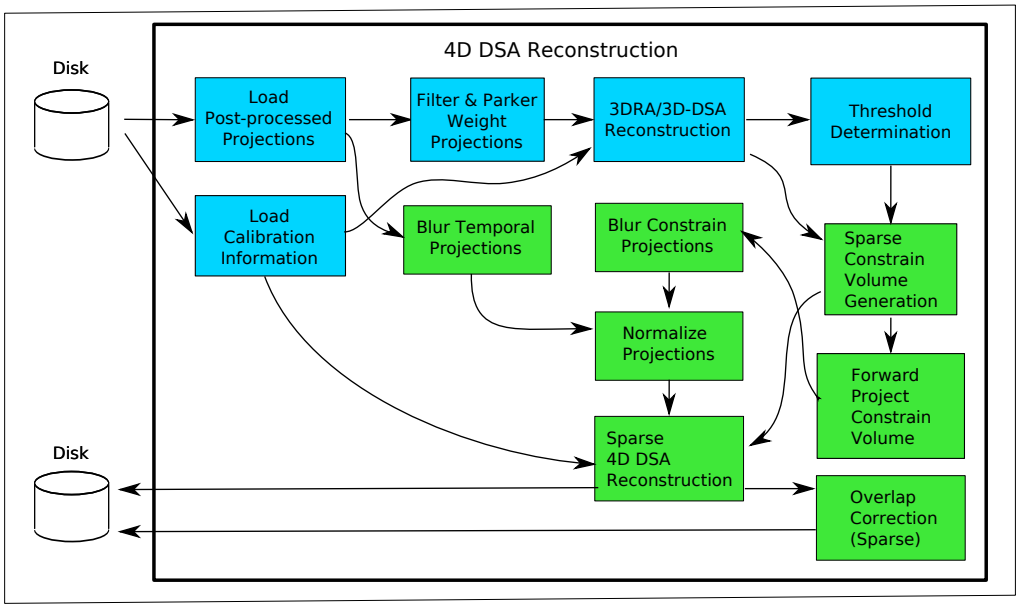

Figure 3.2: 4D-DSA Sparse Reconstruction Software Block Diagram. Shown blue are the typical 3D-DSA steps and shown green are the 4D-DSA steps.

- Pixel Averaging (GPU): Nearest neighbor pixel averaging and decimation.
- FFT Filtering (GPU): Projection filtering as described by equation 3.1
- Backprojection (GPU): Backprojection step as described by equation 3.5

- 4D Recon
  - 4D Projection Generation
    - Blur Projections: Blurring operation as described by k_B in equation 3.14
    - Normalize Projections: The division by the forward projection of the constrain projection shown in equation 3.14
  - Generate Sparse Constrain Volume
    - Find Min and Max of Constrain (GPU): The thrust API call thrust::minmax_element is used
    - Active Voxel Indices Search (GPU): See discussion of set_index_by_threshold, transform, stable_sort_by_key and unique_by_key in section 2.1.4
    - Window and Level (GPU): First thrust::min_max_element then thrust::transform and implementing a user-defined window_level function passed into the transform call.
  - Sparse Temporal Data Generation
    - Find Min and Max of Temporal Data (GPU): The thrust API call thrust::minmax_element is used
    - Active Voxel Indices Search (GPU): See discussion of set_index_by_threshold, transform, stable_sort_by_key and unique_by_key in section 2.1.4

- Sparse Backprojection (GPU): See equation 3.16
- Generate sparse 4D-DSA data set (GPU): The Sparse Backprojector is iteratively called filling in a table of weighting volumes.

- Overlap Correction
  - Single Projection Algorithm (SP) (CPU): See section 2.
  - Separation Angle Algorithm (SA) (CPU): See section 2.
  - Minimum Search Angle Algorithm (MSA) (CPU): See section 2.

2.2.1 Sparse Constrain Table

Table 3.1: 4D-DSA data storage format example. For each time index (row), the image values are stored only at the voxel indices (column headers), which are members of the constraining volume (non-zero values). The constrain volume is stored first and followed by the sparse backprojections of the 4D projections.

	Voxel Index						
Temporal Index	5	23	56	...	117128541	117339666	117494219
Constrain	1.23	3.02	6.35	...	23.98	87.08	6.24
1	3.16	0.61	1.15	...	1.59	2.28	2.89
2	0.89	2.02	1.35	...	0.98	1.08	0.24
3	2.68	0.02	1.63	...	1.64	2.89	1.55
4	0.84	0.54	1.88	...	1.38	3.10	1.94
...	2.92	1.68	0.70	...	1.08	1.89	0.39
$N_{projections}$	0.28	0.72	0.72	...	0.61	2.70	3.00

Provided the 3D volume is properly thresholded, the resulting sparse volume data can be converted into a table of values. The data can then be saved to columns of a row with nonzero voxel indices along the columns in the first row and volume index along the rows in the first column with an example shown in table 3.1. There is only one "temporal index" for the constraining image, which takes up only one row. Given that the positions of the nonzero voxels in the overall 3D space must also be stored with an index value (8 bytes) and representing each grayscale value as a 32-bit floating point value (4 bytes), the required number of bytes to store this information is $N_{bytes} = N_{nonzerovoxels} \times (N_{timepoints} \times 4 + 8)$. The format consists of a voxel index of type unsigned integer 64 and the voxel value field of type unsigned int 16. The range for the voxel value is based on the range [0-4095] of the detector or a 2^{12} with the next highest byte count being two (2), which gives 2^{16} possible gray levels. While 12-bit resolution is a limitation of the equipment, a 16-bit container was used. The required number of bytes to store this data to disk is $N_{bytes} = N_{nonzerovoxels} \times (N_{timepoints} \times 2 + 8)$ as the 32-bit floating point (4 bytes) is replaced with a 16-bit

unsigned integer (2 bytes). Conversion to and from the integer value to a floating point value is performed with a simple linear conversion ($vox_{integer}(i) = vox_{float}(i) \times m + b$) where m and b are chosen to maximize the range of the minimum and maximum values of the data to the min and max of an unsigned 16-bit integer [0 65535]. The slope m and offset b are calculated globally on the temporal data and another set of slope and offset values are recorded for the constrain image. It is important to calculate two sets of slope and offset values as the constrain image is in the form of nominal Hounsfield units while the projection data is normalized in the range [0-1] (see equations 2.1 and 2.3).

The constrain volume data set now consists of, at a minimum, the indices of the nonzero voxels determined by the threshold and the voxel values at the indices. The approach utilizing a smaller container (16-bit unsigned integer) for the values saved to disk thus requires less memory than that required for the reconstruction ($N_x \times N_y \times N_z \times sizeof(float)$). The process of constraining volume generation is shown in figure 3.3. The indices selected for the constrain are retained for volume reconstitution and the later 4D-DSA Sparse reconstruction stage.

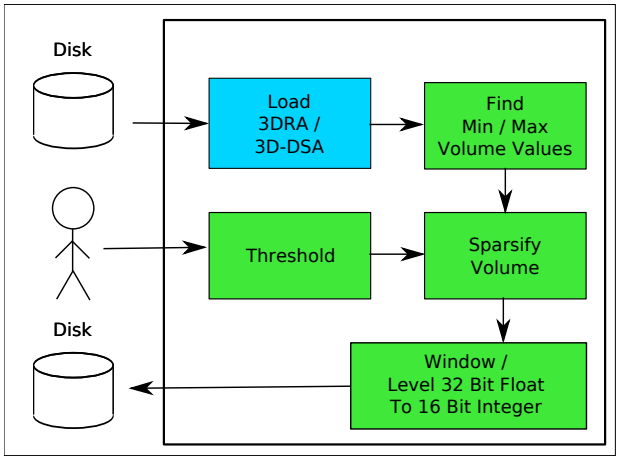

Figure 3.3: Constrain Image Generation

2.2.2 Time Curve Analysis Tool

The Time Curve Analysis Tool, as shown in figure 3.4 allowed viewing of a region of interest's Time Attenuation Curve (TAC). The tool provides a quick assessment of time curves for various ROIs. The user can select a ROI in 3D space, and once selected, the 4D-DSA TAC is compared to the projection at the corresponding projection coordinate. CPU and GPU Implementations were verified with the time curve analysis tool to ensure reconstructions represented the intensity value of the projection correctly.

2.3 Experiments

The 4D-DSA reconstruction algorithm was tested with various real-world cases, and a timing analysis was performed. A selection of cases was chosen by Dr. Charles Strother, and a subset was used from this set for the analysis, yielding 10 cases based on the availability of retrospective calibration data and the

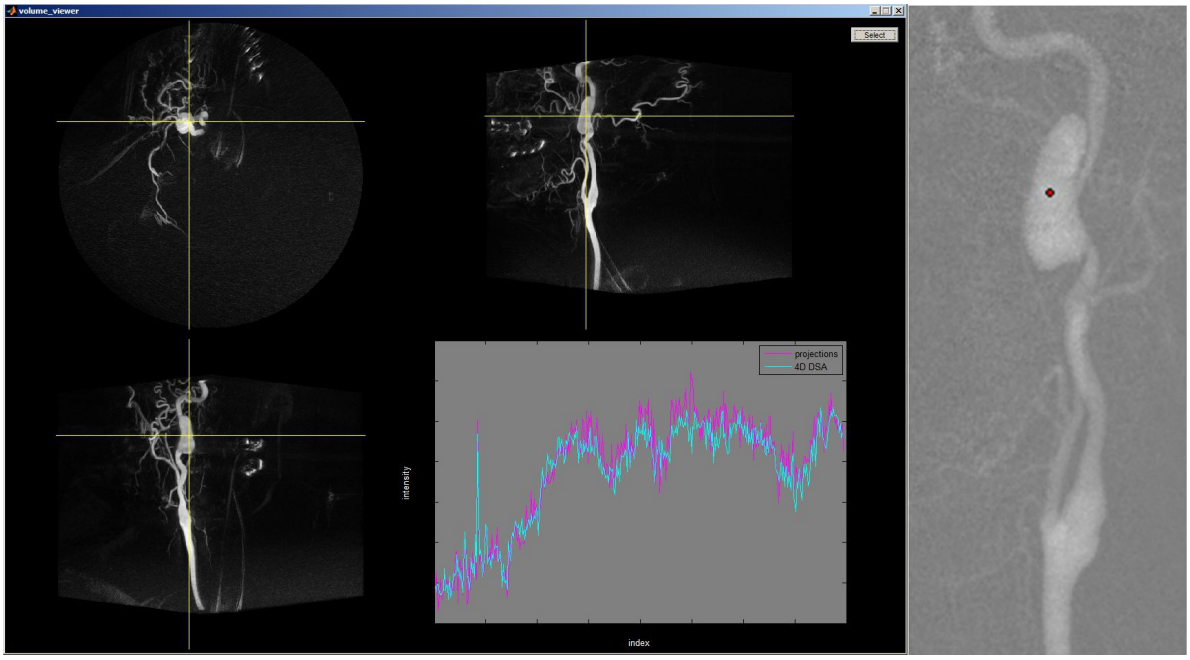

Figure 3.4: The Time Flow Curve Analysis Tool is shown left and the point in the projection is shown on the right as indicated by the red dot. The tool allows values from the 4D-DSA to be compared to the projection values. Yellow lines indicate the location of the region of interest under investigation.

ability to reconstruct the data set. These cases contained various maladies, including aneurysms and AVMs. This research was performed under an institutionally approved IRB protocol for human data. Timing and memory consumption were expected to depend on the sparsity of the image data, which in turn is related to the threshold used when forming the constraining volume. The sparsity factor is defined by the total number of volume voxels minus the number of sparse voxels divided by the total number of volume voxels multiplied by 100 ($SF = \frac{N_x \times N_y \times N_z - N_{voxsparse}}{N_x \times N_y \times N_z} \times 100$). Thresholds were selected to achieve sparsity factors of 95.000, 99.800, 99.980, and 99.995. These factors were chosen to yield nonaggressive, near typical, aggressive, and overly aggressive thresholding of the reconstructed volume. For reconstruction timing comparisons, a value of 99.800 was chosen as it yielded a near-typical value while not necessarily being optimal for any of the cases. This was chosen as it produced "typical" 3D views and reconstruction times given a fixed sparsity factor to remove the variability in reconstruction time based on the sparsity factor and, importantly, the number of reconstructed voxels. Four cases were selected to demonstrate the effects of selecting the sparsity factors. The cases are grouped by sparsity factor, with each of the four cases shown in a single panel in figure 3.5. As the sparsity increases from left to right and top to bottom, fewer voxels are included in the 4D-DSA data set. As shown in the first panel of four cases with a sparsity factor of 95.000, the threshold is low, resulting in many noise voxels being brought into the dataset. Streaking artifacts in the 4D-DSA can be seen due to these noise voxels being included. This demonstrates why 4D-DSA requires a sparse dataset. In

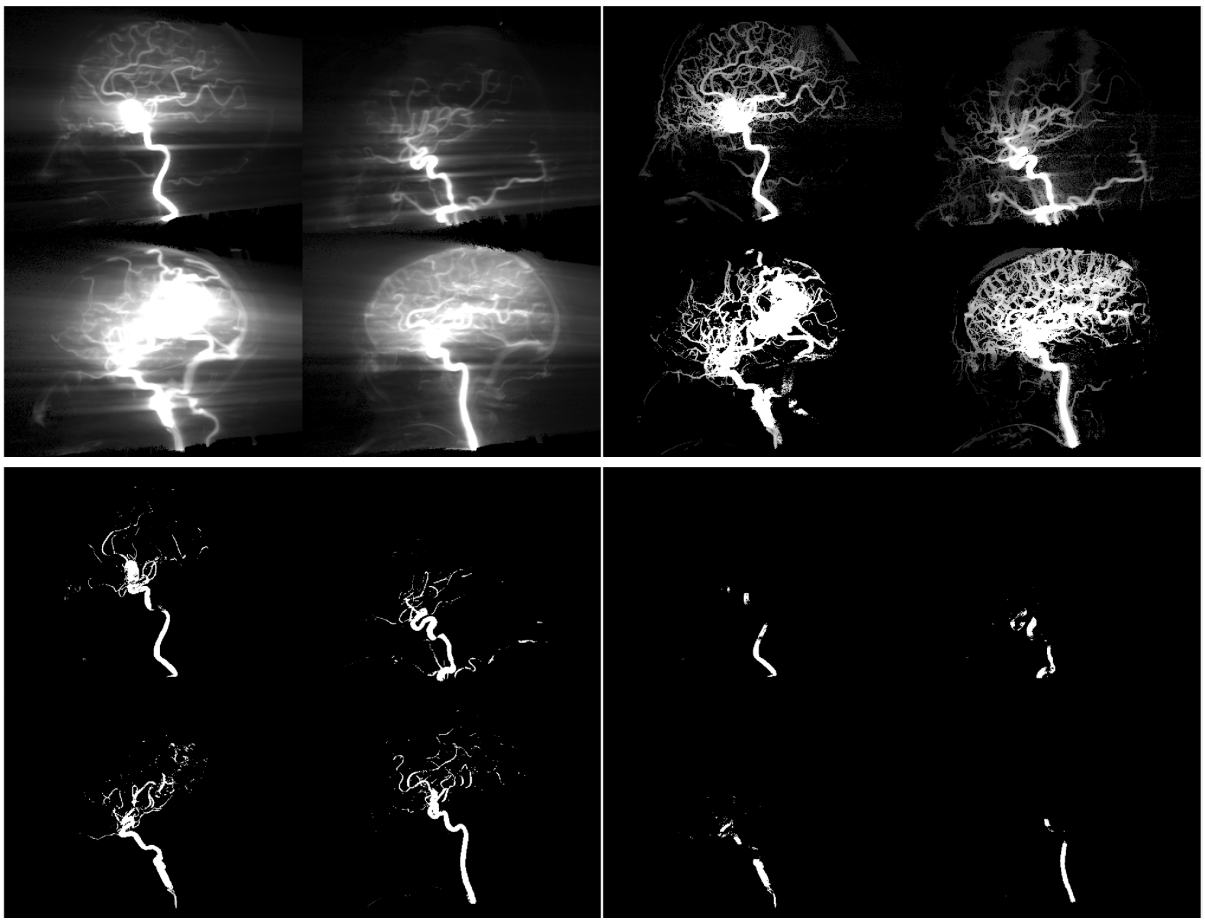

Figure 3.5: Montages for the selected four cases demonstrate the effects of the sparsity factor. Each image contains four (4) cases. The images from right to left, top to bottom, have the sparsity factor varied by 95.000, 99.800, 99.980, and 99.995, respectively, showing the effects on each of the four cases. The top left shows under thresholded, while the bottom right and bottom left show the use of an overly aggressive threshold. The top right shows the threshold of 99.800, which, while not ideal for each of the four (4) cases, can be considered close to a typical threshold.

the second panel top right in figure 3.5 a closer-to-typical sparsity factor of 99.8 was selected. The resulting threshold is not ideal for any of the individual cases. The bottom left panel sparsity factor of 99.980 shows the selected four cases with a resulting aggressive threshold demonstrating the loss of peripheral vessels. Finally, the bottom right panel demonstrates a sparsity factor of 99.995 and a resulting overly aggressive threshold where all peripheral vessels are lost, and parts of the carotid are missing from each of the cases.

3. Results

3.1 Memory vs Sparsity

A total of 10 cases labeled A through J were processed. These cases had a various number of projections of 126, 133, 172, 275, and 304. The table 3.2 is sorted by the number of projections and then by the sparsity factor. The memory reduction achieved through sparse representation can be appreciated by comparing the columns labeled Total Memory (MB) and Total Sparse Memory (MB). Reducing the total number of voxels that are processed means that later stages of applying 4D overlap algorithms also benefit from this compression. The Memory in MB is listed in column Total Memory (MB) on a full volume basis and incorporates the number of projections. The Sparse Number Of Volume Voxels indicates the number of voxels per volume based on the sparsity factor. The Total Sparse Memory in MB is the Sparse Memory Per Volume multiplied by the Number of Projections. The effective reduction in space is equal to the sparsity factor, as a sparsity factor of 95 yields a 95 percent reduction in total memory required. Reviewing the values for Total Sparse Memory in MB when the typical threshold of 98.800 from table 3.2 is selected, the min, max, and average size in MB is 49.0, 119, and 85.5, respectively. This demonstrates that to acquire 4D-DSA sparse data and save it to disk for 133 to 304 projections only requires 49 to 119 MB of memory, which is considerably less (99.8% less) than it would be to save the nonsparse data. To put this in perspective, when a typical threshold yielding a sparsity factor of 98.800 was used, the average size of the 4D-DSA data set was 85.5 megabytes (MB). To put this into perspective, this allows 11 cases to be saved to a 1 GB USB stick.

3.2 Total Recon Time

Plotting the total reconstruction time for each case shows that the cases can be grouped into two relative groups of “shorter” and “longer” reconstruction times. This separation of cases results from the change in the number of projections (and number of time points) from E of 172 to F of 275. This separation is demonstrated in figure 3.6. Results on the high end of 45 seconds, as shown in figure 3.6, would yield

Table 3.2: Case Sparsity Metrics Table

Case	Number Projections	Nx	Ny	Nz	Sparsity Factor	Sparse Number Of Volume Voxels	Sparse Memory Per Volume (kB)	Total Memory (MB)	Total Sparse Memory (MB)
A	133	512	512	390	95.000	5111812	9984	25935	1297
A	133	512	512	390	99.800	204474	399	25935	52
A	133	512	512	390	99.980	20449	40	25935	5
A	133	512	512	390	99.995	5113	10	25935	1
B	133	512	512	390	95.000	5111811	9984	25935	1297
B	133	512	512	390	99.800	204475	399	25935	52
B	133	512	512	390	99.980	20449	40	25935	5
B	133	512	512	390	99.995	5113	10	25935	1
C	133	512	512	390	95.000	5111809	9984	25935	1297
C	133	512	512	390	99.800	204474	399	25935	52
C	133	512	512	390	99.980	20449	40	25935	5
C	133	512	512	390	99.995	5113	10	25935	1
D	126	512	512	390	95.000	5111810	9984	24570	1229
D	126	512	512	390	99.800	204474	399	24570	49
D	126	512	512	390	99.980	20450	40	24570	5
D	126	512	512	390	99.995	5113	10	24570	1
E	172	512	512	390	95.000	5111810	9984	33540	1677
E	172	512	512	390	99.800	204475	399	33540	67
E	172	512	512	390	99.980	20450	40	33540	7
E	172	512	512	390	99.995	5114	10	33540	2
F	275	512	512	390	95.000	5111811	9984	53625	2681
F	275	512	512	390	99.800	204474	399	53625	107
F	275	512	512	390	99.980	20450	40	53625	11
F	275	512	512	390	99.995	5115	10	53625	3
G	304	512	512	390	95.000	5111810	9984	59280	2964
G	304	512	512	390	99.800	204475	399	59280	119
G	304	512	512	390	99.980	20449	40	59280	12
G	304	512	512	390	99.995	5114	10	59280	3
H	304	512	512	390	95.000	5111812	9984	59280	2964
H	304	512	512	390	99.800	204474	399	59280	119
H	304	512	512	390	99.980	20449	40	59280	12
H	304	512	512	390	99.995	5115	10	59280	3
I	304	512	512	390	95.000	5111812	9984	59280	2964
I	304	512	512	390	99.800	204474	399	59280	119
I	304	512	512	390	99.980	20449	40	59280	12
I	304	512	512	390	99.995	5113	10	59280	3
J	304	512	512	390	95.000	5111810	9984	59280	2964
J	304	512	512	390	99.800	204475	399	59280	119
J	304	512	512	390	99.980	20450	40	59280	12
J	304	512	512	390	99.995	5113	10	59280	3

a clinically acceptable time of less than a minute to perform a 4D-DSA recon. In the event that fewer projections are needed, it takes 17.5 seconds to perform both a 3D reconstruction and a 4D recon. If the 4D needs to be done repeatedly, and the initial 3D recon can be reused, approximately 5.5 seconds can be saved from total time utilizing a state-of-the-art 3D reconstruction stage. It should be noted that 4D-DSA does not require the time per 3D reconstruction multiplied by the number of projections. This demonstrates the major strength of using sparse reconstruction, as once the 3D constraining volume is generated, it is only necessary to update a small number of voxels for each time frame. Figure 3.6 also demonstrates that total time increases with the number of projections.

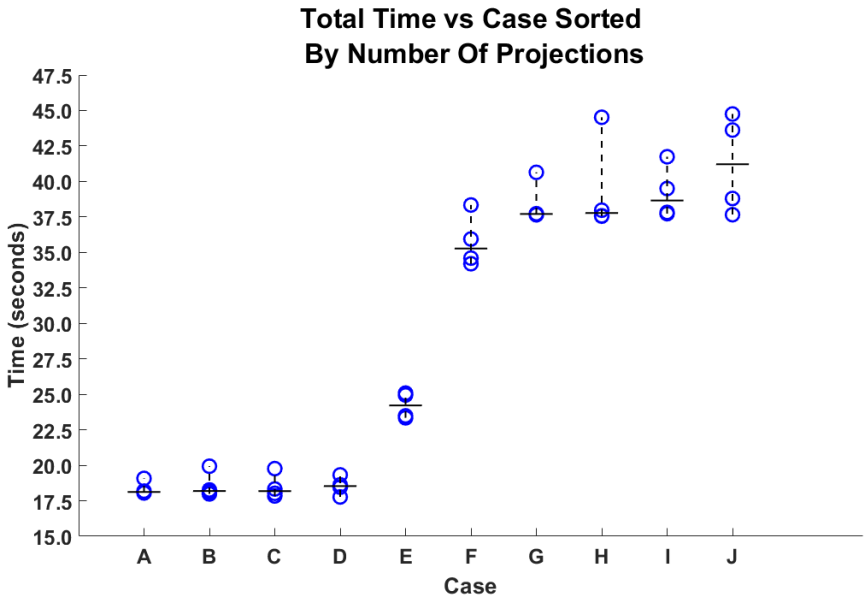

Figure 3.6: Total reconstruction time excluding preprocessing time in seconds varied by sparsity factor with increasing number of projections from left to right.

The median time was plotted with a best-fit line for the 4D reconstructions and, as expected, was linear with a Pearson's R-value of 0.99 (0.9944). Therefore, the total time scales linear with the number of projections (and time points) in the scan as shown by figure 3.7.

A graph of the total time per reconstruction stage as varied by sparsity factor and number of projections for all cases is shown in figure 3.8. The graph indicates the tasks that take the longest duration are the backprojection and forward projection. The FFT filtering and backprojection stages make up the 3D reconstruction stage, while the forward projection and the remaining stages make up the 4D-DSA portion of the recon. It should be noted that the Sparse Backprojection, Sparse Temporal Data Generation, Generate Sparse Constrain Volume, and Overlap Correction take up relatively little time. Importantly the Sparse Backprojection reconstruction time is in the sub-second (0.79 seconds) range and represents the sparse backprojection of all

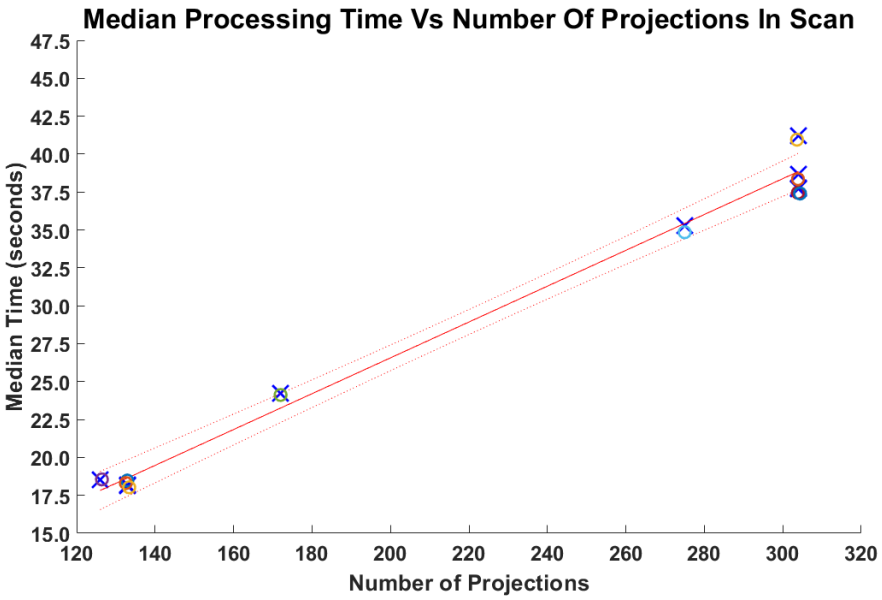

Figure 3.7: The total number of projections for a given case vs the median total reconstruction time for each case varied by the sparsity factors. Pearson's R-value is 0.99, indicating a linear fit and that the total 4D-DSA reconstruction times scale linearly with the number of projections. A small jitter value was applied to the data shown as circles to separate graphically overlapping values.

the projections.

The total reconstruction times were generated for the sparsity factor of 98.800. This was done to provide a sense of the typical total duration that would be incurred for a 4D-DSA reconstruction. This graph indicates that the two longest duration tasks are the forward projection and backprojection tasks. The FFT Filtering can be grouped with the backprojection task to be categorized into the 3D reconstruction stage. The forward projection and remaining tasks, excluding FFT filtering and backprojection, are then grouped into the 4D-DSA reconstruction stage.

The individual stages were timed and then grouped into the 3D-DSA portion (3D recon), and then the remaining 4D-DSA stages were grouped into the 4D-DSA portion of the reconstruction process with the results shown in figure 3.10. What should be noted by the results of this graph is that the total time of the 4D-DSA stages is only slightly more than the 3D portion and not the number of projections times longer. This demonstrates the impact of performing a spare reconstruction using the sparse backprojector and the efficient method in which the output data is stored and further processed. The 3D reconstruction median value was 11.97 seconds, while the 4D portion of the reconstruction time was 15.17 seconds. This results in an approximate total time, the sum of these two values, to generate a 4D-DSA of 27.14 seconds. This total time does not include manual interaction time to obtain a threshold.

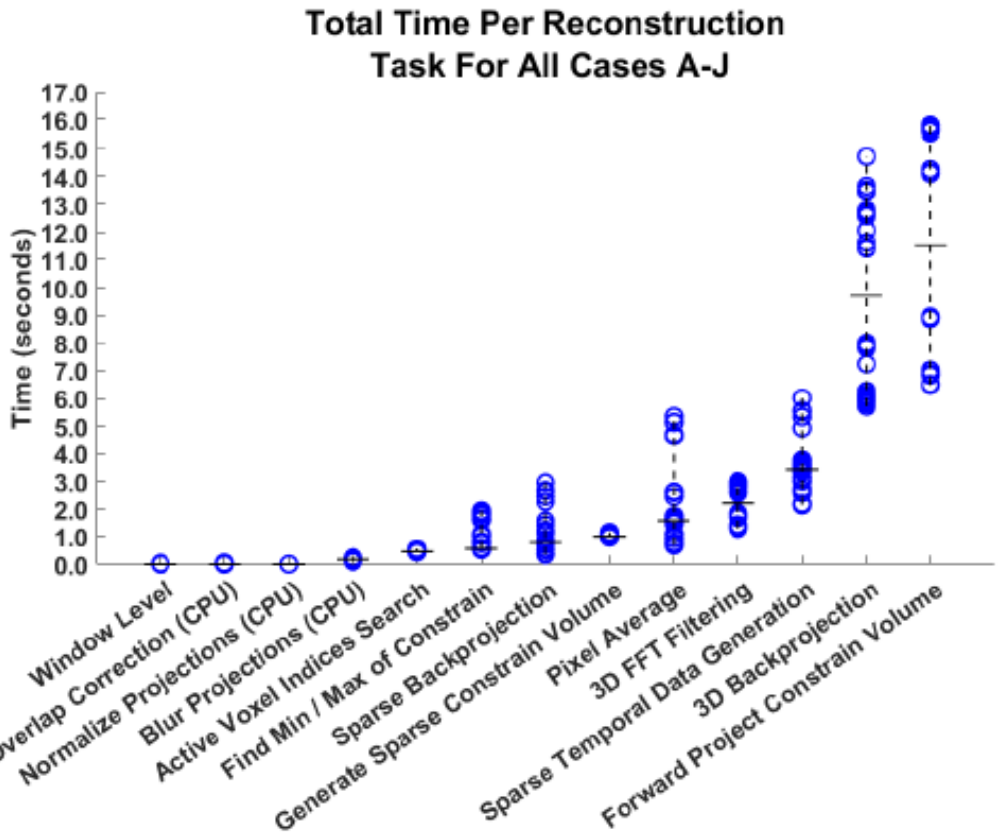

Figure 3.8: Total reconstruction time for each reconstruction stage for all cases varied by the sparsity factor and number of projections. The solid line indicates the median value over the range of values indicated by the dashed line. The blue data points indicate the total time for a specific case having a specific number of projections and a specific sparsity factor. CPU is used to indicate stages for which calculations are performed on the CPU and not the GPU.

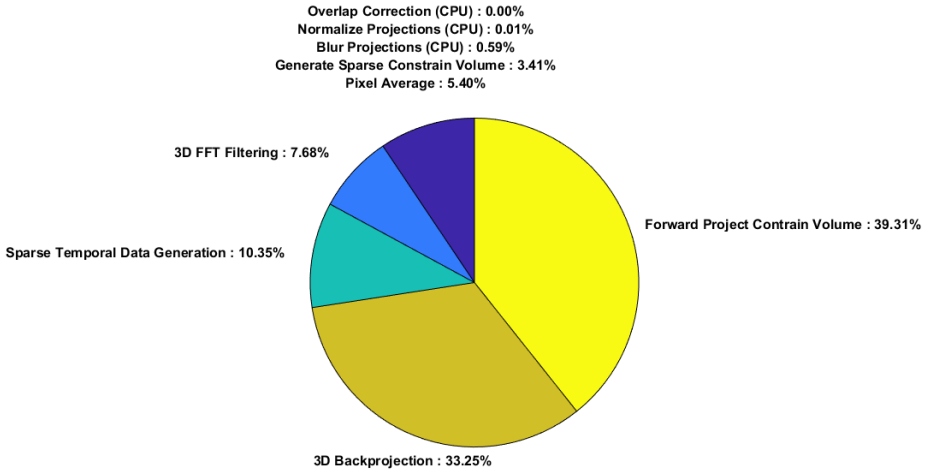

Figure 3.9: Median time total reconstruction time for each reconstruction stage expressed as a percentage of the total. Percentages represent the percent of total median times across all cases when the threshold is set to generate a sparsity factor of 99.80% .

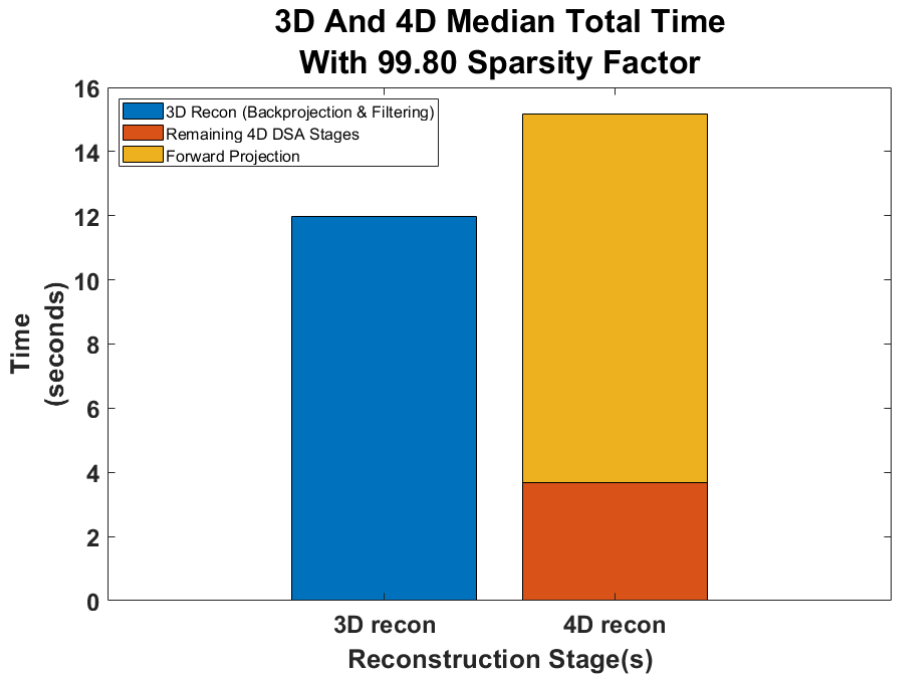

Figure 3.10: Total time bar char with 3D DSA reconstruction stages of projection filtering and backprojection grouped and compared to the 4D stages aggregated using a sparsity factor of 99.980.

3.3 Per-Projection Recon Time

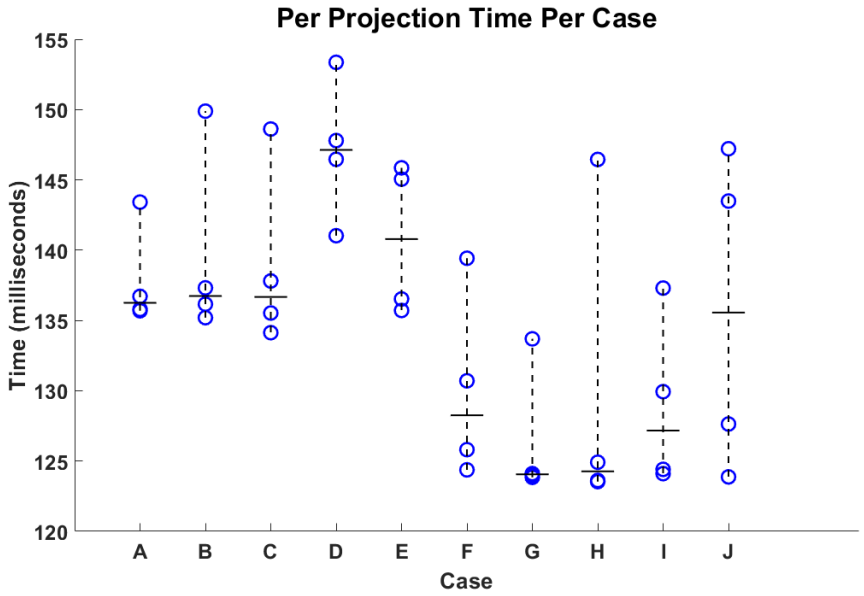

Figure 3.11: Per-projection reconstruction time in milliseconds excluding preprocessing varied by sparsity factor. The solid line indicates the median value over the range of values indicated by the dashed line. The blue data points indicate the total time for a specific case having a specific number of projections and a specific sparsity factor.

While providing a sense of how much time could be incurred when performing a 4D-DSA from start to finish the total reconstruction time analysis suffers from variability in the number of projections between cases. Therefore a per-projection analysis is discussed here. The per-projection times for all cases and sparsity factors are shown in figure 3.12. This graph indicates much less variability among the data points for the various stages when compared to the similar graph of total times in figure 3.8 where the number of projections plays a significant role in the variability among data points. When looking at figure 3.8 and figure 3.11 it should be clear that the duration of the scan increases linearly with the number of projections.

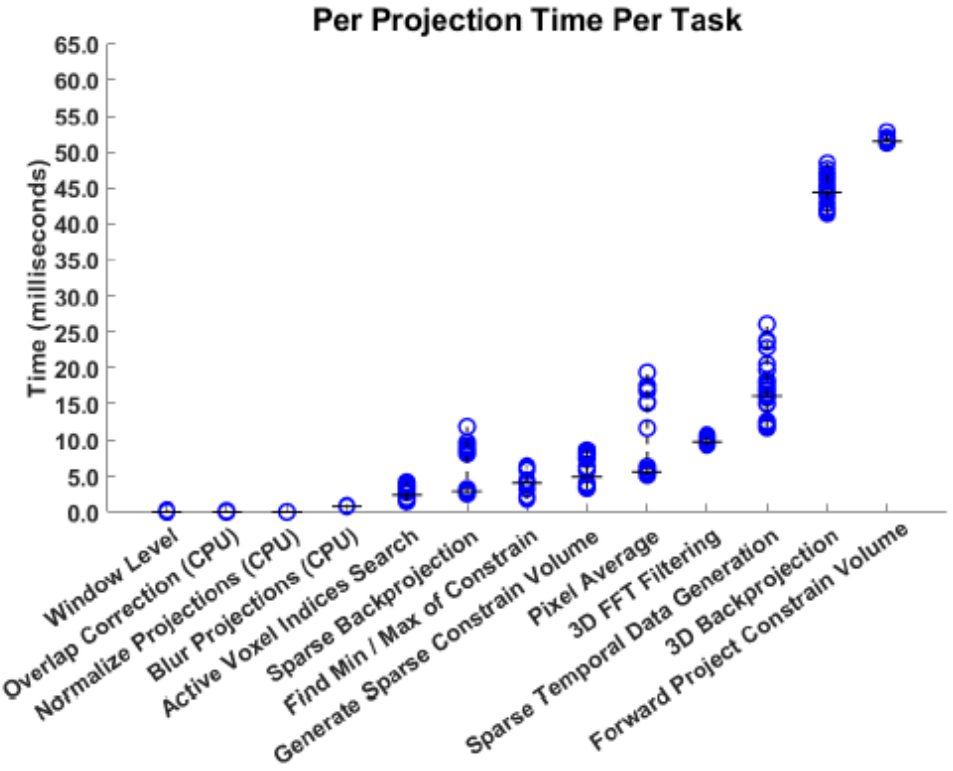

Figure 3.12: Per-projection reconstruction time in milliseconds for each reconstruction stage for all cases varied by the sparsity factor and number of projections. The solid line indicates the median value over the range of values indicated by the dashed line. The blue data points indicate the total time for a specific case having a specific number of projections and a specific sparsity factor. CPU is used to indicate stages for which calculations are performed on the CPU and not the GPU.

The per-projection percent of time for each reconstruction stage is shown in figure 3.13 and compares similarly to the total percent of time for each reconstruction stage graph in figure 3.9. These two graphs indicate as expected the percent time per stage is similar regardless of the number of projections.

The per-projection times were selected for a typical sparsity factor of 99.80 and grouped into three categories of 3D recon, forward projection, and remaining 4D-DSA stages as shown in figure 3.14. This demonstrates again that the 4D takes only marginally longer than the 3D reconstruction with the majority of time spent

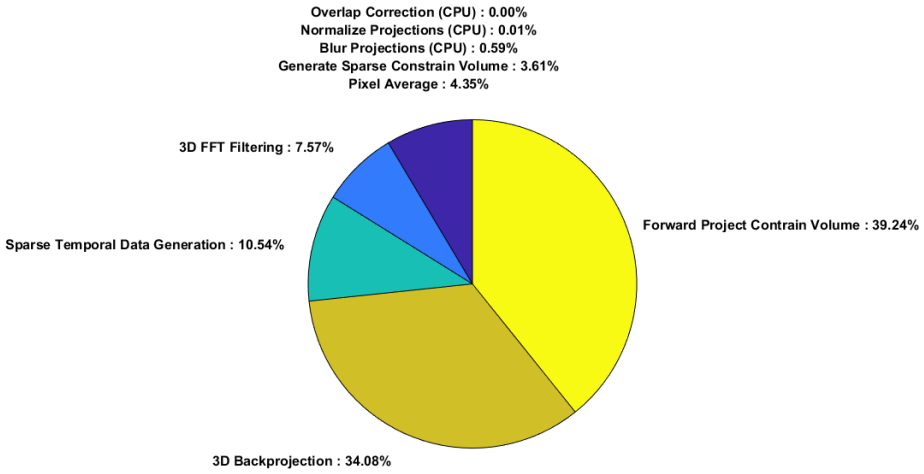

Figure 3.13: Medan time per reconstruction stage expressed as a percentage of the total. Median times are across all cases with threshold set to generate a sparsity factor of 99.80%.

in forward projecting the constrain image.

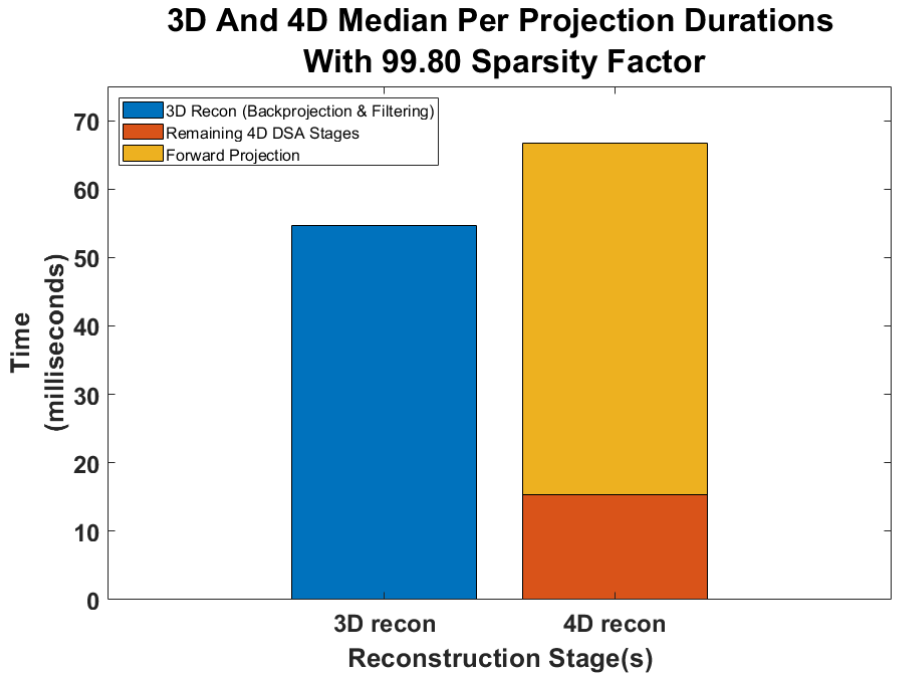

Figure 3.14: Per-projection duration in milliseconds grouped into categories of 3D Recon, Forward projection, and remaining 4D-DSA Stages. Median times are across all cases with threshold set to generate a sparsity factor of 99.80%.

4. Discussion

The 4D-DSA reconstruction times were investigated for various cases. For each case, an optimal threshold was visually determined. Data sets varied based on the number of projections used in the acquisition, the type of malady, and the number of voxels needed to represent the vasculature. The cases were thresholded using a sparsification factor representing the number of voxels reconstructed. The sparsification factor then sets the threshold. The sparsification factor and resulting threshold specified is not to be considered an optimal setting given the case as the threshold setting is case and user-dependent. The sparsity metric is used here to demonstrate three cases of under threshold, near optimal, and over thresholded to demonstrate reconstruction times for various cases under a range of feasible values for the user specified threshold value.

5. Summary

The purpose of this chapter was to convey to the reader the design of the 4D-DSA software and to demonstrate the design is feasible, realizable, and efficient. The 4D-DSA software was designed, coded, and tested. A sparse backprojector and forward projector were implemented The forward projector was modified to support vessel counting to operate as a vessel overlap detector. To this author's knowledge, this is the first time a sparse backprojector has been implemented, tested, and demonstrated with performance metrics provided. It has been shown that the 4D-DSA process can be greatly simplified with data resulting in a sparse table by applying some minor modifications to a GPU backprojection algorithm resulting in a sparse backprojector. By retaining the 4D-DSA temporal data in its original raw form the table can then be used to perform various 4D-DSA algorithms on the temporal data. This sparse backprojector processes data only at indices at active voxel locations thus saving both time and space (data storage).

A key finding of this work is that by implementing a Sparse Backprojection stage the reconstruction time for this stage was brought down to sub-second (0.79 seconds) for all temporal volumes which would have been on the order of 5 seconds for each temporal volume. The additional benefit to the sparse backprojection stage is the savings in memory both in RAM and persistent memory (mass storage/hard disk) required to store the data. As shown in table 3.2 sparsifying the volume and retaining and reconstructing only the data with active voxels can greatly reduce the required memory and computational resources.

Various cases of differing complexity and malady were investigated for reconstruction times to demonstrate what is a negligible addition to the current 3D-DSA reported state-of-the-art[61] reconstruction time of five (5) seconds. The 3D reconstruction median value was 11.97 seconds while the 4D-DSA reconstruction time

was 15.17 seconds. This results in an approximate total time, the sum of these two values, to generate a 4D-DSA of 27.14 seconds. This results in an approximate total time to 4D-DSA of 27.14 seconds not including any manual interaction time to obtain a threshold. With the typical threshold of 98.800, the min, max, and average size in MB required to store the data is 49, 119, and 85.5 respectively. This research demonstrates 1) 4D-DSA reconstruction can be performed in under 30 seconds for a wide range of scenarios and is suitable for intra-procedural tasks and 2) the implementation manages memory and disk space in a way that is efficient and compatible with commercial hardware.

4 Volumetric Limiting Spatial Resolution Analysis of Four Dimensional Digital Subtraction Angiography (4D-DSA) [1]

1. Introduction

The prior chapter focused on the design and implementation of 4D-DSA. In this chapter, the performance of 4D DSA is discussed. Specifically the volumetric limiting spatial resolution (VLSR) of 4D-DSA is quantified and compared to 3D-DSA, with the ultimate goal being to determine how close and under what reconstruction settings a 4D-DSA can maintain the resolution of standard 3D-DSA reconstructions. Measurements of resolution are presented for both the physical phantom (PPH) and the in silico phantoms (ISPH). It is shown that 4D-DSA maintains the resolution of the constraining 3D image and is capable of maintaining the resolution of the 3D-DSA provided acceptable ranges of 4D DSA reconstruction parameters are used. The most important parameters are i) the size of the blurring kernel applied to the 2D projection images, and ii) the threshold applied to the 3D-DSA reconstruction to form the constraining volume. This chapter begins with a discussion of the methods used for determining the Volumetric Limiting Spatial Resolution (VLSR).

2. Methods

2.1 Limiting Resolution

In the previous chapter it was shown that the 4D image volume at time t can be written as

[1] The revised and adapted contents of this chapter have been previously published in the following journal article: Davis, Brian J. and Oberstar, Erick and Royalty, Kevin and Schafer, Sebastian and Mistretta, Charles, "Volumetric limiting spatial resolution analysis of four-dimensional digital subtraction angiography", Journal of Medical Imaging 3, 1 (2016), pp. 013503--013503.[1]

$$I(x, y, z, t) = C(x, y, z)W(x, y, z, t) \tag{4.1}$$

where C is the 3D constraining volume generated by thresholding the 3D DSA reconstruction, and W is a 3D weighting volume for time t, generated by backprojecting a blurred and normalized version of the 2D projection from time t. For convenience, the x, y, and z dependence will be omitted and any dependence on adjustable reconstruction parameters will be shown explicitly. Therefore, the 4D DSA image volume for time t is:

$$I(t) = C(v_{th})W(t; k_B) \tag{4.2}$$

where v_{th} is the threshold applied to the 3D DSA and kB is the blurring kernel size applied to the 2D projection data. The 4D-DSA process includes several nonlinear operations such as thresholding and division of the blurred temporal projections by blurred reprojections of the constraining volume. Although 4D-DSA is nonlinear, it is treated as linear at an operating point. In this approximation, a transfer function analysis in frequency space can be applied to estimate the limiting spatial resolution. The limiting spatial resolution is defined as the frequency where the transfer function reaches the first zero crossing ('first zero') when using a purely mathematical approach or in the analysis of real-world data the first frequency on the MTF curve reaches 10%. Examining equation 4.2 reveals two important operations in 4D-DSA that can be described as 'spatial truncations'. First, there is the intensity thresholding applied to the 3D-DSA to obtain the constraining volume C. Although this is technically a truncation in the intensity domain, for realistic vessels where the 3D-DSA images have slightly smoothed vessel edges, the thresholding operation has the effect of creating a slight spatial truncation of the vessel edges. Second, there is the multiplication of the constraining volume by the weighting volume. Here, since kB is chosen to create some amount of blurring in projection space before backprojection and formation of the weighting volume W, we expect the vessel information in W to be wider than the actual vessel. Therefore, the multiplication of C and W is expected to spatially truncate W to the size of C.

To understand the effect of spatial truncation on the limiting spatial resolution, we first consider the simple case of multiplying two 1D rect functions of different widths. If the original rect functions have widths a (mm) and b (mm), the Fourier transforms will be sinc functions with first zeros at $f = 1/a$ cycle/mm and $f = 1/b$ cycle/mm. The multiplication of these two rect functions yields a new rect function with the width equal to min(a,b). Consequently, the Fourier transform is a new sinc with its first zero at $f = 1/min(a, b)$ cycle/mm. Or, equivalently, the first zero is at $max(1/a, 1/b)$. More generally, if some function g_A with its

first zero at frequency f_A is spatially truncated via multiplication by a rect function of width b, which has its first zero at $f_B = 1/b$, then the result will have its first zero located at

$$f_{trunc} = max\left(f_A, f_B\right) \tag{4.3}$$

Notice this contrasts with the case of convolution in the image domain. By the convolution theorem, the convolution of two functions g_A and g_B in the image domain is equivalent to the multiplication of their Fourier transforms in the frequency domain. If the two functions have their first zeros at f_A and f_B, then their convolution will have its first zero at the lesser frequency:

$$f_{conv} = min(f_A, f_B)$$

These results can be applied to estimate the limiting resolution of 4D DSA. If the constraining volume has its first zero at spatial frequency f_C and the weighting volume has its first zero at f_W, then the product of these volumes is expected to have its zero at:

$$f_I = max(f_C, f_W)$$

The first zero of the weighting volume is, in turn, related to the first zero of the temporal projection and the blurring kernel applied to that projection. At the detector plane, there is a convolution

$$p_{blur} = p_t * k_B$$

which has its first zero at

$$f = min(f_{p_t}, f_{k_B})$$

However, the subsequent backprojection operation has the effect of demagnifying ('shrinking') the image and increasing the spatial frequencies present in the image. For example, if the geometric magnification of a vessel or object is m = 2, then 2 cycle/mm at the detector plane corresponds to $m \times 2$ cycle/mm = 4 cycle/mm at the object plane. Accounting for this effect, the first zero of the blurred projection at the plane of the object is

$$f_{pblur} = m \times min(f_{pt}, f_{k_B})$$

Putting the results together, the limiting resolution of the 4D DSA image is expected to be

$$f_I = max(f_C, f_W) = max(f_C, m \times min(f_{pt}, f_{k_B})) \tag{4.4}$$

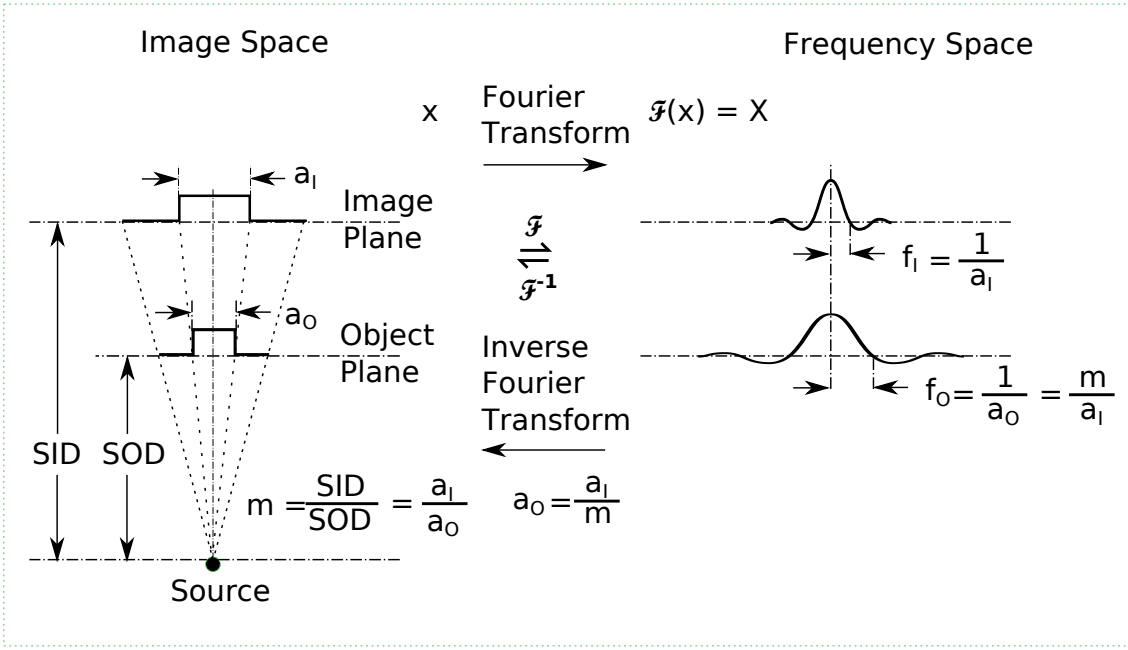

Figure 4.1: Resulting geometric and frequency scaling from the image plane to the object plane.

That is, the resulting limiting resolution of 4D-DSA, f_I, is the maximum of the limiting resolution of the constraining image, C, and the minimum of the limiting resolution of the blurring kernel, k_B, and the temporal projection data, p_t, scaled by the geometric magnification, m.

2.2 Experiments

The standard approach[62] of scanning a fine highly attenuating wire centered in and perpendicular to the transverse plane was performed. The effects of the 4D-DSA reconstruction on volumetric spatial resolution were investigated using both an in silico phantom and the scan of a physical 76 micron (um) diameter tungsten wire centered in a cylindrical supporting structure. The in silico phantom was modeled after the physical phantom as a cylinder centered in the transverse plane with the axis parallel to the axis of rotation extending throughout the entire volume of interest. The physical phantom is shown in figure 4.2. The

constraining image inherits the reconstruction parameters from the 3D-DSA as it is a 3D-DSA where a threshold has been applied. The spatial resolution of a 4D temporal volume can be obtained by the same means as for the 3D-DSA. The 3D-DSA is compared with the 4D temporal frames (temporally enhanced 3D volumes) of 4D-DSA reconstructions. This was done on a volumetric basis using a single transverse slice of a physical or digital phantom of a small wire. Resulting point spread function (PSF) data were radially averaged and Fourier analysis was performed to generate averaged MTF data for each 3D-DSA volume and 4D-DSA temporal slice. The limiting spatial resolution was automatically determined by finding the spatial resolution when 10% of the magnitude at zero spatial frequency was reached. Numerical simulations and reconstruction of the real-world phantom were performed using a combination of MATLAB (The Mathworks Inc. Natick, MA, USA) and CUDA (NVIDIA Corp. Santa Clara, CA, USA) based software. The spatial resolution at the center of the central slice of the x-ray angiography system (Artis zee, Siemens Healthcare, Forchheim, Germany) used is determined by equation 4.5. The spatial resolution is based on the Nyquist sampling criteria using the detector spacing (du), imaging geometry source-to-image distance (SID) and source-to-object distance (SOD), to determine the minimal detectable distance (object size) achievable in the transverse plane. This equation does not account for blurring effects due to focal spot, geometric instabilities of the C-Arm, or projection filtering. The minimal resolvable distance (object size) calculation is shown in equation 4.6.

$$\begin{aligned} f_{Nyquist} &= \frac{1}{2\times du\times\frac{1}{m}} = \frac{m}{2\times du} = \frac{SID}{2\times du\times SOD} \\ &= \frac{1200[mm]}{2[\frac{del}{cyc}/]\times 0.3080[\frac{mm}{del}]\times 750[mm]} = 2.59[\frac{cyc}{mm}] \approx 2.60[\frac{lp}{mm}] \end{aligned} \tag{4.5}$$

The scan geometry was determined using a standard 4D-DSA acquisition procedure without zoom of the detector/C-Arm with SID set to the maximum of 1200 mm and SOD held constant at 750 mm resulting in the magnification factor, m, and collimation set to the maximum field of view with 2x2 binning yielding a detector resolution of 1240x960 detector elements with an isotropic detector element size of 0.3080 mm (2480x1920 native non-binned resolution with 0.154 mm isotropic detector elements). The minimal resolvable distance is calculated with equation 4.6 which was used to ensure the reconstruction grid was smaller than this dimension.

$$d_{min} = \frac{du}{m} = \frac{1}{f_{Nyquist}} = 0.385[mm] \tag{4.6}$$

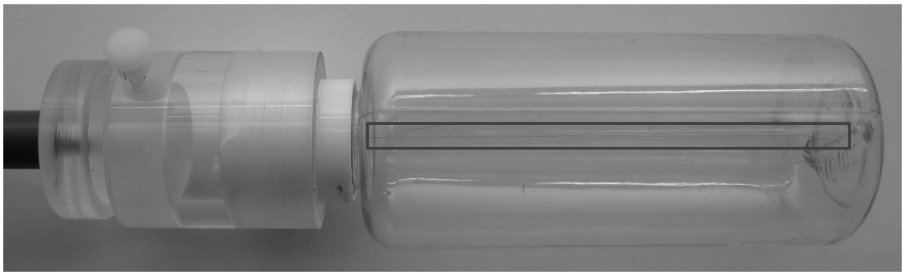

Figure 4.2: Image of the physical phantom. The location of the tungsten wire has been highlighted by a dark gray box overlaid on the image and is located in the center of the box.

The selection of the maximum allowable wire size was found to be 86 micron using the approach of Nickoloff[63]. The reconstruction grid (slice) was 512 by 512 voxels with a 0.0376 mm isotropic voxel size. The voxel size was made considerably smaller than the minimum resolvable object size, d_{min}, to ensure proper reconstruction and 4D-DSA reconstruction artifacts could be properly investigated. Off-axis and off-central slice resolution was not investigated in this research and is a topic for future investigation and research. The physical wire phantom was built using a Scientific Instruments (NJ, USA) 0.076 mm Tungsten wire part number W91 surrounded in an air-filled thin walled plastic cylinder, 47 mm O.D., as a supporting structure as shown in figure 3. The phantom was then scanned on x-ray angiography system. The scan was 8.2 seconds in duration providing 248 projections, at a frame rate of 30 fps, at 60.4 kVp, and 168 mAs.

The phantom was placed in the field of view for the mask run and removed from the field of view for the fill run. This was done to allow the same processing pipeline to be used for current 4D-DSA processing while also setting the Automatic Exposure Control to the object during the mask run. The mask and fill projections were then interchanged to allow correct subtraction and sign of the value in the projections. Normalized projections using equation 2.3 were used in this analysis.

The steps to generate MTFs are as follows: Select a backprojection filtering kernel and perform a reconstruction at the correct zoom factor to satisfy the Nyquist criteria and reconstruction grid requirements. Acquire a central transverse slice of the temporal frame of the reconstructed object and repeat the process for each 4D volume. Sum all transverse slice time frames extracted from each 4D time frame volume to make a composite PSF. Find the center of the composite point spread function (PSF). Preprocess the transverse slices of the temporal time frame if necessary. Radial average the temporal slice in the spatial domain using the center coordinates found using the composite time frame. Generate the measured Modulation Transfer Function (MTF) from the radial averaged PSF by taking the Fast Fourier Transform (FFT). Then take the absolute value of the result of the FFT. The system MTF is then determined by dividing the measured MTF by an estimate of the MTF of the object (Jinc). The maximum spatial resolution is determined from the resulting MTF plot by finding the first zero or value on the frequency axis where a ten percent of the zero

frequency value is reached.

Generation of a composite frame stated above was performed to aid in finding an accurate center of the point spread function. Composite frame generation was performed to avoid projection angle-dependent modulation in some reconstructed frames. The modulation was induced by the backprojection of blurred temporal projection data where blurring as a result of the blurring kernel, of size zero or two, is less than that induced blurring due to geometric instability. Preprocessing of the transverse slice as stated above can include cropping the image from 512 to 64 voxels on center to avoid any ripples in the frequency response curve near zero spatial frequency due to the standard deviation increasing with increasing N as described in Bischoff[64].

3. Results

The limiting spatial resolution of the 3D-DSA was found to be higher for the in silico phantom than for the physical phantom and is a result of the simulated processing stage not accounting for geometric instability and focal spot blurring. While the results of the in silico phantom and physical phantom are not similar the discussion of the differences is an important topic. The results are summarized in table 4.1. Frequency response plots for the 3D C-Arm CT, constraining image, physical phantom, and in silico phantom are shown in figures 4.3, 4.4, and 4.5.

The spatial resolution of the 4D-DSA tracks with that of the constraining image as can be seen from the table when appropriate kernel sizes, 5, 10, and 20, are used. Provided the threshold of the constraining image is not severe and the limiting resolution of the constraining image is maintained close to the 3D-DSA then the limiting resolution of 4D-DSA temporal volumes are very near to the resolution of the 3D-DSA reconstruction volume. While equation 4.4 may appear to inflate the resolution of 4D-DSA it does so only marginally. Blurring kernels of the size typically used widen the object data in image space and thus decrease the limiting spatial frequency of the object in frequency space. The wider the image is in image space the smaller the value is for the zero crossing in frequency space for the frequency response of the image and thus the smaller the contribution is to the resulting limiting spatial resolution. When typical parameters for the projection blurring are used, the effects of the weighting volume term (i_W) in equation 4.4 has little impact on the limiting spatial resolution.

When the 4D-DSA algorithm is applied with square kernels of 5, 10, and 20 pixels, the resolution is lowered for the in silico phantom and physical phantom only as a result of the constraining image. The kernel size can only act to increase the resolution beyond the constraining image by allowing high spatial frequency

Table 4.1: In silico and physical phantom limiting spatial resolution summary table.

			Limiting Spatial Resolution (lp/mm)			Relative Percent Error 100*(A-B)/A		
	Kernel Size	Threshold	3D-DSA	Constraining Image	4D-DSA	Constraining Image vs. 3D-DSA	4D-DSA vs. Constraining Image	4D-DSA vs. 3D-DSA
In silico phantom	20	10	2.28	2.21	2.21	3.07	0.00	3.07
	10	10	2.28	2.21	2.21	3.07	0.00	3.07
	5	10	2.28	2.21	2.20	3.07	0.45	3.51
	2	10	2.28	2.21	2.92	3.07	-32.13	-28.07
	20	30	2.28	2.55	2.55	-11.84	0.00	-11.84
	10	30	2.28	2.55	2.55	-11.84	0.00	-11.84
	0	10	2.28	2.21	4.33	3.07	-95.93	-89.91
Physical phantom	20	10	1.69	1.66	1.67	1.78	-0.60	1.18
	10	10	1.69	1.66	1.67	1.78	-0.60	1.18
	5	10	1.69	1.66	1.67	1.78	-0.60	1.18
	2	10	1.69	1.66	1.67	1.78	-0.60	1.18
	20	30	1.69	1.82	1.82	-7.69	0.00	-7.69
	10	30	1.69	1.82	1.82	-7.69	0.00	-7.69
	0	10	1.69	1.66	1.67	1.78	-0.60	1.18

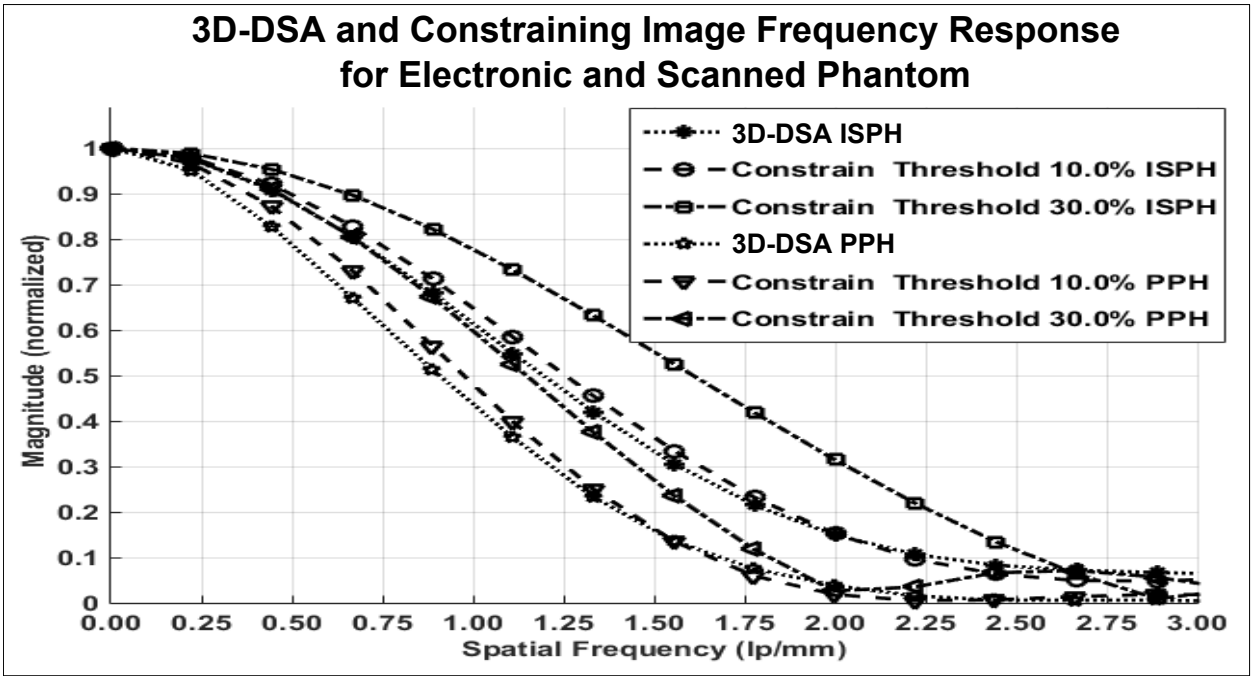

Figure 4.3: 3D-DSA and Constraining Image Frequency Response Curves for the electronic (ISPH) and physical phantoms (PPH).

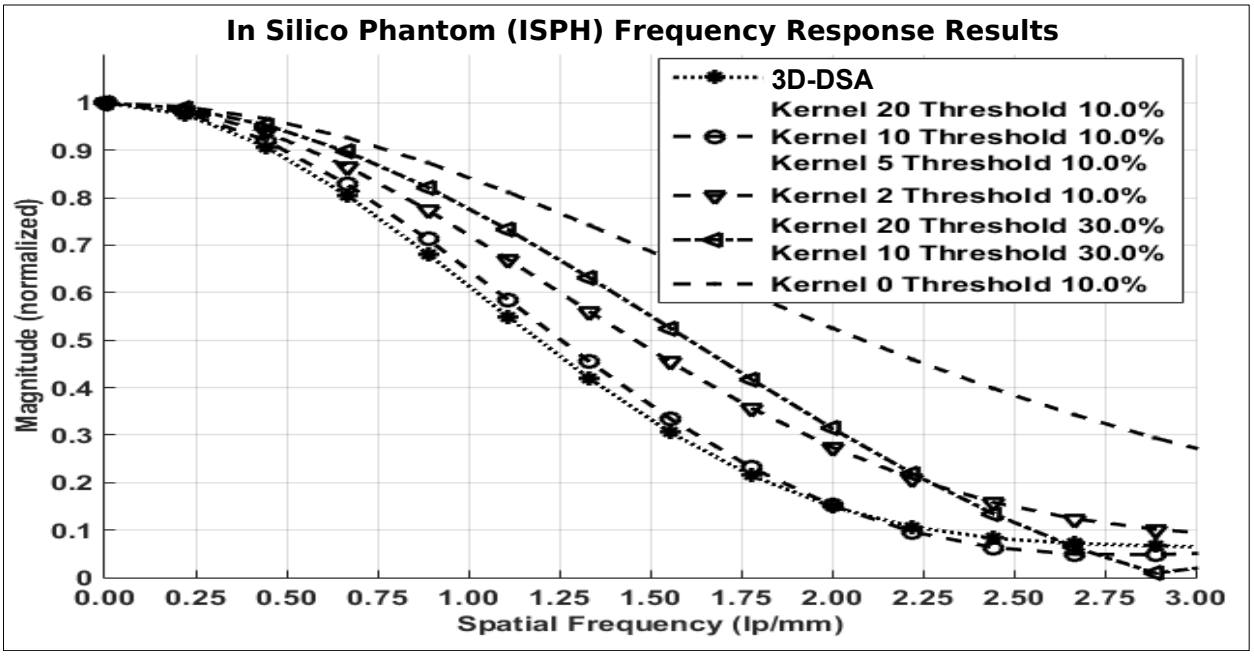

Figure 4.4: Electronic phantom (ISPH) frequency response results. Near exact results have been grouped for clarity.

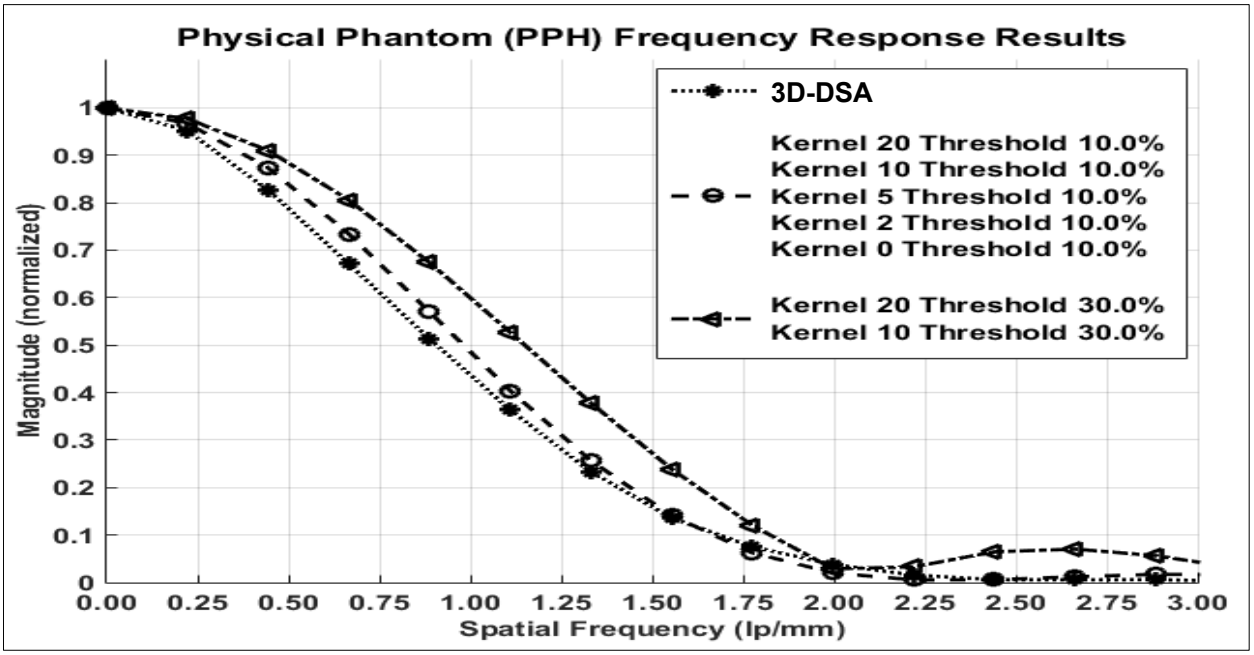

Figure 4.5: Physical Phantom (PPH) frequency response results. Near exact results have been grouped for clarity.

data in the projection to modulate the constrain image. This represents a reduction of ∼3.1% for the in silico phantom and ∼1.2% for the physical phantom. These typical values for the kernel size have a minor effect on the spatial resolution. It is not until the kernel is changed to 2 or no kernel is applied that projection is allowed to retain the high spatial frequency content. The effect is a modulation of the 4D-DSA volumes during the backprojection operation. The result is a narrowing of the 2D PSF of the constraining 3D volume perpendicular to the ray along which the data is backprojected. The figures 4.6 and 4.9 clearly show when modulation does and does not occur along the projection. Figures 4.6(b) and 4.7(b) demonstrate the modulation at the projection angle. This acts to inflate the results for the 4D limiting spatial resolution as described by equation 4.4. The effect is apparent only in the in silico phantom due to the ideal reconstruction process and the retention of high spatial frequency content in the projections. Modifying the volume threshold has the expected effect of artificially inflating the limiting resolution as can be seen when comparing datasets for which the kernel size was ten or twenty and the threshold changed from 10% to 30% for either phantom.

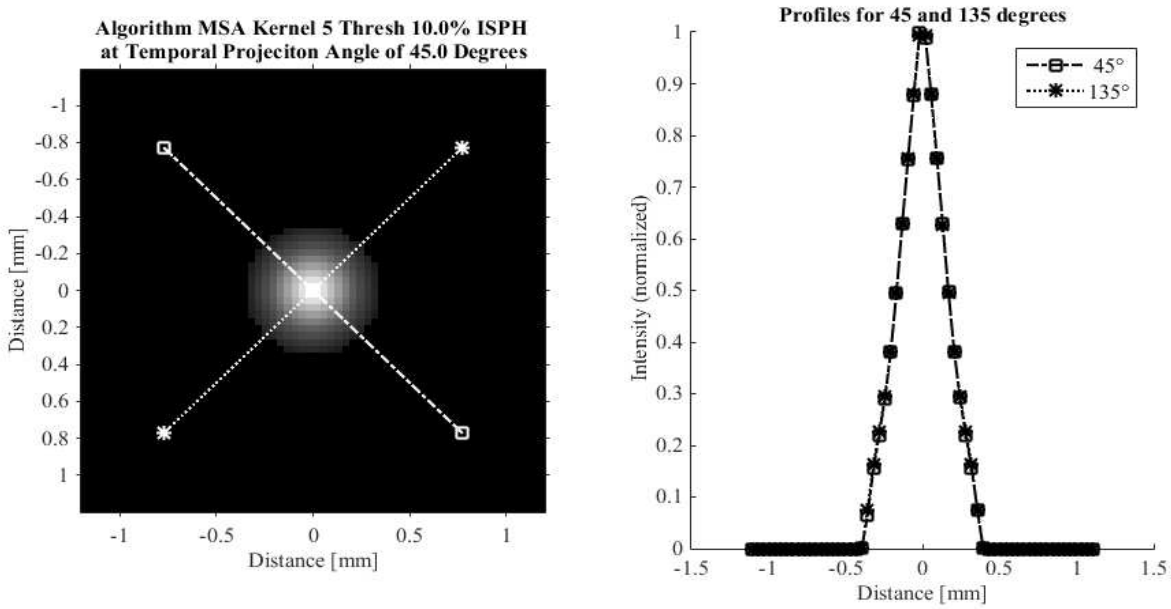

Figure 4.6: In silico phantom profiles of the PSF with kernel size 5 and 10% threshold.

4. Summary

The purpose of this chapter is to convey how the settings of blurring kernel size and the threshold used in segmentation can affect the resolution of 4D DSA. A real-world phantom was designed and investigated to

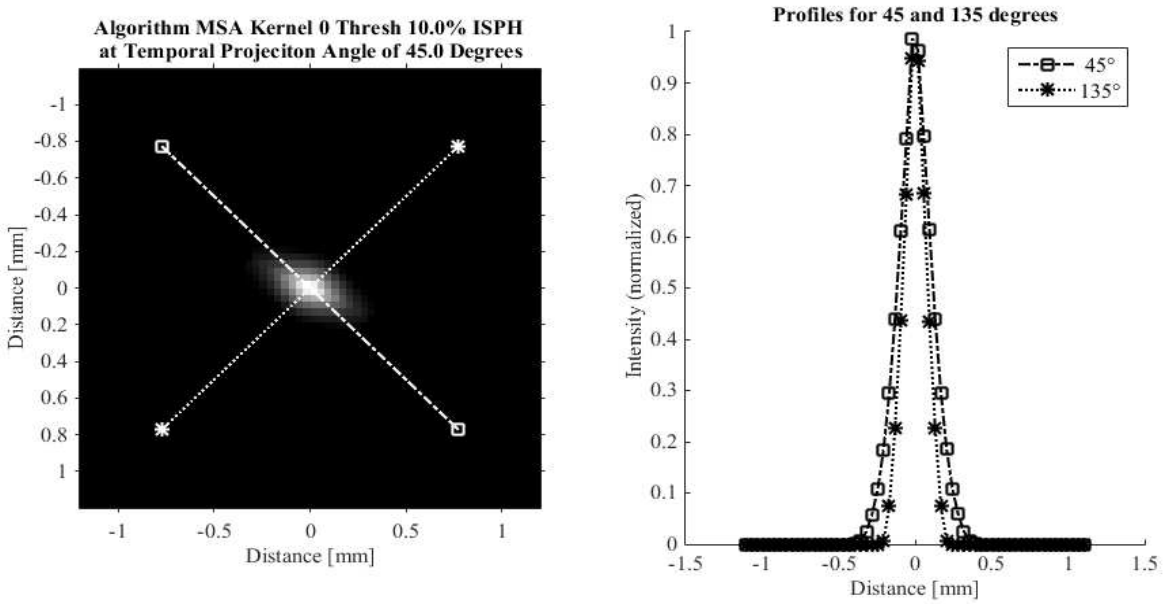

Figure 4.7: In silico phantom profiles of the PSF with kernel size 0 and 10% threshold.

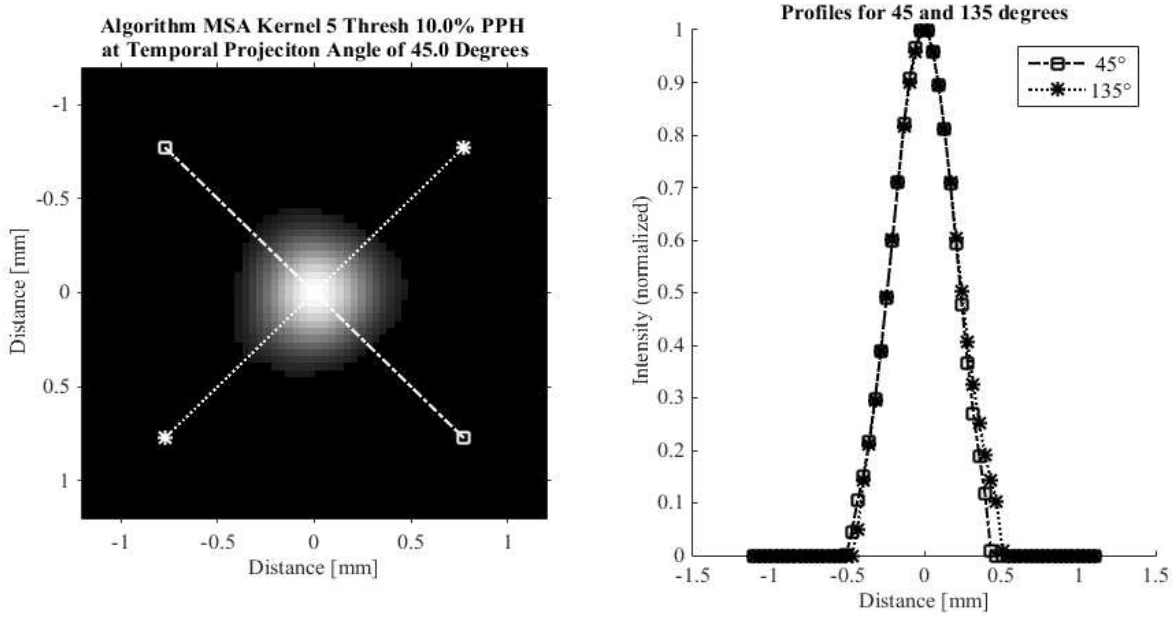

Figure 4.8: Physical phantom profiles of the PSF with kernel size 5 and 10% threshold

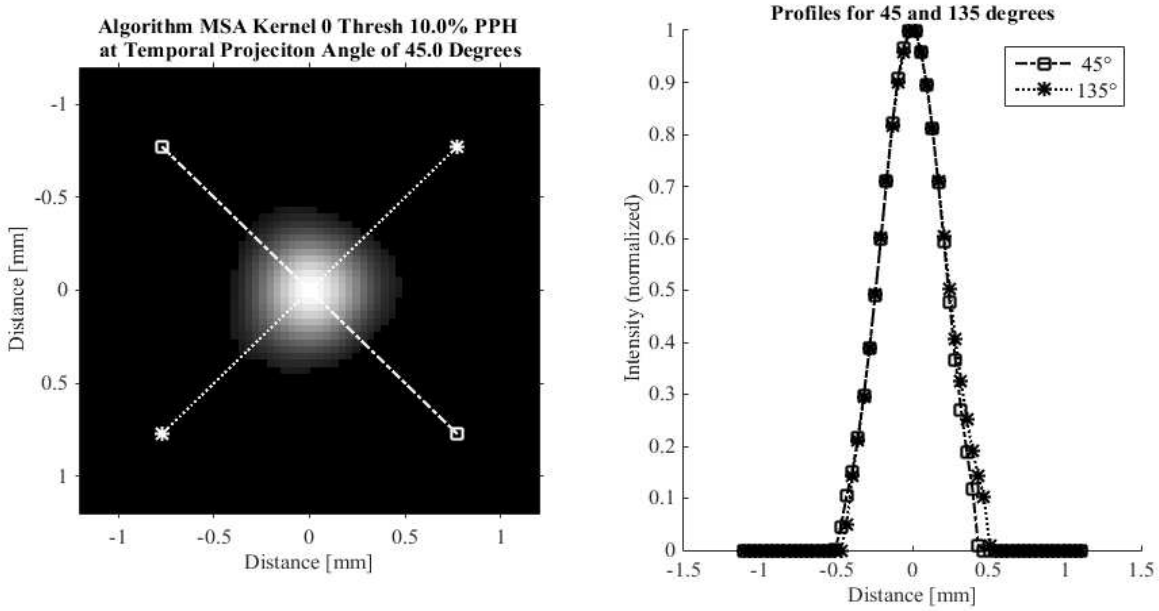

Figure 4.9: Physical phantom profiles of the PSF with kernel size 0 and 10% threshold

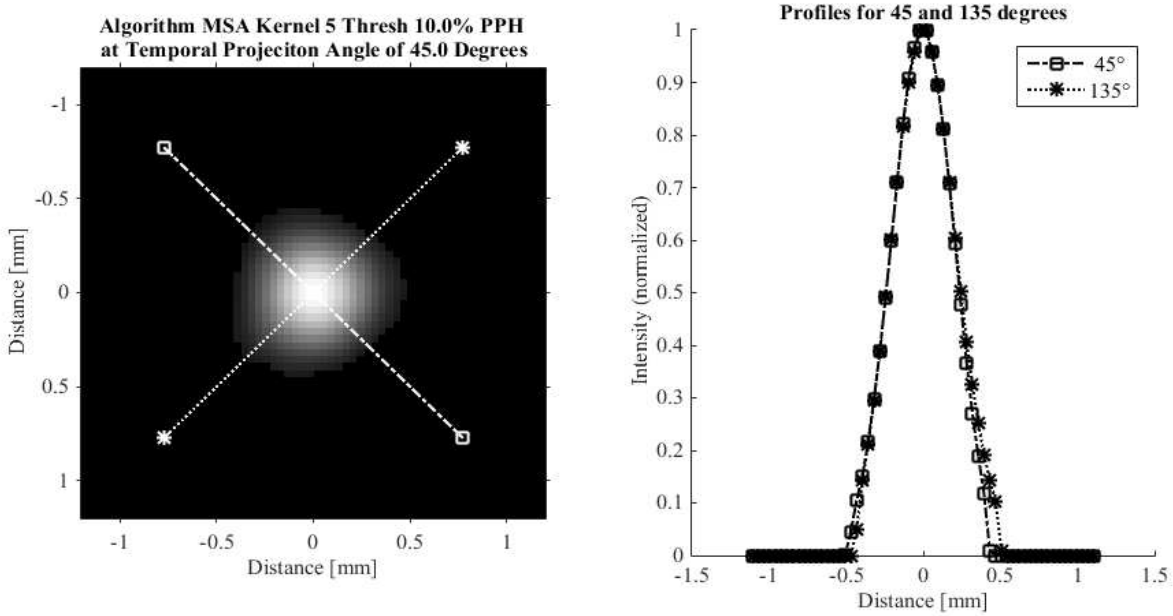

Figure 4.10: Physical phantom profiles of the PSF with kernel size 5 and 10% threshold

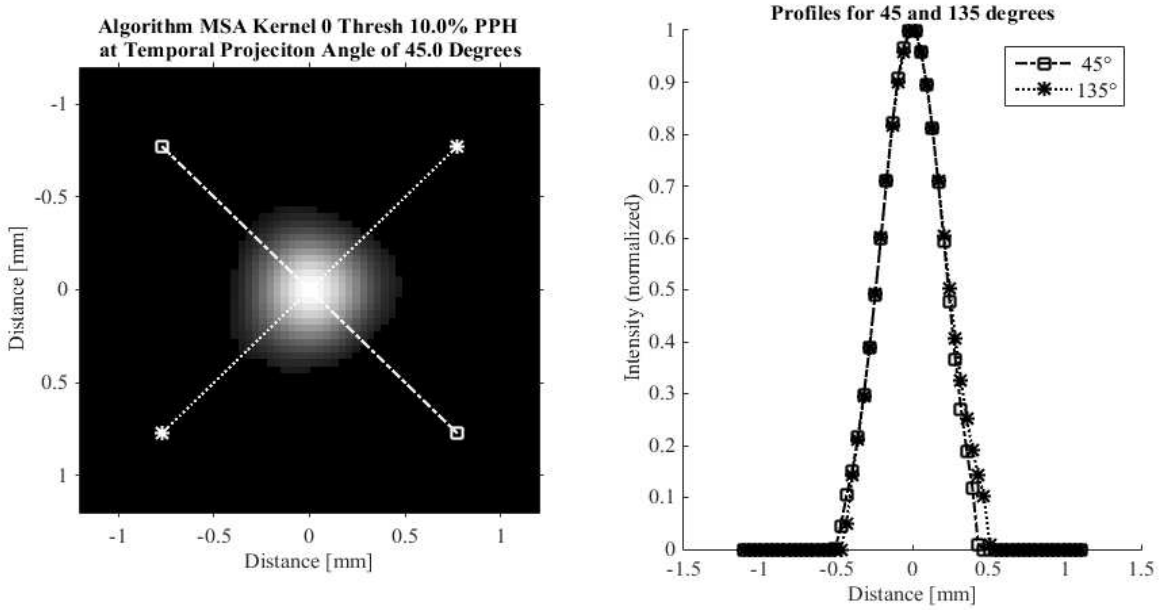

Figure 4.11: Physical phantom profiles of the PSF with kernel size 0 and 10% threshold

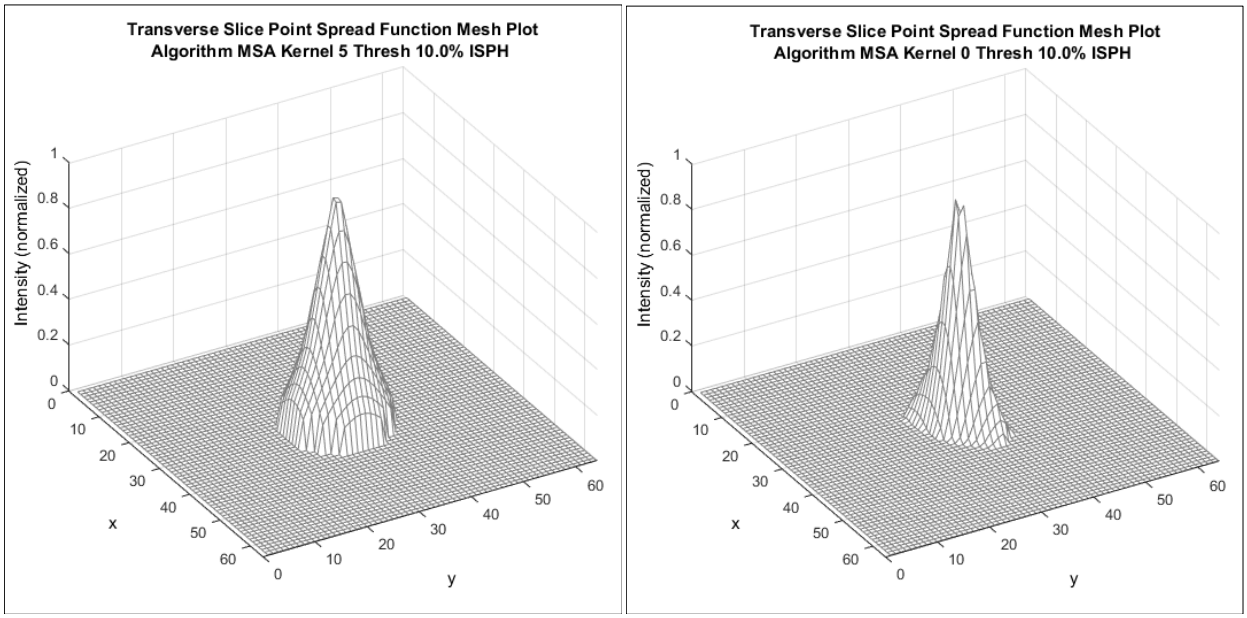

Figure 4.12: In silico phantom PSF mesh plot with a) kernel size 5 and 10% threshold representing an unmodulated PSF and b) kernel size 0 and 10% threshold representing a highly modulated PSF in the direction of the projection angle.

aid in the determination of the resolution of 4D-DSA. The kernel size and threshold were varied over typically used ranges. This chapter walks the reader through the various stages of the reconstruction and discusses the individual stage equations and the effects the various stages have on the overall resulting resolution of 4D DSA. Results are provided for both a scanned phantom and an electronic phantom resulting in obtainable real-world results and results obtained from an idealized silico phantom. The artifact of a highly modulated PSF along the x-ray beam when the threshold is excessive also demonstrates the modulation along the x-ray path. It is shown that so long as the blurring kernel and the threshold are kept within acceptable ranges the resolution of the 4D-DSA can retain the resolution of the 3D-DSA. 4D-DSA is capable of producing a time series of 3D angiographic volumes that have occurred at any time in the scan and from any view angle while retaining the resolution of the 3D-DSA volume. 4D-DSA is capable of providing a resolution of 1.67 lp/mm at a temporal resolution of 30 frames per second using a standard protocol.

5 4D Fluoroscopy Design and Implementation[1]

1. Introduction

While 4D DSA provides enhanced temporal diagnostic capability it cannot be used to perform an actual intervention in the human body. 4D Virtual Fluoroscopy and Endoscopy, on the other hand, have the potential to provide relevant and important interventional device guidance, navigation, path planning, and views not possible through the use of 2D DSA alone to the interventional radiologist. This chapter details the technical aspects of the endoscopic view software visualization process and demonstrates the process is possible in a manner critical to the real time nature of device guidance thus providing the groundwork and justification for evaluation testing.

Before the effort detailed in this chapter, endoscopic views for interventional x-ray angiography machines at the University of Wisconsin-Madison Medical Physics department were post-processed (offline). The accuracy of the 4D fluoroscopy device reconstruction algorithm used in this development effort was reported by Wagner et. al. [39]. An Artis zee biplane as shown in figure 2.1a was used to scan a vascular phantom. The location of the catheter was determined at five different locations. This was done by taking a scan at each point in time the catheter was moved to and then performing an offline reconstruction. The virtual catheter centerline was then reconstructed and compared to the measured centerline from the 3D-DSA reconstructions at each of the five locations. This work was reported in [39]. The study found that accurate virtual device placement can be obtained with an average accuracy of 0.10 $\pm$0.19mm and that real-time virtual fluoroscopic planar views are possible.

The present effort builds on the works of Wagner et al. by adding the capabilities of real-time virtual endoscopy to the existing 4D-fluoroscopy system providing a true real-time 4D-fluorosocpy system with both endoscopic and fluoroscopic capabilities. These efforts produced a fully integrated system capable of path

[1]Portions of this chapter have been previously published in the following journal article: Davis, Brian J., Martin G. Wagner, Sarvesh Periyasamy, Charles A. Mistretta, Charles M. Strother, Paul F. Laeseke, and Michael A. Speidel. "Evaluation of Real-Time Guidewire Navigation Using Virtual Endoscopic 4D Fluoroscopy." In Medical Imaging 2020: Image-Guided Procedures, Robotic Interventions, and Modeling, 11315:1131515. International Society for Optics and Photonics, 2020. https://doi.org/10.1117/12.2549683.

planning, real time navigation, and real time virtual views for the virtual navigation of vascular structures in the human head. The system was tested during the development effort and evaluated based on performance metrics acquired to aid in the determination of the capabilities of the proposed system. Various device navigation features have been designed for Endoscopic view which have become critical to the successful implementation and are discussed in this chapter. The implementation of the algorithms and visualization are described. This chapter reports on the requirements, implementation, and technical evaluation of the 4D-fluoroscopy platform. The chapter that follows reports on the use of the platform described here in simulated clinical tasks.

2. Methods

The creation of 4D Endoscopic view rendering software began first with a requirements gathering phase, then proceeded through the design, implementation, and testing phases. Discussed here in detail are the requirements gathered, the design and implementation of the system, validation experiments run to ensure correct operation, and the analysis of data and metrics to qualify the operation of the system. This research was performed under an institutionally approved animal care and use committee protocol for animals.

2.1 Feature Requirements

Table 5.1: Key requirements of the 4D-Fluoroscopy endoscopic view.

Requirement Description	Metric
Frame Rate	15 fps (times 2x per view) or greater
Time to ready (including human interaction) after 3D-DSA available	2 minutes
Virtual View Types	Down the pipe (endoscopy), glass pipe, and 4D-fluoroscopy
Number of Simultaneous Virtual views	2
Lag (pulse to endoscopy frame)	300 ms
Camera Paths	Vessel network, user defined path, and catheter tracking

The clinical team defined upper-level system user requirements which drove the technical team's development of the platform. The definition of user features defined how the operator would interact with the scene

and mode changes of the endoscopic view rendering software. Workflow requirements from both user and technical perspectives were defined. Key requirements are summarized in table 5.1 and what follows here is a discussion of these key requirements.

- Refresh rate at 30 fps
  - Current interventional x-ray angiography capabilities are 7, 15, or 30 pulses per second. A fps of 30 is only possible when using a single plane and thus when using both A and B planes required for 4D fluoroscopy only 15 fps can be achieved based on the maximum supported fps of existing equipment. This translates to a worst-case frame rate of 15 frames per second [fps]. A pulse rate is the rate at which radiation is generated by the x-ray tube and the image is subsequently acquired by the detector.

- Time-to-ready
  - Time-to-ready is the time from when all data is available from the system to the time that views appear on the screen. Some user interaction is required to allow the user to segment the vascular network for only the regions of interest. The clinical team defined an acceptable time would be 2 minutes. This does not include any time to acquire a 3D volume but rather starts after the 3D volume has been acquired and is available to the software. This time is minimized so as not to add significantly to the overall setup time. Generation of the 3D view is required at the beginning of the procedure. However, allowing the operator to change the threshold of the system to change the generation of the 3D view on the fly during a procedure could overcome any volume artifacts as a result of an initially incorrect threshold setting. This allows the operator to modify the vasculature representation during the procedure either because there is a missing structure (over threshold) or unnecessary structure (under threshold). Another feature is the ability to remove unneeded vasculature from the reconstruction using the volume clip feature. This feature can also add to the time-to-ready.
- Virtual Views
  - The 4D-Endoscopy stage presentents the 3D vascular data in the form of a voxelized 3D data set and is required to generate a 3D view visible from both intravascular and extravascular. The radius of the device may be modified at the operator's request. Virtual fluoroscopy views provide 2D planar projection views similar to those in standard 2D DSA.
- Lag
  - Latency is the period of time between the action of the operator/user and the perceived reaction of the system by the user or the new frame depicting the current state of the real-world system. At 30 fps yields a frame time of $t_{frame} = \frac{1}{30} = 33.\bar{3}$ (milliseconds) and 15 fps provides a frame time of

$t_{frame} = \frac{1}{15} = 66.\bar{6}$(milliseconds). Each time the x-ray system acquires a frame at a rate of 15 frames per second [fps] the prototype system must display the rendered 3D-vascular network and rendered virtual device with a minimum lag time of 300 ms or less. The system needs to generate a frame at a rate of 15 to 30 frames per second (fps) and have a new image latency of 300 ms[65, 66] so as not to be distracting to the user or exhibit excessive delays with a maximum limit of 600 ms[66]. Latencies beyond 300 can lead to hand-eye coordination issues and be disorienting to the operator. These values of latency were derived from telesurgery and provide bounds for a system with human operators in the control loop. The value 15 fps is 66.6 ms per frame thus the allowable lag with no dropped frames. This puts a hard deadline on the real time algorithms of 4D-Endo. The time for algorithms to complete during the 4D-Fluoroscopy stage erodes the allowable 66.6 ms lag time left available for the 4D-Endoscopy stage.

- Number of simultaneous virtual views
  - Early in the project, the virtual views were limited to two (2) to provide at a minimum one (1) 4D virtual fluoroscopy view and one (1) 4D virtual endoscopic view. Timing analysis during the development and testing indicated that 4D virtual fluoroscopy views could be increased to two to provide an additional 4D virtual fluoroscopy view and one 4D virtual endoscopy view.
- Camera paths
  - Vessel Network: The endoscopic renderer provides the centerline data of the device and 3D vascular data. The vessel centerlines were required to be generated before the 4D-Endo entered the real-time phase. The vessel centerline data is used during the real time navigation phase for optional camera placement on the vessel centerline and should allow following of the device tip from this vantage point.
  - User-defined path: The navigation phase requires certain capabilities to be implemented including providing the user the ability to specify a desired path.
  - Catheter tracking: Centerline information is required for the various desired catheter tracking features. Catheter tracking features include 'on centerline look at centerline' (OCLC), 'on centerline look at device' (OCLD), and 'on device look at device' (ODLD) as shown in figure 5.1. It was decided that when the catheter moved outside the wall of the rendered lumen the software should not deform the rendered lumen in any way to provide the same view characteristics as the conventional 2D DSA images.

This requirements gathering led to a design and prototype implementation of the 4D-Fluoroscopy with a Virtual Endoscopy display system.

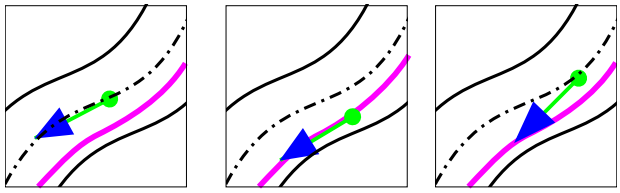

Figure 5.1: Camera tracking modes demonstrating 'on centerline look at centerline'(OCLC), 'on device look at device'(ODLD), and 'on centerline look at device'(OCLD). The green line with a blue arrow represents the eye (green dot) to look at the vector(blue arrow). The magenta line represents the device while the dashed line represents the centerline of the vasculature.

2.2 Technical Implementation

Given the above set of user and design requirements, the next step was to generate a design and the technical methods by which to realize the system. The 3D vascular roadmap is obtained from a pre-navigational contrast-enhanced 3D-DSA. Alternatively, a contrast-enhanced cone-beam CBCT can be used. After the acquisition of 3D data, a 3D DICOM volume representing the vascular network is then sent to the 4D fluoroscopy prototype platform. The external view mode displays this volume data as a maximum intensity projection (MIP). The endoscopic view mode produces a volumetric 3D rendering from a mesh of triangles representing the geometry. This geometry can then be rendered quickly by accelerated 3D hardware. For both viewing modes, a real-time 3D reconstruction of the catheter device from two biplane projections is displayed along with the 3D vascular roadmap. Since the vascular roadmap and live biplane projections are generated with the same imaging system, they are inherently reconstructed in the same coordinate system.

2.2.1 Hardware Components

Components of the 4D fluoroscopy system were implemented on a Windows workstation (Intel Xeon Processor E5- 2697 v2 (Twelve Core HT, 2.7GHzTurbo, 30MB), NVIDIA Quadro K6000 12GB GPU, 64GB RAM) which received live images from a bi-plane x-ray angiography system (Artis Zee, Siemens Healthineers, Forcheim, Germany) using a frame grabber (Vision RGB-E2S 1920x1200, Datapath Limited, Derby England) and vendor-provided interface. The majority of the components were contained in a mobile cart referred to as the Digital Video Processor Four (DVIP4) as shown in figure 5.2. Historically the first generation digital video processor can be found in Kruger et. al. [11, 10]. The output of the system was integrated with the large monitor of the x-ray system, allowing for side-by-side viewing of 2D and 4D fluoroscopy displays. The graphical interface of the system is controlled at table side with a wireless mouse and keyboard.

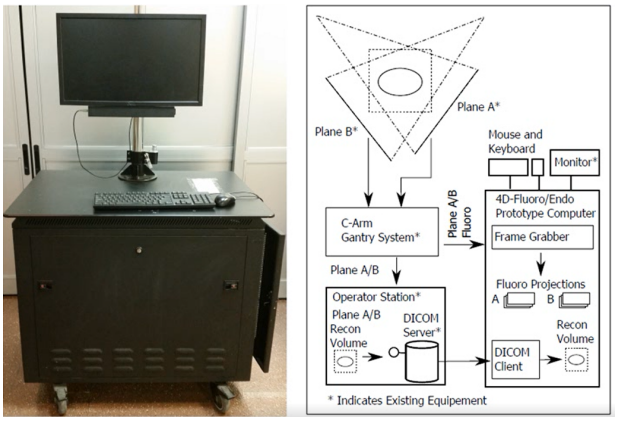

Figure 5.2: Digital Video Processor Four (DVIP4) hardware and system block diagram.

2.2.2 Virtual Fluoroscopy Planes

Frame-by-frame device reconstruction starts with segmenting the device in both 2D image planes to generate point-wise values representing the device in each plane. The 2D DSA fluoroscopy image is created by subtracting an earlier mask image without the device in the field of view from the current live fluoro image possibly containing the device. The resulting image shows the device, any associated noise, and any possible misregistration artifacts. The device is segmented from this image by applying a ridge enhancement filter with local a second derivative followed by binarization with a specified threshold. The centerline of the binary segmentation is then computed with a topology preserving thinning algorithm. A monotonic mapping function is applied to the centerline points of each plane using epipolar geometry to identify corresponding points. A 3D backprojection is performed point by point for each pair of point correspondences to find the intersection. The series of intersection points is then the location where the device is located in 3D[42, 39, 40]. The implementation of this algorithm was provided by Dr. Martin Wagner.

2.2.3 Modular Architecture

The 4D fluoroscopy prototype software consists of an application and a series of plugin modules with the block diagram representing the system shown in figure 5.3. The software is configured using a configuration file specifying which plugins are loaded and what default configuration parameters are passed. For instance, the Live Data Provider is removed by removing its configuration in the configuration file. This can be used to allow a File Data Provider to load previously acquired images stored in DICOM format. These plugins can be grouped into three categories, those relating to 4D-fluoroscopy with an external viewpoint, the virtual endoscopic view, and those relating to utility such as the file and live data provider. The centerline plugin performs the core of the segmenting and determination of the device centerline. The block-

matching registration plugin performs a deformable registration where the image is divided into small blocks and a translation-only registration is performed for each block. Translation vectors for every pixel are then interpolated between blocks[67]. This is done to register the current frame containing the device and anatomy to the mask frame containing only anatomy before subtraction.

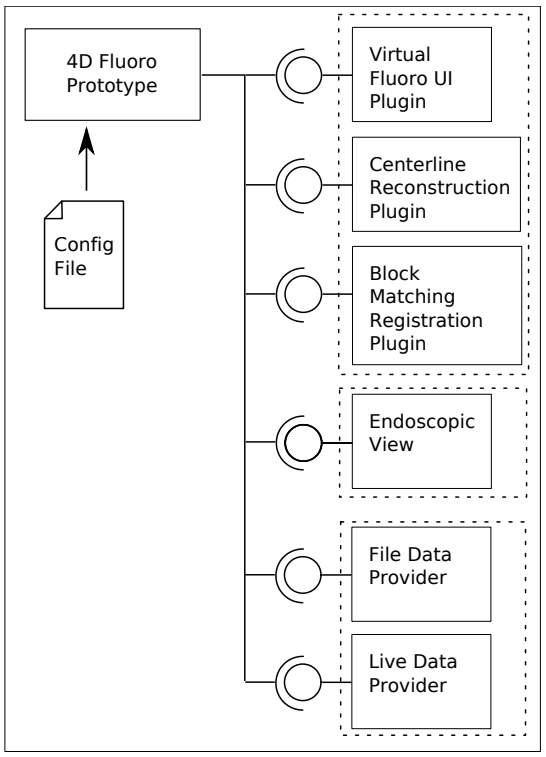

Figure 5.3: 4D fluoroscopy prototype plugin software block diagram.

The modularity of the endoscopic view software also lends itself to being incorporated into test applications separate from the 4D Fluoroscopy prototype software. The endoscopic view plugin provides only a thin software interface necessary to complete the requirements of a plugin as defined by the 4D-fluoroscopy prototype. The endoscopic view software subsystem is shown in figure 5.4. The subsystem is composed of the optional endoscopic view plugin interface, endoscopic view library, textures library, event logger library, shaders library, and OpenGL Shader Library (GLSL) files.

The endoscopic view plugin receives configuration information on startup and allows the user to configure the endoscopy view plugin parameters through a control panel. Changing these parameters also changes the settings in the configuration file. This allowed for quick changes during early testing and no interaction once optimal settings were found. Modifiable settings include vessel mesh, vessel centerline and post-processing, path planning, device centerline including smoothing parameters, color specifications, default isovalue (volume threshold), settings for 3D Gaussian blur of the volume, vessel centerline algorithm settings for both

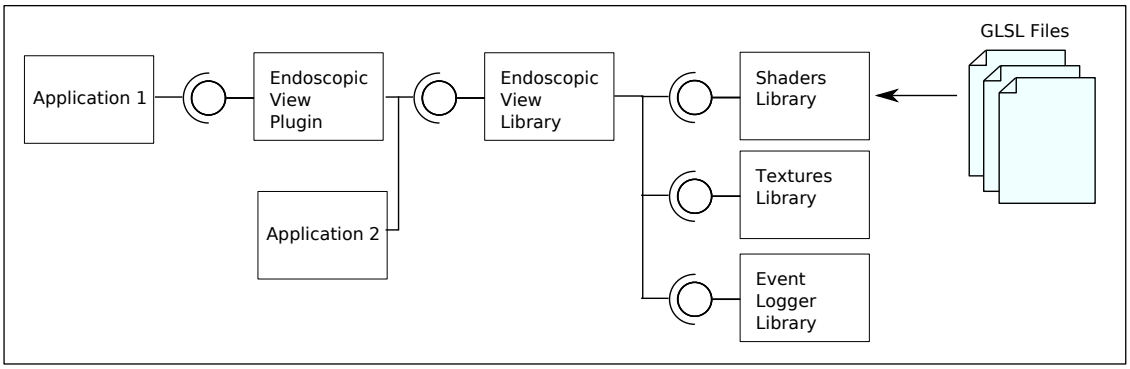

Figure 5.4: Endoscopic view software block diagram.

thinning and optionally VMTK, endoscopy view settings, endo camera placement and tracking settings, camera tracking, camera motion smoothing, endoscopy camera light and ambient lighting, render configuration, shader parameters, and user interface settings.

2.2.4 Isovolume Creation

The endoscopic display software algorithms compute the isosurface of the vascular network (volume) given an automatically calculated but user-adjustable isovalue (threshold). The marching cubes algorithm[68] was applied to the task of generating an isosurface (mesh) of the 3D vasculature from 3D volumetric DICOM files. A modified version of the NVIDIA marching cubes algorithm (NVIDIA CUDA 9.1) was employed to create the isosurface. Modifications include increasing the allowed data dimensions and individual coloring of vertexes. The resulting 3D roadmap is inherently registered to the 3D reconstruction of the device assuming no table or patient motion as it is derived from the A plane of the gantry C-Arm angiography system. Optionally, the 3D roadmap may be generated from other 3D modalities such as MDCT or MRI. Since these modalities are not inherently registered to the x-ray angiography system, a method of manual registration would be required.

2.2.5 Centerline Algorithms

Algorithms investigated for finding the centerline of a vascular network include skeletonization and thinning as well as an approach that utilized Voronoi diagrams for finding centers of maximal inscribed spheres. Skeleton3D[69, 70] and VSK[71] are examples of skeletonization approaches while VMTK[72] is an example of a Voronoi diagram approach. A real-time thinning approach by [73] was also tested and ultimately selected. Decimation of 5 was applied to on the data as the thinning approach produces centerline values

on voxel coordinates. This decimating of the data helped smooth the centerline returned from the real-time thinning approach.

2.2.6 Path Planning

The optional 3D path planning phase aims to provide a visual highlight of the navigational route to be traversed when viewed by the endoscopic virtual display mode. The user is allowed to select a path by selecting points with a mouse. At a minimum, the user can select an origin and destination. The software can then calculate the shortest path. If the shortest path is not the desired path, the user may select way-points between the origin and destination to ensure the path calculated is the desired path. The user interface was implemented with a mix of Win32 UI controls and cursor movements along with a picking implementation allowing the user to rotate, pan, zoom, and select (pick) geometries rendered on the screen.

As the vessel network can be considered a graph with edges and nodes the well-known method of Dijkstra's algorithm (and its variants) can be applied to determine the path along a vessel network. The Boost Graph Library (BGL) in Boost version 1.68 was chosen for this task. Boost Graph provided a means to specify edges and nodes. The implementation then allowed the user to select any two or more points on the graph. The point selection or "picking" was implemented using the OpenGL Mathematics library (glm) version 0.9.8.1. This approach used a model view projection matrix of the current view, the x and y location of the cursor, the two z coordinates of the near and far planes the view frustum, and an unproject function. This allowed the calculation of a ray within the view frustum at the mouse coordinates which could then be used to find the shortest distance between the ray and all points on the centerline graph. The point with the shortest distance to the ray was then the picked point. Picking two or more points then select the desired path. When picking more than two points Dijkstra algorithm was called once for the first pair of points and then successfully on each new point pair in the list. This allowed the graph algorithm to find the shortest path between segments while still providing the user with the ability to select a desired path which may not be the shortest path. The glm library was also used extensively for the user interaction calculations of pan, zoom, and rotate for interactions with the 3D representation of the vessel network (mesh). Once the centerline points were determined the geometry was then fed into the isovolume rendering implementation which used a custom algorithm written in CUDA to find points in the vertices representing the volume mesh closest to the given points in the centerline and change the color of the vertices to the desired path color.

2.2.7 Camera Controls

The endoscopic view implementation required several camera controls. These controls allow the user to freeze the camera in place along the device navigation path at any point along the path, move the camera viewpoint to any angle, and move the camera distal or proximal to the device tip. Camera tracking modes provided are 'on centerline look at centerline', 'on device look at device', and 'on centerline look at device'. The field of view (FOV) can also be changed to provide a narrow or wide-angle lens effect. Various buttons were implemented to allow the user to change the tracking distance configuration including the camera to tip-to-look-at distance and tip-to-eye distance. The 'tip to look at' distance is the distance from the tip to the point along the catheter to look at. The tip-to-eye distance is the distance from the tip to a point along the catheter where the camera (or eye) is located. The vector between these points defines the direction of the view. These variables effectively allowed the camera to be moved towards or away from the tip of the catheter. The tip-to-look-at parameter was found to be a distance away from the tip to aid in minimizing camera jitter. The tip was found to jitter or jump depending on how the tip was interacting with the vessel wall. These key configuration parameters are described in table 5.2. Increasing the tip-to-eye distance allowed more of the device tip to be in view. This setting was used to back off the camera from the tip along the device centerline or vessel centerline depending on the tracking mode.

2.2.8 Camera Motion Smoothing

The camera motion along the centerline data was smoothed using an N-point ($N = 10$) averaging filter. Although this does create a small delay in camera motion relative to the device tip, this was observed only during very rapid movements or times when the catheter became stuck on the vessel wall and broke free quickly.

2.2.9 Rendering

OpenGL 4.3 with OpenGL Shader Library (GLSL) was chosen over the earlier versions of OpenGL to avoid the fixed function pipeline and provide the greatest chance of success due to increased performance and ability to finely control nearly every aspect of the rendered scene. The Shader Library (OpenGL GLSL) provides the ability to control the lighting and coloring of individual triangles given the virtual light sources placed in the scene. The ability to modify the calculation on the incident light ray and color the triangle by applying user-defined calculation provided the capability needed to quickly render a scene. Various shaders were implemented and tested, including Blinn-Phong, Cook-Torrance, and light and material shaders. Ultimately

the light and material shader was selected for use due to the finer level of control it provided for the rendered scene. In addition to the scene rendering there were also shaders implemented for textures to support rendered icons and sprites. Test shaders were also created to draw surface normals to ensure normal averaging was working correctly. Normal averaging allows surface rendering to be smoothed and not have the distinct appearance of lines at the edges of the triangles that make up the rendered surface mesh.

2.2.10 Post Processing Mode

The virtual endoscopic software is also capable of post-processing saved data generated during live real-time cases. This was done to decrease the development iteration time of the software and to provide this capability under normal operation of the software to provide post-case reanalysis or new views of the vascular network. The endoscopic system can run in either of two post-processing modes. The first is where the DICOM fluoroscopy frames are played back through the system with the centerline extraction algorithm operating in the same configuration as when the data was acquired in real-time. This method has the drawback that the bit depth of the data is 14bit whereas the live stream video frames are 8 bit depth. The second is where the endoscopy software plays back the actual data of the reconstructed centerline acquired during the live experiment and operation of the prototype software. This latter approach has the benefit of reconstructing exactly what was reconstructed by the real time pipeline at the time it was first generated.

2.2.11 Hardware Integration and Qualitative Testing

The post-processing mode which utilized the previously acquired DICOM projection data allowed the software to be profiled to determine areas of the code that could be targeted for optimization and greatly reduced the developing and testing iteration time. Rendering issues were also fixed using this mode as the system could be paused and the plugin nature of the OpenGL Shader implementation allowed shader code changes to be reloaded and viewed instantaneously. Centerline algorithms were tested and debugged in this mode along with the catheter tracking algorithm. The post-processing mode ran in nearly identical time frame rates allowing camera smoothing algorithms to be written, tested, and debugged. During this effort test shaders were developed and tested. Test catheters and guidewires were also used to check device tracking and determine a configuration that could be used in operator testing.

Various machine imaging parameters were investigated to as to provide the reconstruction algorithm with an optimal image. This was challenging due to the limited 8-bit depth of the obtainable image from the vendor-supplied hardware and imaging acquisition pipeline used. The optimal settings were determined as

shown in table 5.2. Injector testing was performed during the qualitative hardware integration testing to ensure the phantom could be opacified to create a 3D vascular roadmap. Manual hand injections were also performed to ensure both 2D and 4D roadmaps could be created using the phantom.

2.3 Experiments

The development process requires a series of experiments to be performed to ensure performance metrics were obtained, test the system, and acquire needed settings for use. A 3D-printed aneurysm phantom was scanned in 3D-DSA mode to validate that a 3D vascular roadmap could be generated, received, and rendered by the endoscopic view plugin. The scan was performed using a 50/50 solution of Iohexol contrast agent and water with a 5-second injection at 3.0 mL/sec for a total of 15 ml contrast and water mixture with a 2-second x-ray delay. The 3D DSA protocol was a Neuro 5-second rotation protocol. Having used the post-processing mode to develop the isovolume rendering, it then required testing in the lab. This also tested the sending of the volume via DICOM to the prototype to ensure the endoscopic plugin received the volume and displayed it correctly. Also tested were the correct orientations of the mouse relative movements or user controls. The volume appeared in the endoscopic view plugin and could be manually adjusted in realtime at the correct orientation.

Catheter tracking tests were also performed. This required the use of multiple phantoms and the development of prototype phantoms using 3D printing technology. Prototype phantoms were used to test catheter movement and binding. During this testing, excessive camera jitter was caused by interactions with the vessel wall when the catheter would catch or snag temporarily. This led to the development of a setback distance from the catheter tip referred to as tip-to-look-at distance and a determination of the tip-to-eye distance. Tip-to-look-at distance and tip-to-eye distance were determined and are stated in table 5.2.

Table 5.2: Key configuration variables used in the experiment.

Group	Configuration Parameter	Value	Units	Description
Application	calibration offset (x,y,z)	(0,0,0)	global coordinate	The number of edges of the polygon to be extruded along the path to form the centerline.

Table 5.2: Key configuration variables used in the experiment.

Group	Configuration Parameter	Value	Units	Description
Path Planning	picking distance threshold	50	global coordinate	The number of edges of the polygon to be extruded along the path to form the centerline.
	sprite size	32	2D Pixels	The size of the sprite to draw in 2D pixels for picked targets.
	target sprite size	32	2D Pixels	The size of the target location sprite in 2D pixels at the end of the selected path (target location).
Device Centerline	number of edges	10	global coordinate	The number of edges of the polygon to be extruded along the path to form the centerline.
	radius	0.25	global coordinate	The radius of the polygon to be extruded along the path of the centerline.
	calibration offset (x,y,z)	(0,0,0)		A corrective offset that could be applied by the endoscopic view software to further correct for any calibration offset required to register the centerline.
	centerline algorithm mode	1	N/A	Configured to smooth the device centerline using a N-point average
	centerline algorithm N-point average setting	10	N/A	Performs an N-point average using N=10.
Volume Algorithm	Gaussian blur sigma	1.5	N/A	Performs a 3D voxel wise Gaussian blur on the volume

Table 5.2: Key configuration variables used in the experiment.

Group	Configuration Parameter	Value	Units	Description
Centerline Algorithm (thinning)	thread timeout seconds	15	seconds	Duration for the thinning logarithm to perform calculations prior to being stopped if errant execution were to occur.
	max segment length	50	global coordinate	The maximum straight line segment length before beginning a new segment.
	smoothing span	0	global coordinate	The number of values that are averaged using a centerline smoothing block filter
	multi threaded	true	Boolean	Allow the implementation to run in multi threaded mode.
Endoscopy View	cam on device look at device (tip-to-look-at/tip-to-eye)	5 / 15	global coordinate	When in “cam on device look at device mode” these parameters are used for locating the camera relative to the device tip/end.
	cam on network look at network (tip-to-look-at/tip-to-eye)	5 / 15	global coordinate	When in “cam on network look at device mode” and “cam on network look at network” these parameters are used for locating the camera relative to the device tip/end.
	UI camera tracking (tip-to-look-at/tip-to-eye)	0.2/1.0	global coordinate	

Table 5.2: Key configuration variables used in the experiment.

Group	Configuration Parameter	Value	Units	Description
	UI camera tracking (pan x/pan y)	0.1/0.1	global coordinate	Pan the camera of the calculated location so as to account for the device or centerline diameter so view is from the outside of device or centerline and not form inside the device/centerline.
	temporal filter N	15	frames	N-point filter the camera tracking position changes.
Endoscopy Camera	near plane	0.1	global coordinate	The distance to the near plane of the view frustum from the camera
	far plane	512	global coordinate	The distance to the far plane of the view frustum from the camera
	field of view	90	degrees	The field of view angle of the camera.

Once the reconstruction parameters could be optimized and the device reliably reconstructed the navigability of devices then needed to be determined. Various phantoms were used with devices to determine the usability of the system. Devices tested included those from expired stock to determine the size and features of the device. This then led to the specification of devices to be ordered to have as consistent and repeatable results as possible among different evaluators of the system.

3. Results

The development effort of 4D endoscopic view (4D-Endo) resulted in the implementation of a real time endoscopic view for use with a bi-plane x-ray angiography system. The primary result of the effort was the endoscopic view plugin which integrates with the existing 4D-fluoroscopy software. The key result is the displays of the software renders as shown in figure 5.5. This display consists of three primary sections

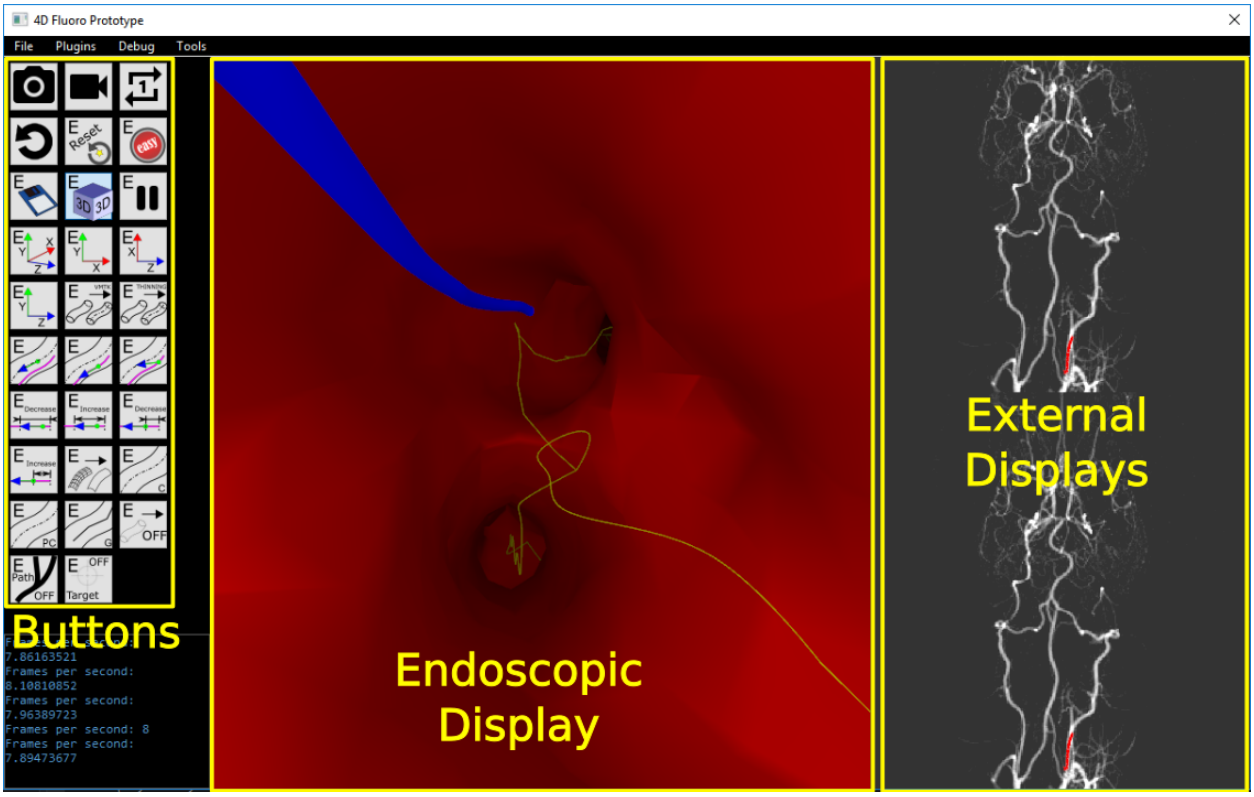

Figure 5.5: Prototype software user interface.

including the user buttons, the endoscopic display, and the two 4D fluoroscopy displays. The path planning capabilities are demonstrated in figure 5.6. The figure demonstrates path planning with a shortest path versus non-shortest path approach. Endoscopic view configuration parameters were 5x decimation of points returned by the thinning operation, N point averaging of the centerline with an N of 10, and a temporal filter of 15 frames to aid in smoothing the camera motion and removing jitter while still retaining responsiveness.

The 4D-fluoroscopic prototype was found to achieve a frame rate of more than 30 fps. Timing results for the various stages of data acquisition and processing by both hardware and software are shown in figure 5.7. The various components of the system are grouped by hardware and software. The hardware components are the detector, vendor-specific hardware, and the frame grabber. Software components consist of the frame grabber driver, frame processing, reconstruction, and finally the display plugin. The maximum achievable frames per second is 38.6 if only the software components are considered and are reduced by any latencies of vendor-supplied hardware. The maximum frame rate was measured based on the processing time of various stages of the software from the time of frame availability from the capture card to the time the frame has been rendered and displayed to the user. Currently, the bit depth is limited by the vendor-supplied hardware DVI interface.

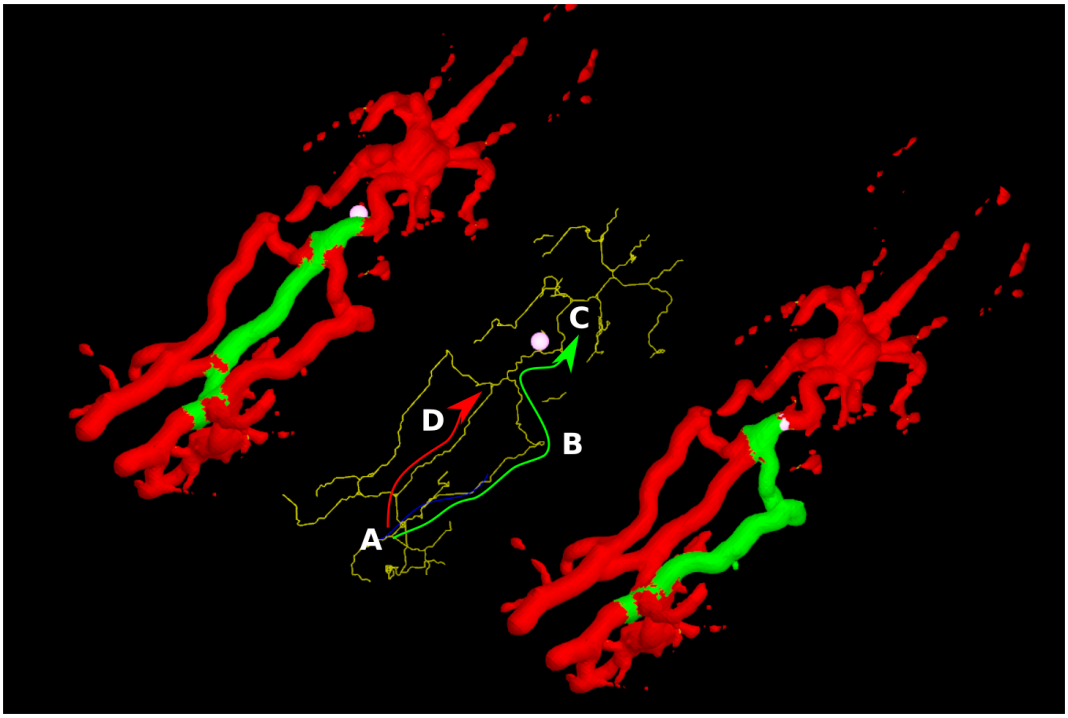

Figure 5.6: The path planning stage works in conjunction with the endoscopic visualization allowing the user to select and visualize the desired path both externally and from within the vessel. The vessel wall is shaded red for vasculature not on the planned path and is shaded green for vessels on the planned path. When selecting a path using just two points the path may not be the desired path as the shortest path between two points is calculated using the Dijkstra shortest path algorithm such as the selected points A and C yielding a path A, D, then C. However the path planning software allows the user to specify waypoints such as point B allowing the planned path to be A, B, then C which is the desired path the device shown in blue is traversing. The path coloring is retained when switching to the endoscopic view internal to the vessel lumen. Shown top left is the shortest path and the user-defined path with an added way-point is shown bottom right.

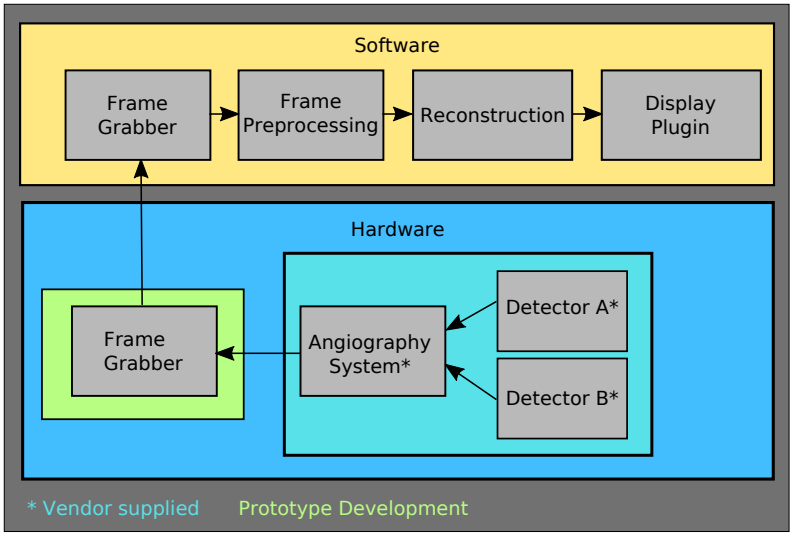

Figure 5.7: Hardware and software pipeline.

Table 5.3: 4D fluoroscopic prototype hardware and software metrics

Component	Resolution	Bit Depth	Component Latency (ms)
Manufacturer Hardware	-	8	-
DVI Interface	512 x 512	8*	-
Frame Grabber (Hardware)	512 x 512	8*	-
Frame Grabber (Software	512 x 512	8*	1.09
Registration, Collimation and Other Processing Plugins	512 x 512	8*	0.47
Reconstruction	512 x 512	8*	15.19
Display Plugins	512 x 512	8*	9.17
Data Cleanup	N/A	N/A	0.01

* Limited by the manufacturer hardware and frame grabber interface.

4. Summary

This chapter describes the design and implementation of the real-time 4D-Fluorosocpy and 4D-Endoscopy system. Various requirements of the system were documented. The system design was described and the various user interfaces were documented and shown. Key software modules including marching cubes, centerline generation, network graph for path planning, rendering, and user interface controls were detailed. The modes of camera tracking including camera 'on centerline look at centerline', 'on device look at device', and 'on centerline look at device' as well as camera control was explained. Camera control includes the capability to move distal and proximal to the device tip, freeze the position of the camera, and manually change the viewing angle. The key metrics of resolution, bit depth, and latency were elaborated upon. The maximum achievable frame rate given the manufacturer's hardware is 38.57 frames per second. It has been shown a virtual 4D fluoroscopy with an endoscopy display system is realizable and can meet latency requirements for use in the angiographic suite. The design of a fully functional real time 4D Virtual Endoscopic display for use on a bi-plane x-ray angiography machine has been demonstrated. Also demonstrated was the ability to perform path planning to visualize to the user the desired path to navigate when in endoscopic view. The following chapter explores the performance of the system from an operator's perspective.

6 4D Fluoroscopy Evaluation[1]

1. Introduction

The previous chapter focused on designing, implementing, integrating, and testing the endoscopic view plugin with modified versions of the existing 4D-fluoroscopy software. Described here is the evaluation of the system as a whole in catheter navigation tasks. A mock interventional procedure involving the navigation of endovascular devices through branches of a vascular phantom was designed to evaluate the performance of navigational tasks when using the system. Metrics were defined to compare and contrast the gold standard of 2D DSA alone with the combined 2D DSA, 4D virtual endoscopic view, and 4D virtual external view. The metrics and user feedback acquired aided in ascertaining the utility of 4D endoscopy/fluoroscopy. Qualitative results obtained from a survey of the participants' responses based on a Likert scale provided insight into the use of the system. System performance and task difficulty were evaluated from quantitative metrics derived from a semi-automated analysis of post-processed video recordings taken during the experiments. Using the phantom in the experiment allowed the reduction in variability often present in animal testing, thus providing a consistent platform to the participants.

A portion of this work targets the system's ability to allow an operator to obtain a goal using virtual real time imaging. Reported in Mauri [74] is the evaluation of a real time ultrasound CT/MRI virtual image fusion to guide the thermal ablation of liver tumors that are undetectable when using ultrasound alone. A virtual navigation and guidance system, Virtual Navigation System, Esaote S.p.A, Genova Italy, was used, correctly targeting 95.5 percent of tumors. This demonstrates that virtual image fusion methods like those reported here can be effective if done correctly. That patient study treated 1581 tumors in 987 patients. In that study, success was tied to whether or not tumor ablation was successful. As reported in the literature, that study is an example of a successful virtual real-time navigation system with a human-in-the-loop.

[1] Portions of this chapter have been previously published in the following journal article: Davis, Brian J., Martin G. Wagner, Sarvesh Periyasamy, Charles A. Mistretta, Charles M. Strother, Paul F. Laeseke, and Michael A. Speidel. "Evaluation of Real-Time Guidewire Navigation Using Virtual Endoscopic 4D Fluoroscopy." In Medical Imaging 2020: Image-Guided Procedures, Robotic Interventions, and Modeling, 11315:1131515. International Society for Optics and Photonics, 2020. https://doi.org/10.1117/12.2549683.

In the Mauri work, no user evaluation via surveys was reported. However, Royalty [19] reported the evaluation of 4D-DSA quantitatively and qualitatively, including user surveys asking participants to rank the effectiveness of the 4D-DSA approach. However, a similar approach is taken here, with the difference that participants provided feedback by evaluating the system using questions based on a Likert scale. These surveys are essential to guide the research in a practical direction. The work reported here combines quantitative task completion metrics and qualitative user feedback to evaluate the system comprehensively.

2. Methods

To evaluate the virtual 4D-fluoroscopy system, a 3D-printed phantom was first developed. Protocols provided consistency in the setup, configuration, and user experience during the evaluation experiments. The participant was then trained on the system. In order to capture and quantify the user experience, a series of cameras recorded the participants' interaction with the system. Developed software tooling provided semi-automated analysis of the video recordings. The navigational study consisted of having each operator participate in two experimental segments. In the first segment, termed "4D-assisted", the operator was presented with conventional 2D and the new 4D displays with both virtual endoscopic and external viewpoints. In the second segment, termed "2D-only", the operator was presented with only conventional 2D displays for image guidance.

2.1 Experimental Setup

The experimental setup consisted of a systolic pump, an injector pump, Siemens Artis Zee Bi-plane, custom cylinder phantom housing, and vascular phantom. The cylinder phantom housing supported the vascular phantom and allowed water to fill between the cylinder wall and the vascular phantom. The water fill allowed physical simulation of the x-ray attenuation similar to that of a human head. The experimental setup is shown in figure 6.1. The pump provided fluid circulation through the phantom, while the injector pump provided metered remote contrast and water injections during the roadmap volume acquisitions. All other injections were performed manually by the participant using a syringe. The 4D fluoroscopy system consists of four components: i) a 3D vascular roadmap of the vessels of interest, ii) an optional planned path through the vascular network, if desired, iii) a live view of the endovascular device reconstructed from the two 2D live views of the biplane fluoroscopy system, iv) a virtual camera viewpoint and method of displaying the device relative to the registered roadmap in real-time.

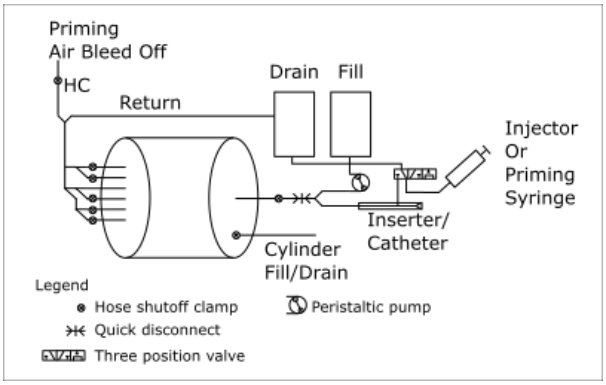

Figure 6.1: Cylinder phantom housing fluid schematic.

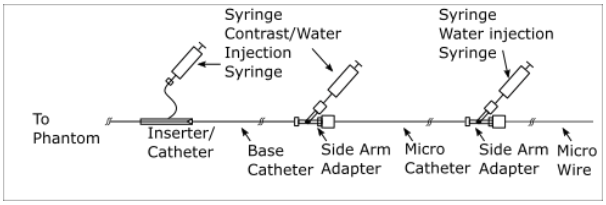

Figure 6.2: Device configuration.

The phantom housed within the cylinder phantom is shown in figures 6.3 and 6.4. The cylinder was mounted on the head holder with spare tubing and taped to help affix the phantom. The phantom, pump, and fill and drain buckets are shown in figure 6.4. The injector was moved near the pump and located on the back side of the table when needed.

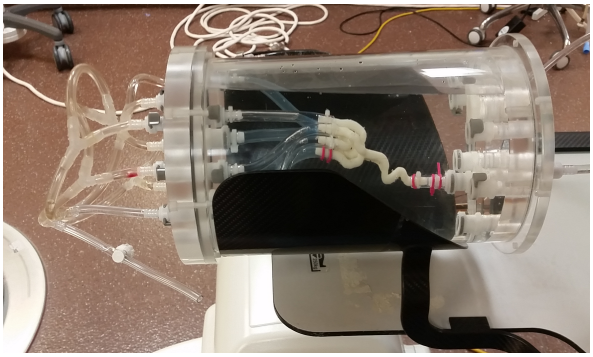

Figure 6.3: Endoscopy carotid three parallel tortuous phantom.

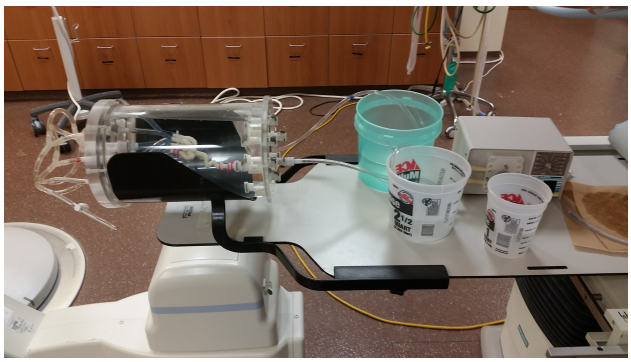

Figure 6.4: Phantom and pump configuration shown in relation to fill and drain buckets. .

2.2 Workflow

The process workflow consisted of two primary phases with one optional phase. The first step in the process workflow is the 3D vascular roadmap generation phase. The vascular roadmap is derived from a contrast-enhanced 3D-DSA volume. The 3D-DSA was created using Omnipaque Iohexol contrast agent (300 mgI/mL) diluted 50/50 with water and injected at 3ml/s for 5 seconds with a 2-second x-ray delay. During the optional path planning phase, the user can optionally modify the isovalue (threshold) used to generate the isovolume to remove any noise that can create false rendered vasculature. The user would then command the software to create the vessel centerlines. With the centerlines generated, the user can select the path

along the vasculature from the start to the end, with optional waypoints selected along the path. The navigational phase is the second primary phase. During the navigation phase, a peristaltic pump circulates water through the vasculature to simulate ambient blood flow. After the first navigational task, additional navigations were performed. Additional navigations used the original 3D-DSA, but participants were allowed to define (optionally) a new path plan.

2.3 Phantom Design and Realization

The phantom was modeled after patient-specific features of a human cerebral AVM case, as shown in figure 6.10a. The features of the vessel geometry were specifically chosen based on the complexity and difficulty of obtaining 2D fluoroscopic images at appropriate view angles. These features included a winding carotid segment, a section containing vessels that run parallel and coincident with other vessels, and a tortuous segment for which obtaining nonoverlapping working 2D projections is challenging. The carotid segment bifurcated into the parallel segment, while the parallel segment bifurcated into the tortuous segment. The trifurcations and bifurcating of the vessels in the 3D printed phantom were designed to provide multiple paths, test the path planing features of endoscopic view, and provide operators with views of multiple (2) vessel branching types.

The phantom was designed and realized through a series of steps. A design pipeline consisting of Blender [2.74], MeshLAB (version v2016.12), MATLAB 20118b, and Materialise Mimics, Materialise 3-Matic. The process of developing the phantom consisted of 1) acquiring a clinically relevant data set, 2) mesh in MeshLAB and exporting to STL, 3) importing STL in Blender and creating spline (tubes), 4) exporting spline data from Blender using custom script, 5) import spine data into MATLAB and voxelize, 6) import voxelized phantom into Mimics to remesh for export to 3-Matic, 7) use 3-Matic to thicken mesh (add vessel wall) and attach ports for fill and drain, 8) export STL for printing, and 9) 3D print part on Formlabs Form2 or Stratasys uPrint SE Plus. The printed phantom was then sprayed with enamel paint to seal micro-pores and placed inside an 8” outer diameter water-filled cylinder fabricated from acrylic shown in figure 6.1 Blender was used to create centerlines conforming to, or similar to critical vascular structures such as the carotid section, three parallel, and tortuous segments. Due to the required scale of the final product, the features were not direct copies of exact vascular structures, and a certain level of artistic license was employed. This was necessary as it was discovered on early prototypes that device navigation would be difficult due to the binding of the device with the rigid vascular wall. Deviations included straitening and shortening the carotid section, placing the parallel segments more in line, and collocating and free-handing the tortuous segment.

The phantom must also be realizable with current prototyping and manufacturing capabilities. The phantom

was test printed and prototyped on a Formlabs Form2 SLA printer. Due to the phantom design of the tortuous segments, it became difficult to create them on a Form2 3D printer without requiring the phantom to be printed in two parts and glued together. Therefore, the final phantom was printed on a Stratasys uPrint SE Plus and then sprayed with enamel paint. The enamel paint was required to seal micro-pores, as shown in figure 6.5 in the vessel wall, which are artifacts of the printing process at the needed scale and were visible on micro CT scans of the phantom.

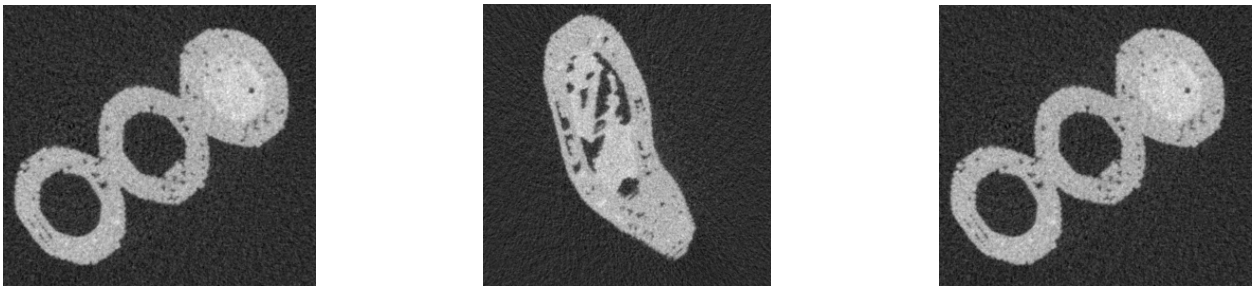

Figure 6.5: Micro-CT of prototype phantom printed using a Stratasys uPrint SE Plus

2.4 Video Acquisition of the Participant Experience

Two cameras captured the live x-ray display monitor and a view of the participant's interaction with the devices and phantoms. The camera facing the monitor was a GoPro Hero Silver. This camera was mounted on the operating light to allow easy repositioning. A Canon A1100 oriented to face the participant captured interactions with the devices. This tripod-mounted camera was located at the end of the patient's table. These table-side actions included interactions with controls, catheter, and contrast syringe injections. Captured audio provided verbal feedback from the operator throughout the experiment. A transcript of the audio was manually created and saved with the event log file. Figure 6.7 shows an example of the manual log file.

2.5 Quantitative Metrics

Post-processing of video recordings provided quantitative metrics of the study. Semi-automated video analysis using MATLAB provided metrics of total imaging time per task, total task time adjusted for pauses between imaging runs, total air kerma per task from both C-arms, and the number of pedal presses per task. A master timeline provides specific vital events, including navigation start and stop; experiment holds events such as allowing a participant to ask a question; path planning events; device insertion or removal; contrast injections; video recording events; camera shaking; battery change events; and instances where video regions-

of-interest needed to be specified. Regions of interest are areas on the x-ray system monitor relative to and selected in the video frame in which video processing metrics can be applied or require further analysis by the reviewer. Updates to the position of the regions of interest occurred due to inevitable shifts in camera position relative to the x-ray system monitor due to either movement of the monitor by the participant, replacement of camera batteries, inadvertent movements of the camera due to bumps, or movement of the x-ray shield. The x-ray shield shared the mount with the operating light to which the camera facing the x-ray system monitor was affixed. Thus, disturbances to the relative position of the x-ray system monitor and the camera provided a time point where the region coordinates in the video frame could be specified. The manual timeline also contained comments and interactions with the researchers during the experiment. This transcription provided a quick reference, providing text search to associated video and time instance referencing. An example of manually entered master timeline data is shown in figure 6.7.

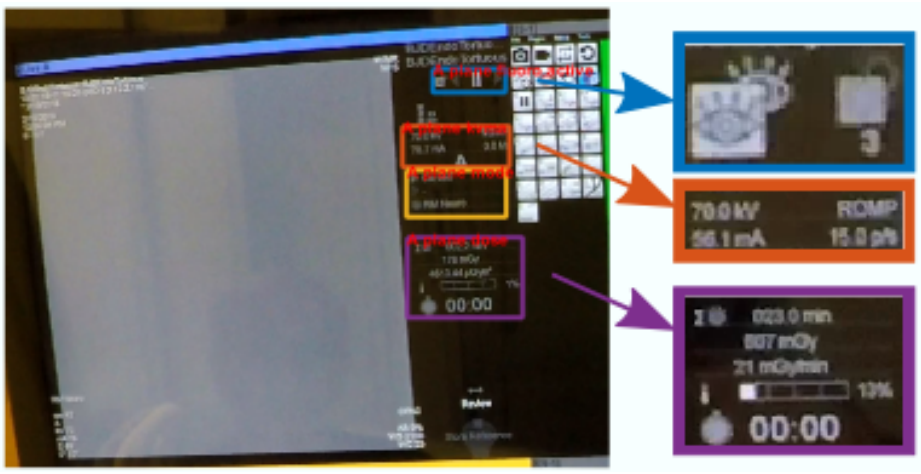

Figure 6.6: Key image regions of a single video frame, including x-ray on/off (blue), kV and mA (orange), and the interventional reference point kerma (purple) selected during the semi-automatic processing of the video. Note for the RAD on/off icon, two of the the three states grouped as on, off, and dark (no icon) are shown.

Five regions (shown in figure 6.8a) of interest were determined, including the fluoroscopy active / pedal press icon region, the kV and mA region, a region containing dose information, the endoscopic view image, and the 2D fluoroscopy plane A view. The regions can be selected in MATLAB in every frame, as shown in figure 6.8c. Each region can be displayed and processed separately, as shown in figure 6.6. Processing can then be performed on the regions of the image and merged with manually entered master timeline data. The software written in MATLAB extracted and classified image regions in the video feed, as shown in figure 6.6. The video was processed frame by frame. Image classification of x-ray on/off state was performed on up to three video regions. The radiation dose (reference point kerma) reported by the system was determined by

manually reading the value and recording it in the timeline using the timeline-derived x-ray on/off states. Due to camera focus, distance, and resolution or obstruction of the view at the time instance these dose values became challenging to read in a single image. Therefore, a utility was created to view the video just prior to and after the time selected time frame, allowing the reader to view multiple images surrounding the time point in question to obtain an accurate reading for radiation dose.

Regions of interest were determined by opening a grayscale converted frame in Inkscape and drawing boxes of various colors to indicate the different regions. These differing regions could then be easily found automatically by the color-mapped pixels which were not grayscale values (R=B=G) in MATLAB. The gray scale regions provided a mask image, and the MATLAB implementation of the bwlabel function provided each region's label (number). The region coordinates were extracted. These region coordinates were then mapped to names using a translation table from name to region id to region coordinates. Only critical regions were selected, labeled, and processed, as shown in figure 6.8b. There were different region sets based on the experiment segments 4D or conventional 2D as the screen layout varied due to the location of the 4D fluoroscopy and endoscopy user interfaces.

	A	B	C	D
1	Time	Event	State	Description
2	0:00:00	GOPR0559.MP4	start	12/4/2018 7:30
3	0:00:00	SEGMENT_4D	start	
4	0:00:00	GOPR0559_IMAGEREGIONS	event	
5	0:13:29	P1_A	start	start duration 17:42
6	0:22:00			in Path planning begins

Figure 6.7: Example of manual timeline entry. The description field contained transcriptions of interactions with the participant to record feedback and user experience.

The image frames provided metrics for both the pedal presses, allowing the generation of automatic digital timeline signals. The automated video processing required the manual review of the videos to determine when path navigations began and when the participant reached the target. The automatic detection and classification approaches failed for some images, requiring a manual classification tool to be created for unclassified images, as shown in figure 6.9. This tool allowed the classification of images based on 'is dark', 'active', 'inactive', or 'unknown'. Dark images indicated a transition between icons, active indicated pedal press was 'active' / RAD on, 'inactive' indicated the pedal was not depressed / RAD off, and unknown was used for indeterminate states where the icon was between states due to camera image ghosting effect. The unknown states are shown in one image in figure 6.9 in the fifth column and fifth row. Manual classification then changed the state to either 'pedal active', 'pedal inactive', or 'unknown'. Sometimes, the image metric used to determine dark frames would fail when no icon was present. Therefore these moments were classified manually and labeled 'is dark'. This manual timeline data and automated video processing timeline data were fed into a timeline processing code to generate digital signals for the events. These events included

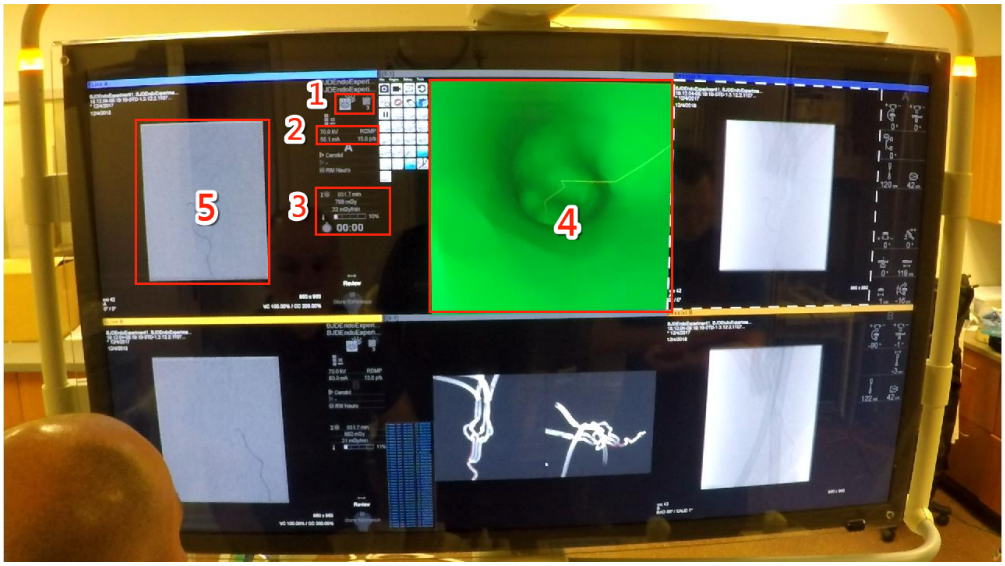

(a) Video frame regions of interest include 1) Pedal depressed / Fluoroscopy active icon, 2) KV and mA, 3) does information 4) endoscopic view, and 5) 2D plane A view.

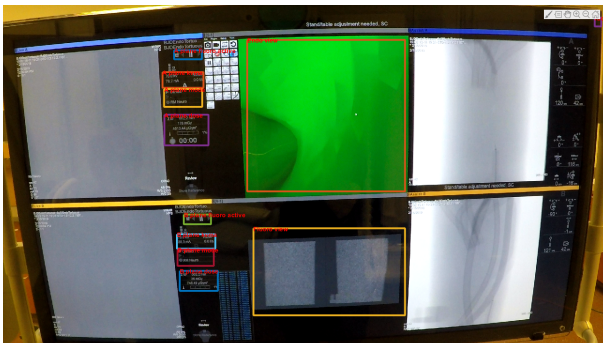

(b) Selected and labeled regions of interest.

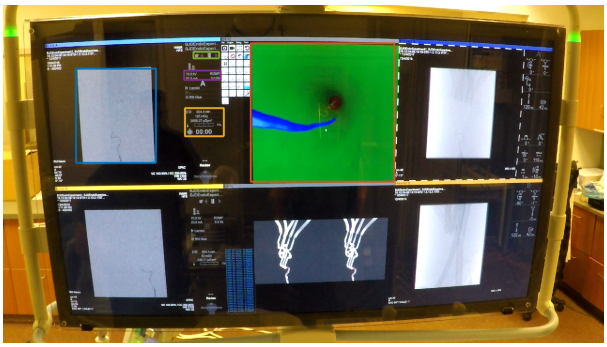

(c) Regions are automatically drawn in MATLAB using regions defined manually.

Figure 6.8: Extraction and event generation of video regions.

events for each path A through E, and pedal presses. The digital signals were then combined to generate a mask of the timeline of the automated video data with the manual path events A through E to extract just the metrics as they applied to the path navigations, thus excluding any setup time prior to the navigation task using a manually entered experiment hold signal. The experiment hold signal was used in cases such as when changing a battery or realigning the cameras was required.

2.6 Qualitative Participant Questionnaires

Upon task completion, navigational success was recorded and participants were asked a series of questions in the form of a questionnaire providing qualitative feedback. The survey consisted of questions that were 4D-fluoroscopy specific and related to both 4D-fluoroscopy and conventional 2D fluoroscopy. The questionnaire

Figure 6.9: Manual classification of unclassified images resulting from the automatic classification approach.

was designed to determine the benefit of 4D fluoroscopy and endoscopy modes and the conventional 2D modes already provided on existing equipment. The questionnaire was also designed to determine how various factors impacted the participants' ability to perform the task. One question was designed to determine if the vascular network provided the phantom posed a challenge to the task at hand. Another question was to determine to what degree the catheters influenced the ability of the participant to perform the task. Also of interest was determining if the task depended on the viewing angle and non-overlapping views of the vasculature. An overall question was geared at the overall task difficulty provided all factors involved. When using the 4D displays, various other items were of interest to determine the perceived utility of 4D-fluoroscopy with 4D-endoscopy, including the following: To what degree were the conventional 2D displays utilized? Which, if any, 4D display, fluoroscopic or endoscopic, was used? To what degree was the external (virtual fluoroscopic) view used? To what degree was the endoscopic (virtual endoscopy) view used? Under what conditions were 4D displays of any type chosen over the conventional 2D displays? Also of interest were the answers to questions relating to the types of procedures the interventionalist performed and if 4D-fluoroscopy would be useful in these procedures if provided. Also, the participants were asked if there were any applications or imaging tasks where the 4D fluoroscopy technique could be beneficial. There was a question ranking the utility of the various provided features of the 4D-endoscopy display, such as coloring of the vessel surface and device, path highlighting, vessel centerline, manual camera movement option, the ability to pause the camera, and the ability to show/hide the 3D vessel surface. A question targeted the ranking of the provided features of the 4D-fluoroscopy display, including the display of the vessel, the device color, the ability to rotate each view (two provided) for an optional angle, and the ability to zoom in and

out.

The questionnaires used a Likert scale with symmetry and balance on a one (1) to five (5) scale free of forced-choice questions. It has been recommended by Jamieson[75] not to employ mean and standard deviation on ordinal data but rather to utilize the median or mode as the measure of central tendency.

While four (4) questions were fill-in-the-blank and one was of type check-all-that-apply (CATA), the remaining questions used a Likert scale. Data from the questionnaire was entered into MATLAB and processed automatically to generate results tables and graphs, as shown in the results section. The survey can be found in Appendix D.

2.7 Real-time Navigational Task Evaluation

The goal was to perform two participant evaluations during two separate experiment segments on separate days. In the first segment, the participants used 2D-DSA with 4D Fluoroscopy and 4D Endoscopy (4D-assisted) to navigate a complex phantom. The second segment, on the following day, asked the participant to utilize only the conventional 2D-DSA (2D-only) device navigation approach on the same phantom. This approach provided a baseline comparison using only conventional 2D in one segment to be compared and contrasted to the dataset gathered in the 4D-assisted experiment segment. During the 2D-only experiment segment, the participant was allowed to move, rotate, and pan the gantry or couch, as is typical in a conventional 2D-DSA procedure. During the 4D-assisted segment, the participant could not move the gantry and could not lean on or move the couch as it would affect the calibration.

The suggested device configuration was reviewed with the participant (see figure 6.2) as part of the training. A 3D reconstructed view of the phantom was shown and provided to the participant in the form of a 3D-DSA acquisition. Participant training contained a description of the system, features that could be used during the experiment, and a labeled diagram of the phantom, including start and end locations. The participant was allowed to refer back to the written briefing and ask questions for clarification at any time during the experiment.

The layout and features of the user interface, as shown in figure 5.5 were described and demonstrated to the participant. The participant was allowed to utilize contrast injection, contrast agent, and syringes. These were made ready and available. The participant was instructed on the operation of the pump when performing contrast injections or flushes. The participant briefing is in Appendix C.

The x-ray angiography machine provides various fluoroscopy modes with varying degrees of image filtering and smoothing operations. The first participant experienced both options, including RM GLUE mode

and RM FLUORO mode. Upon activation of RM GLUE mode, the user stated a disorientating effect. The participant further stated that when a movement was made and stopped, a pause of approximately a second was required to allow the device to catch up before any subsequent movement. Having been exposed to both options, the participant selected the RM FLUORO mode due to its responsiveness. The rest of the experiment used this mode throughout and across all participants. Although the manufacturer of the vendor-supplied hardware could not provide delay/latency figures, there were no complaints by participants regarding the system's responsiveness when operating in this mode.

The participant completed five (5) navigational tasks with a catheter/guidewire system consisting of a Striker Transcend guide wire with a shapeable tip 0.018" x 165cm, a Boston Scientific Fastracker-325 microcatheter 135cm/12cm, and a Medtronic SiteSeer 5F Angiographic Catheter 100cm configured as shown in figure 6.2. Each navigational task consisted of the navigation of the guidewire tip from the base of the phantom to one of the five (5) endpoints of the vasculature tree as labeled A-E in figure 6.10c. Operators could delineate vascular anatomy during a task as needed by injecting an iodinated contrast agent, generate conventional 2D roadmaps, or both. During the conventional 2D fluoroscopy tasks, the operator could use single or biplane fluoroscopy and select any needed viewing angles. Imaging for both experiment segments occurred at 15 frames per second (fps).

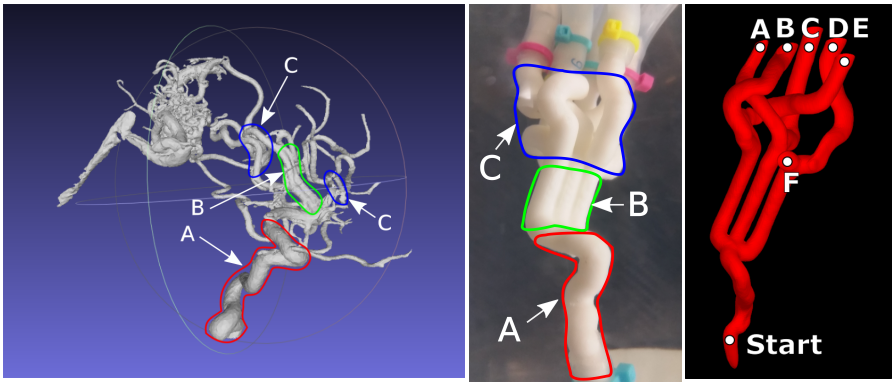

(a) (b) (c)

Figure 6.10: a) Case 679 is an AVM rendered in MeshLAB with carotid, parallel, and tortuous segments. The carotid segment is red, the parallel section is green, and examples of tortuous segments are blue. b) The 3D-printed phantom as mounted in the water-filled cylinder. Labels highlight the A) carotid section, B) three parallel sections, and C) tortuous section. c) The phantom as rendered in the endoscopic view with labeled paths (added to the image) from the start location to the five (5) endpoints A-E.

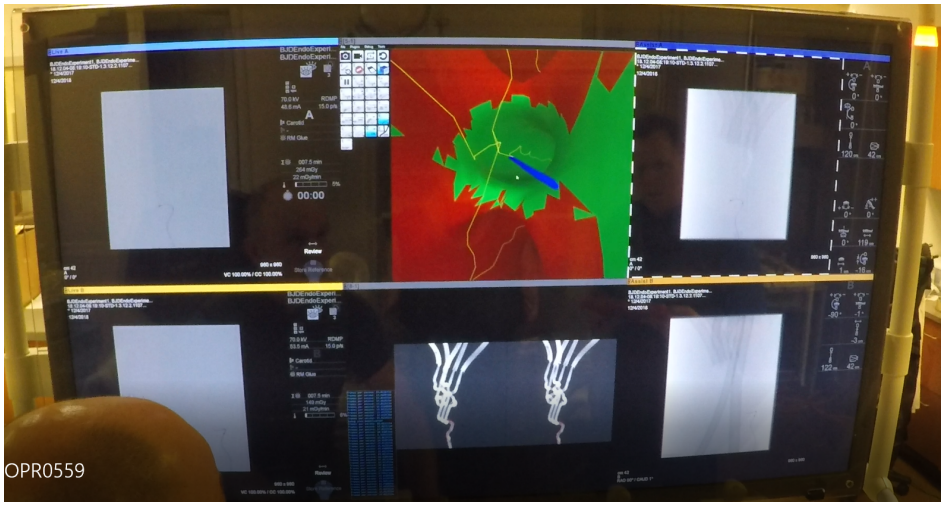

Figure 6.11: Video capture of the C-Arm angiography x-ray system demonstrating integrated real time 4D-assisted during a navigational task performed by a participant. Conventional biplane fluoroscopy A plane (top) and B plane (bottom) images top and bottom left. The top center display demonstrates the 4D endoscopic display while the bottom center display demonstrates the 4D external view, both generated from live biplane fluoroscopy images at 15 fps. The guide wire is rendered blue in the endoscopic display and red in the external view display. The unsubtracted A plane (top) and B plane (bottom) are shown right. The display demonstrates various view types, allowing a view of the static 3D-DSA.

3. Results

The prototype system 4D displays rendered and displayed device movement at the 15 frames per second imaging rate of the fluoroscopic system with no dropped frames as shown in figure 6.11. Two interventional radiologists and one medical student participated in the initial evaluation study. In total, participants completed 15 of 15 navigational challenges in the 4D-assisted segment. During the conventional 2D segment, the completion rate was similar, with 13 of 15 challenges completed with two failures due to device (guidewire) mechanical fatigue, resulting in two paths not traversed by one participant. The results detailed below are grouped into two categories: 1) quantitative results derived from the semi-automated video analysis of the participant's interaction with the system and 2) qualitative results as obtained from the user surveys.

3.1 Quantitative Results

Results of metrics of task time, number of injections, number of pedal presses, imaging time, and total kerma on a per task basis for each segment are shown graphically in figure 6.12. Results indicate similar ranges for task completion times for both experimental segments (4D-assisted and 2D-only). The number of injections indicates the number of contrast injections using a 5 ml syringe with 300 mg/ml Iohexol contrast agent

mixed 50/50 with water with the full syringe push during a single navigational challenge (task). During the 4D-assisted segment, the average number of injections was 0.1 when aggregated, as two operators did not perform any contrast injections, with the remaining operator performing only one contrast injection during one task. Comparing the conventional 2D-only segment, the number of injections was 1.3 per task, ranging from zero to 7. This difference results from the 4D-assisted mode use of the 3D vascular roadmap, generated at the study's beginning, where no additional contrast injections are required. As measured at the central region, the air kerma from both planes averaged 55% higher during the 4D-assisted segment. There was a modest 15% on average increase in the total imaging time per task. This increase in imaging time for the 4D-assisted segment can be accounted for by the fact that 4D-assisted requires both planes simultaneously, while participants were allowed to use one or both planes based on preference. Optimization of radiation dose was beyond the scope of this preliminary study.

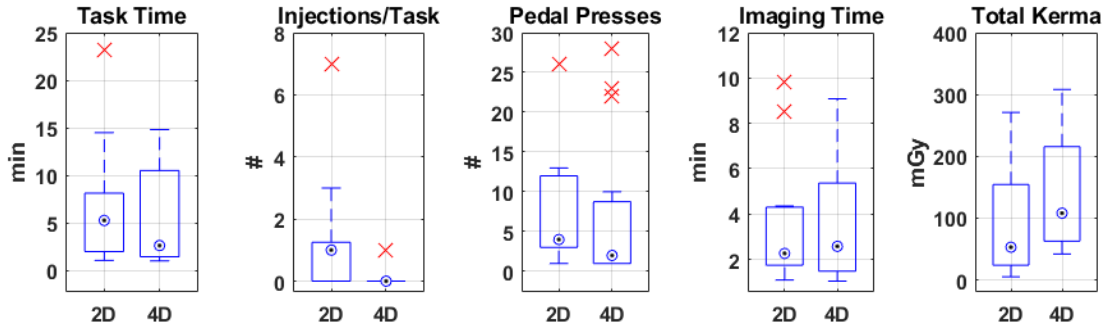

Figure 6.12: Quantitative metrics compare the experimental segment 4D-assisted to the conventional 2D-only experimental segment on a per-task basis. Results are aggregated across all participants and tasks for each experiment segment.

3.2 Qualitative Results

Segments involving 4D-assisted operators reported using the 4D display modes 'often' or 'almost always' on the Likert scale with a median score of 5 with a range of 4 to 5 and reported using the conventional 2D displays 'never' to 'sometimes' with a median score of 2 and a range of 1 to 3 thus indicating a preference for the 4D display. Participants, when asked to what degree they used each display, indicated a preference for the virtual endoscopic viewpoint (median score of 4, range of 4 to 5) over the external viewpoint (median score of 3 and range 2 to 4). Results were aggregated over all paths, and all participants for each of the two segments provided an N equal to fifteen (15) and thirteen (13), respectively. These responses relating to using the 4D-assisted displays are summarized graphically in figure 6.13. The figure graphically represents the response by the participant with the median value represented by the blue circle; the boxes enclose the 25 to 75 percentile range; the whiskers indicate the value range without outliers, and the red "X" symbol

indicates outliers. MATLAB was used to generate the box plots, and the reporting and usage are identical throughout, regardless of the data presented.

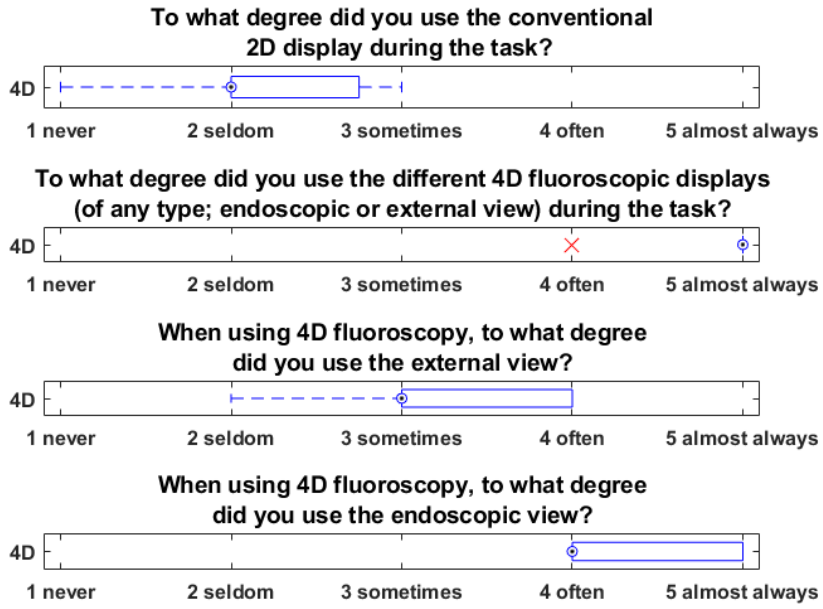

Figure 6.13: Participant responses to questions comparing utilization of 4D-Fluoroscopic displays, both endoscopic and external, as compared to conventional 2D displays.

The perceived utility of 4D fluoroscopy is highly dependent on imaging, providing needed views, and devices used. The questionnaire captured this feedback from the participants. These questions relating to the ability of the participant to complete the task include what effects the vasculature had on performing the task, what degree the style of catheter devices affected the ability to complete the task, and, significantly, if the ability to obtain the appropriate view angle or nonoverlapping views of the vasculature affected the ability to complete the task. The results of these questions are shown graphically in figure 6.14. Overall, participants reported the task ranged from 'very simple' to 'very difficult' on a range of 1 to 5, with the 25-75 percentile responses being 'simple' to 'challenging' falling on the range 2 to 3 when asked if the task was simple or difficult to perform. When asked to what degree the shape of the vasculature influenced the ability to perform the task, answers ranged from 'slightly' to 'extremely' with scores 2 to 5 and the 27-75 percentile responses falling in the range of 'moderately' to 'considerably' with scores from 3 to 4. When asked if the ability to perform the task depended on obtaining appropriate viewing angles or nonoverlapping views of the vasculature, the responses were 'considerably' with a score of 4, with two outliers at 'moderately' and 'extremely' with scores of 3 and 5. Responses to the question as to whether the style of catheter devices influenced their ability

to perform a task responded 'slightly' with a score of 2, with the 25-75 percentile ranges of 'slightly' to 'moderately' with scores in the range 2 to 3.

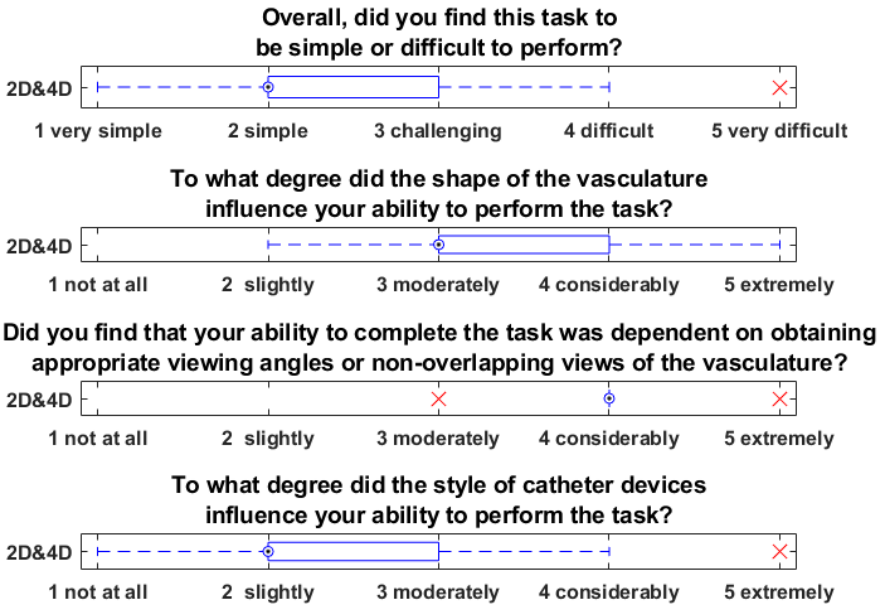

Figure 6.14: Responses aimed to determine factors influencing the ability of the participant to complete a task. The results were aggregated across all segments, participants, and tasks.

These questions were designed to separate the influence of the vascular network's complexity, the catheter's style, and the ability to obtain a desired viewing angle. The final question aimed to determine what impact the catheter used had on the task regardless of the various facts of the vascular structure and ability to achieve the desired viewing angle. Survey data was aggregated over the users for 2D-only and 4D-assisted segments of the experiment, with results shown in figure 6.15. figure 6.15 shows the separation of the results into 4D-assisted and conventional 2D-only results. Results from the question on *overall task difficulty* in figures 6.15 and 6.14 indicate the phantom was complex enough to provide a challenge.

Participant responses to the *impact of the shape of vasculature influence on the ability to perform the task* for 4D-assisted in figure 6.15 shows a larger percentile range for 4D-assisted than for 2D-only. This question was designed to determine how the catheter device affected the navigation tasks. In reviewing participant results, 4D-assisted was slightly more challenging than 2D-only. This finding reflects that 4D is a new and different approach than 2D-only and requires a learning curve. Two additional displays are provided in 4D-assisted with up to five, including endoscopic display, external 4D view, plane A, plane B, and the static 3D-DSA.

Responses to the question regarding *ability to complete the task was dependent on obtaining appropriate viewing angles or non-overlapping views of the vasculature* . They were found to be similar when comparing 4D-assisted and 2D-only segments, as it is not surprising that the ability to obtain the correct view angle is vital regardless of which approach is used. This was a key finding as it shows that 4D-assisted can provide the necessary view angles as two participants performed no 2D roadmap contrast injection. The remaining participant only performed one (1) contrast injection during the 4D-assisted segment of the experiment. When asked what degree the style of catheter devices influenced the ability to perform the task, they were similar at 'slightly'; however, 4D-assisted had a larger percentile range from 'slightly' to 'considerably' on a range 2 to 4 with outliers spanning the range.

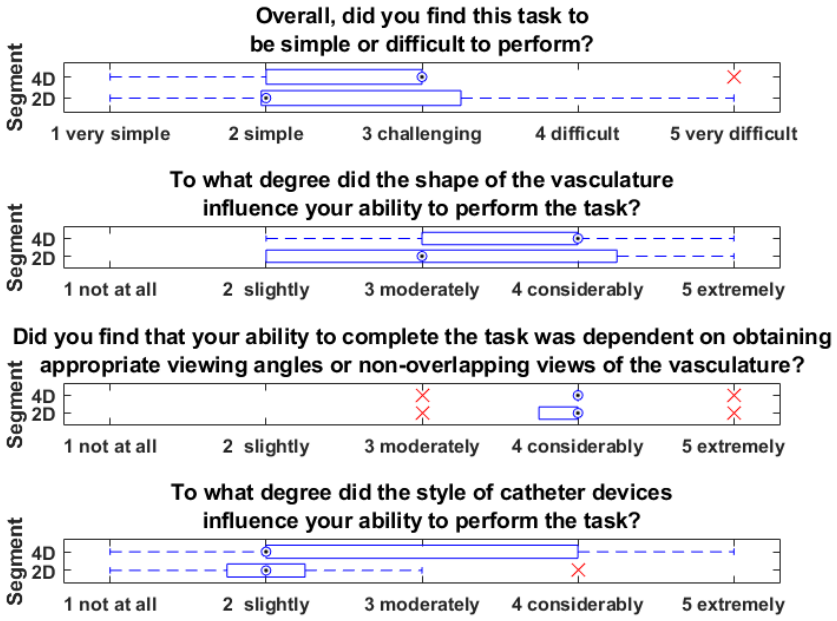

Figure 6.15: Aggregated participant path evaluations vs experiment segment.

Multipart questions were asked relating to the view provided and features of the endoscopic display and external view of virtual 4D-fluoroscopy with results shown in figures 6.16 and 6.17. Due to the structure of multipart questions relating to the endoscopic and fluoroscopic views in the 4D-assisted section of the questionnaire, resulting in a low N, the results were aggregated across all paths. Therefore, the following subjective conclusions were drawn. The results of multipart questions asked to determine what features of the 4D endoscopy display the participants found most useful are shown in figure 6.16. The display of the vessel surface (red), the display of the device (blue), and the path to the target (green) were found by participants to be from 'very useful' to 'extremely useful.' The display of the vessel centerline (yellow) was

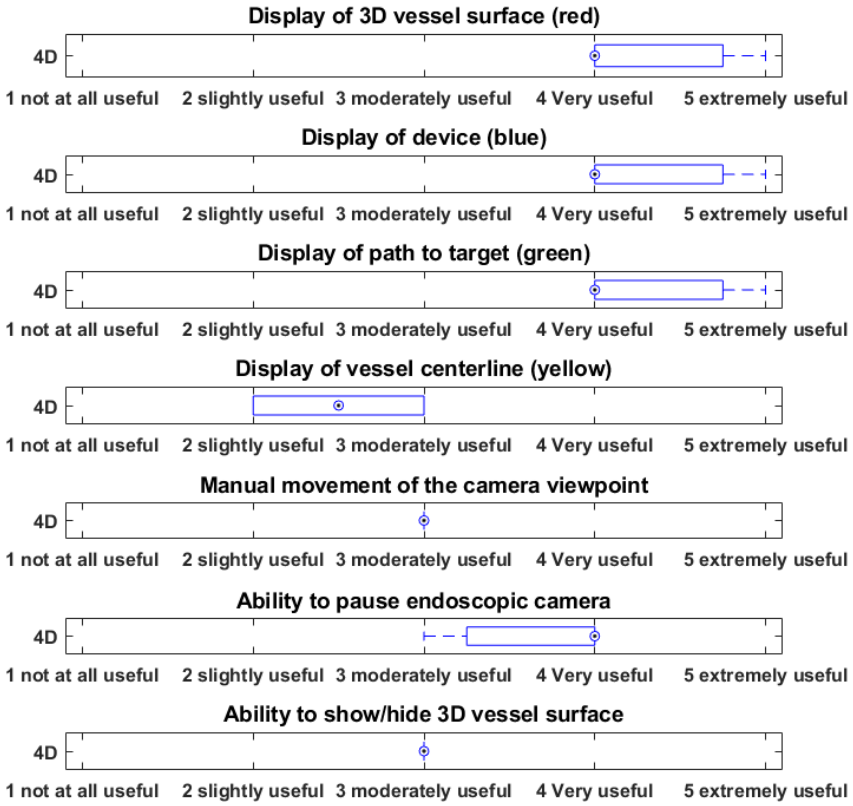

Figure 6.16: Results relating to the 4D fluoroscopy with endoscopic display during the 4D-assisted section of the experiment questionnaire.

'slightly useful' to 'moderately useful.' The ability to pause the endoscopic camera was 'moderately' to 'very useful.' Both the manual moment of the camera viewpoint and the ability to show/hide the 3D vessel surface were moderately useful.

Results of the multipart question asked to determine the utility of the features of the 4D-luoroscopic external display shown in figure 6.17. The participants indicated that the 4D-fluoroscopy display of the 3D *vessel (white)*, the display of the *vessel (red)*, and the *ability to rotate each view for optimal viewing angle* were found to be from 'very useful' to 'extremely useful.' The *ability to zoom* the two views in and out was found to be 'moderately' to 'very useful' and may indicate that the zoom and size of the vasculature presented to the user were adequate.

Results for participants' responses when asked if they preferred 4D-assisted vs conventional 2D-only are shown in figure 6.18. From these results, the following conclusions were drawn. When asked to choose a preference when *viewing parts of the vasculature* respondents agreed 47% of the time that the 4D-fluoroscopy

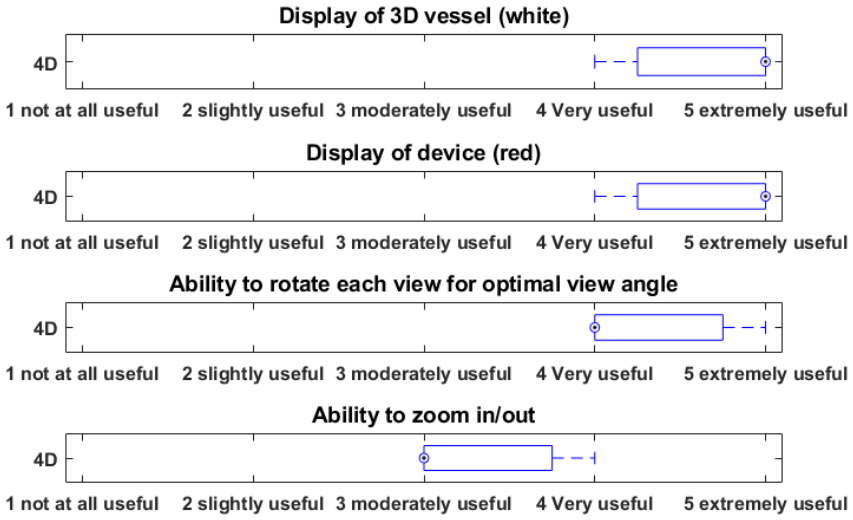

Figure 6.17: Results relating to the 4D fluoroscopic external view display during the 4D-assisted section of the experiment questionnaire.

display is more useful for viewing the vasculature than the 2D display. This result indicates that the participant is not using the display for the anatomic shape. Instead, they use it to view the device in real time and for navigation. All participants agreed 100% when asked in *viewing the path to the target* indicates endoscopy is a feature to aid in viewing the path and thus navigating to the target. In accessing the results of participants' preferences when *viewing the device in relation to the vasculature*, all participants agreed 100% that the 4D fluoroscopy display is useful in determining the device to vasculature relationship. More importantly, it indicates the 4D road mapping in the 4D-fluoroscopy display (bottom red/white) in figure 5.5 is also useful. It is also important to state that two participants did not inject contrast to generate roadmaps in the native 2D but relied on the 4D roadmaps in the 4D-fluoroscopy display. Responses to participant preference in *viewing the device in real time* indicate participants agreed 66% of the time viewing the device in real time was preferentially viewed in the 4D display over the 2D display. This indicates that viewing the device in 4D may not be as important as viewing the path to the target in 4D. However, the realtime device location information is critical in locating where the participant is along the path. The structure of the vasculature (47%) or the orientation of the device within the vasculature (66%) seems less critical importance to the user than viewing the path to the target (100%) and the orientation of the device relative to the vasculature (100%). This also indicates that the endoscopic view path planning rendering of the exact structure of the vasculature is less critical so long as a clear path (green) to the destination is provided by the path planning in the endoscopic view.

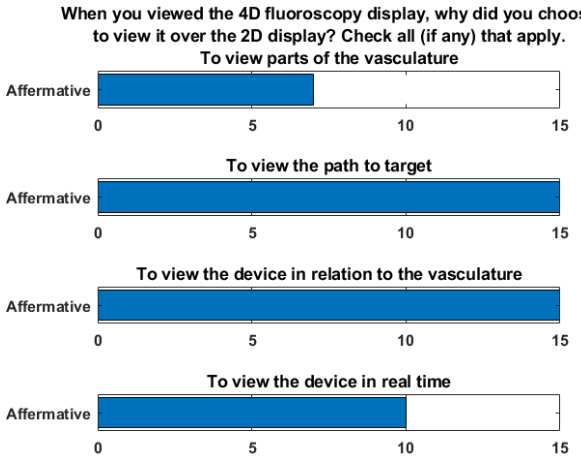

Figure 6.18: 4D-fluoroscopy display utilization vs conventional 2D display results

4. Discussion

Interventional procedures require the navigation of catheters, guidewires, and other devices through complex three-dimensional vascular anatomy. The state-of-the-art gold standard system for such navigations in real time is the x-ray angiography bi-plane system. This system, while useful, provides only two (2) single 2D x-ray projections and a static 3D volume to the operator. No 4D real-time navigation system exists to date, either being used in the field or being researched for potential use for the navigation of devices through the complex 3D vasculature other than what is proposed here. The current 2D with the static 3D system requires the operator to select the required projection angles, up to two, with additional contrast and radiation dose to acquire the view. The operator must mentally integrate the disparate information from the live two 2D and static 3D views to derive a mental image to navigate the device through the complex vasculature network.

4D-fluoroscopy with the endoscopic view and external 3D view aims to address these issues by fusing the 2D views and static 3D volume into an actual virtual 4D display capable of rendering the device and vasculature in three dimensions in real time. The system reported here implements a fully integrated system with some features that are similar to those that have been reported on individually. Epipolar reconstruction efforts, as an example, have been demonstrated and reported with electrophysiology catheters using two views of the device [76, 77]. The concept of virtual endoscopy has previously been reported for 3D visualizations of the heart, bronchial tree, and colon[53, 78, 79]. The user evaluation of the system described here is the first of its kind technology that fully integrates real-time bi-plane 3D reconstructions of guide wires on a frame-by-frame basis up to 15 fps, providing intraluminal endoscopic views of the vasculature and external

4D fluoroscopy to support neurointerventional radiology procedures performed on the gold standard x-ray angiography suite.

Participants were asked to evaluate the system with a wide range of interventional radiology experience and background. These participants were asked to perform a series of navigational tasks in a vascular phantom modeled after features found in a patient-specific AVM case. The experiment was divided into two segments. Participants navigated using the 4D-assisted platform during the first segment, which provided conventional 2D bi-plane views and two 4D displays. The participants were asked to perform the same navigations during the second segment. However, only the 2D conventional displays (2D-only) were provided. Participants reported a wide range of difficulty when performing navigational tasks when asked via the survey and, importantly, that the ability to complete the task was highly dependent on obtaining appropriate viewing angles and or non-overlapping views of the vasculature. This is not a surprising finding. However, it helps to highlight the important distinctions that can be made between the 2D-only and 4D-assisted display modes. It emphasizes the importance of the views provided and means that it can provide increasingly better views of the task that could aid the interventional radiologist. The task success rates for 2D-only and 4D-assisted were similar, indicating that 4D-assisted does not hinder the operator's ability to complete the task. Operators also indicated a preference for the 4D displays over the conventional 2D displays when they were provided during the 4D-assisted segment of the experiment. During the 4D-assisted segment, participants preferred the virtual endoscopic display over the external 3D viewpoint display. These results indicate that 4D virtual endoscopic display could provide value-added utility when used in conjunction with conventional fluoroscopy, emphasizing the capabilities of 4D-assisted to assist in challenging navigational tasks with overlapping vasculature and branching structures. This indicates that the design goals of 4D-fluoroscopy were accomplished for this initial stage of the development.

There are, however, several limitations that must be addressed. The study was limited in the number of participants, two being interventional radiologists and a medical student. Each participant performed five navigational tasks for each of the two experimental segments (4D-asssited and 2D-only), with a few tasks being unable to be completed due to navigational device fatigue. While the current effort was sufficient to evaluate the potential and gain valuable insight into how future testing should be performed, it is clear that a more extensive study should be performed to confirm the findings of this study. Operators reported that the ability to complete the task was somewhat to moderately influenced by the device's performance. The fact that two navigations were not completed due to device fatigue should not be attributed to a failure of the displays, whether it be 2D-only or 4D-assisted. The issue of device fatigue does occur clinically; therefore, it cannot necessarily be attributed to the phantom design. The two tasks where device fatigue

occurred were omitted from the results since device fatigue can impact performance for reasons unrelated to the display method. It should also be noted that the 2D-only experiments were performed after the 4D-assisted for every participant. While there was at least a 24-hour minimum time between segments, there exists the possibility the participant was influenced by the memory of the prior 2D-only navigational task segment. This is to say that it is possible that the participant "learned" the phantom. If it did indeed occur, participant memory of the phantom could be accounted for in the future by randomizing the order of the segments over many participants. When comparing the 2D view to the 4D endoscopic view during the 4D-assisted experiment segment, the 4D endoscopic view was ultimately preferred over the 2D views by participants. Dose optimization would also be critical to any continued future study, as this study did not attempt this. Additionally, no attempts were made to investigate the effects of vascular deformation by the device and/or any roadmap misregistration that would occur as a result. Vasculature deformation is a very real possibility and does occur in patient navigation. At least one participant has stated that the 3D roadmap should not auto-deform in the live view to provide a similar view as the existing conventional 2D roadmaps, as it aids the operator in determining to what degree the device is deforming the vasculature. Future navigational challenge studies should likely include animal models in place of the existing phantom for both the experiment's 4D-assisted and conventional 2D-only imaging segments while attempting to maintain similar dose rates between segments and operators.

5. Summary

This chapter discussed the performance of the current implementation of 4D-fluoroscopy with the virtual endoscopic display. The system was evaluated by asking a set of participants to use the system to perform a set of navigational tasks in a vascular phantom. The phantom contained key patient-specific features. These key phantom features included carotid, parallel, and tortuous segments. Both trifurcations and bifurcations were provided to the participant. The participants were asked to evaluate the 4D-fluoroscopy and endoscopy software both as a unit and separately. Feedback was also gathered by two means, including using a survey based on a Likert scale and through the manual and automatic generation of timeline events of the participant's use of the x-ray angiography system. The phantom was found to be sufficiently complex to provide a near real world experience. Device fatigue issues were encountered when performing a few of the navigations. Operators reported using the 4D display modes more than the conventional 2D displays and preferred virtual endoscopic display over the external view during the 4D-assisted experiment section. Results indicate the justification for a larger-scale study to be performed to further characterize the potential

benefits of 4D-fluoroscopy with the virtual endoscopic display.

7 Conclusions and Future Work

1. 4D-DSA

Modern interventional radiology procedures rely primarily on 2D x-ray imaging and 3D-DSA to visualize vascular anatomy. The goal of 4D-DSA is to augment and enhance the tools available for vascular visualization and specifically to provide the radiologist with time-resolved 3D images of patterns of vascular enhancement. This is achieved by applying a novel reconstruction method to a conventional two-rotation 3D-DSA scan, producing a unique image volume for each time point and projection angle. The design and implementation of a 4D-DSA algorithm requires careful attention to time and storage requirements. For 4D-DSA to be useful in the clinical interventional setting, reconstruction times must be short enough to allow for intraprocedural image review. Given that 3D-DSA reconstruction times are ~15 seconds, and each 4D-DSA scan has >100 time points, a naive implementation would require >25 minutes of reconstruction. Likewise, a naive implementation would increase data storage requirements by >100x. This work presents an implementation of 4D-DSA with GPU acceleration and a sparse back projector, significantly reducing reconstruction time and storage requirements as needed for practical clinical use. In a set of tests with clinical data, the total reconstruction time for 4D-DSA averaged 27 seconds. This total included the initial 12 seconds required to reconstruct a 3D-DSA, which is the starting point for additional 4D-DSA reconstruction steps. Therefore, 4D-DSA with hundreds of time points required only 15 seconds of additional time on average, which is a small increment relative to most interventional procedure steps. Compared to a naive implementation, the sparse backprojector and GPU implementation increased reconstruction speed by >55x (approx. 25 minutes x 60 seconds / 27 seconds). The use of a sparse data representation model also significantly lowered storage requirements. Total storage depends on the threshold used when creating a 3D constraining volume. When a typical threshold yielding a sparsity factor of 98.800 was used, the average size of the 4D-DSA data set was 85.5 megabytes (MB). To put this into perspective, this allows 11 cases to be saved to a small 1 GB USB stick. Given a 4TB hard drive, approximately 49,056 cases could be saved. The spatial resolution of 4D-DSA relative to 3D-DSA was evaluated in silico and experimentally. 4D-DSA was

shown to be capable of providing a resolution of 1.67 cycles/mm at a temporal resolution of 30 frames per second using a standard protocol. It was demonstrated that so long as the blurring kernel and the threshold are kept within acceptable ranges, the resolution of the 4D-DSA can retain the resolution of the underlying 3D-DSA. Deviations between 4D-DSA and 3D-DSA resolution were found only when excessive thresholding was used in constraining volume generation.

Overall, the 4D-DSA studies presented here demonstrated 1) 4D-DSA reconstruction can be performed in under 30 seconds for a wide range of scenarios and is suitable for intra-procedural tasks and 2) the implementation manages memory and disk space in a way that is efficient and comparable with commercial hardware. The key technique that made this possible was the use of a sparse backprojector, a sparse data storage model, and GPU acceleration.

2. 4D-Fluoroscopy and 4D-Endoscopy

Conventionally, catheter devices are visualized during an interventional procedure using real-time 2D x-ray projection imaging (fluoroscopy). Although navigation of a device through patient anatomy is a real-time 3D task, there are currently no commercial x-ray imaging approaches that provide real-time 3D imaging. The technique of 4D-fluoroscopy was developed specifically to address this problem. 4D-fluoroscopy uses the two simultaneous views available from a bi-plane x-ray angiography system to produce a real-time frame-by-frame reconstruction of the catheter device in 3D. The device reconstructions are displayed relative to a 3D image of vascular anatomy, e.g., a contrast-enhanced 3D-DSA scan acquired with the same x-ray angiography system. This work expanded the feature set of 4D-fluoroscopy to include 1) a real time virtual endoscopic display in which the device and vascular anatomy are viewed with a virtual camera placed near the tip of the catheter reconstruction, analogous to an actual endoscopic device, and 2) a path planning feature to aid with navigation in endoscopic display mode. The path planning feature was designed so that users could identify waypoints in the 3D vasculature to traverse paths that are more complicated than the simple shortest-path approach. A complete 4D-fluoroscopy system with both external and endoscopic viewpoints was designed around specifications for lag, frame rate, time to ready, types of displays, and type of camera paths. The system was then implemented on a mobile platform (cart) that could be interfaced with an existing biplane x-ray angiography system. The resulting system could display reconstructions at >30 fps, which exceeds conventional 15 fps biplane x-ray fluoroscopy requirements. The utility of 4D-fluoroscopy and the new virtual endoscopic display was evaluated in a study requiring operators to complete catheter navigation tasks in a phantom. A tortuous vessel phantom with trifurcations and bifurcations was

designed and 3D printed for this study. The phantom was designed and modeled after a complex real-world arteriovenous malformation (AVM). Operators were asked to navigate a catheter from the base of the vascular tree to different endpoints using two styles of guidance: 1) conventional 2D-only guidance and 2) 4D-assisted guidance in which the operator was presented with conventional 2D displays as well as 4D displays with both virtual endoscopic and external camera viewpoints. Quantitative metrics such as task time, contrast injections per task, imaging time, and total kerma were gathered from the post-processing of video recording. Qualitative metrics were based on a post-procedure questionnaire. The 4D-fluoroscopy system could display guidewire and catheter manipulations in complex vascular anatomy, with virtual viewpoints not achievable with conventional displays. A key finding of this study was that operators reported using the 4D display modes more than conventional 2D display and, importantly, a preference for virtual endoscopic display over the external camera viewpoint.

3. Future Work

The results of this work suggest several future research directions. During the completion of this work, 4D-DSA has been made commercially available by one system vendor. Despite this commercial availability, characterization of the performance of 4D-DSA remains an active topic. The potential to quantitatively determine blood flow from 4D-DSA images has been explored by Shaughnessy[8], Wu[80], Meram[81], and others. A similar line of research exists with 2D-DSA. For example, Periyasamy[82], Hoffman[83], and Wagner et al.[84] have published on the technique of qDSA, which determines blood velocity from 2D angiograms. While blood velocity (cm/s) can be computed from 2D images, 4D imaging promises blood flow (mL/s) since one can compute both blood velocity and vessel cross-sectional area from a 4D-DSA dataset. A complete characterization of 4D-DSA blood flow quantification accuracy and sensitivity to image artifacts is an open research topic. If proven accurate, quantitative pre- and post-interventional blood flow measurements could one day be used to determine if a procedure is successful.

The GPU used for the 4D-DSA timing analysis was an NVIDIA Quadro 4000 with a GPU clock of 475MHz, 720Mhz memory clock, 2GB of memory, and 8 Streaming Multiprocessors (SM). If a newer GPU were used, such as an NVIDIA GeForce RGX 4090 Max-Q with a GPU clock of 930 MHz, 2250MHz memory clock, 16GB of memory, and 76 Streaming Multiprocessors (SM), the reconstruction performance would be significantly improved. Considering GPU and memory clock frequency alone, an almost 2x (1.96) increase might be obtained. Considering the SM difference alone, an almost 10x (9.5) increase may be possible. The increased memory provides an opportunity to perform view-parallel processing in addition to ray-parallel

processing, although actual performance increases depend on memory bus and texture unit details.

The 4D-fluoroscopy work reported here has demonstrated feasibility and utility in a controlled phantom study. Although this was an important initial step in defining the feature set of 4D-fluoroscopy, this work should be followed by a larger-scale in vivo study that provides more realistic scenarios. There are a potentially large number of clinical procedures that would benefit from real-time 3D visualization. Generally, any procedure involving device navigation in tortuous vascular anatomy (e.g., neurointerventional procedures) or in large 3D spaces that do not confine the catheter device (e.g., cardiac interventional, or percutaneous needle procedures) may benefit. However, the adoption of the present methods to new clinical procedures will require adaptations to device segmentation and reconstruction methods.

A VLSR Analysis in Image or Frequency Space

The volumetric limiting spatial resolution (VLSR) can be determined using two primary methods including the point spread function (PSF) analysis and the edge method. During the investigations into the methods of the point spread function revealed there are two methods to center the data contained in the PSF. The resolution can be determined in either image space or frequency space. Based on research image space analysis seemed more prevalent in the literature and hence was the method used for determining the VLSR of 4D-DSA, the frequency space approach has fewer steps and is simpler when it comes to the radial sampling. The two approaches are outlined graphically below in figures A.1 and A.2.

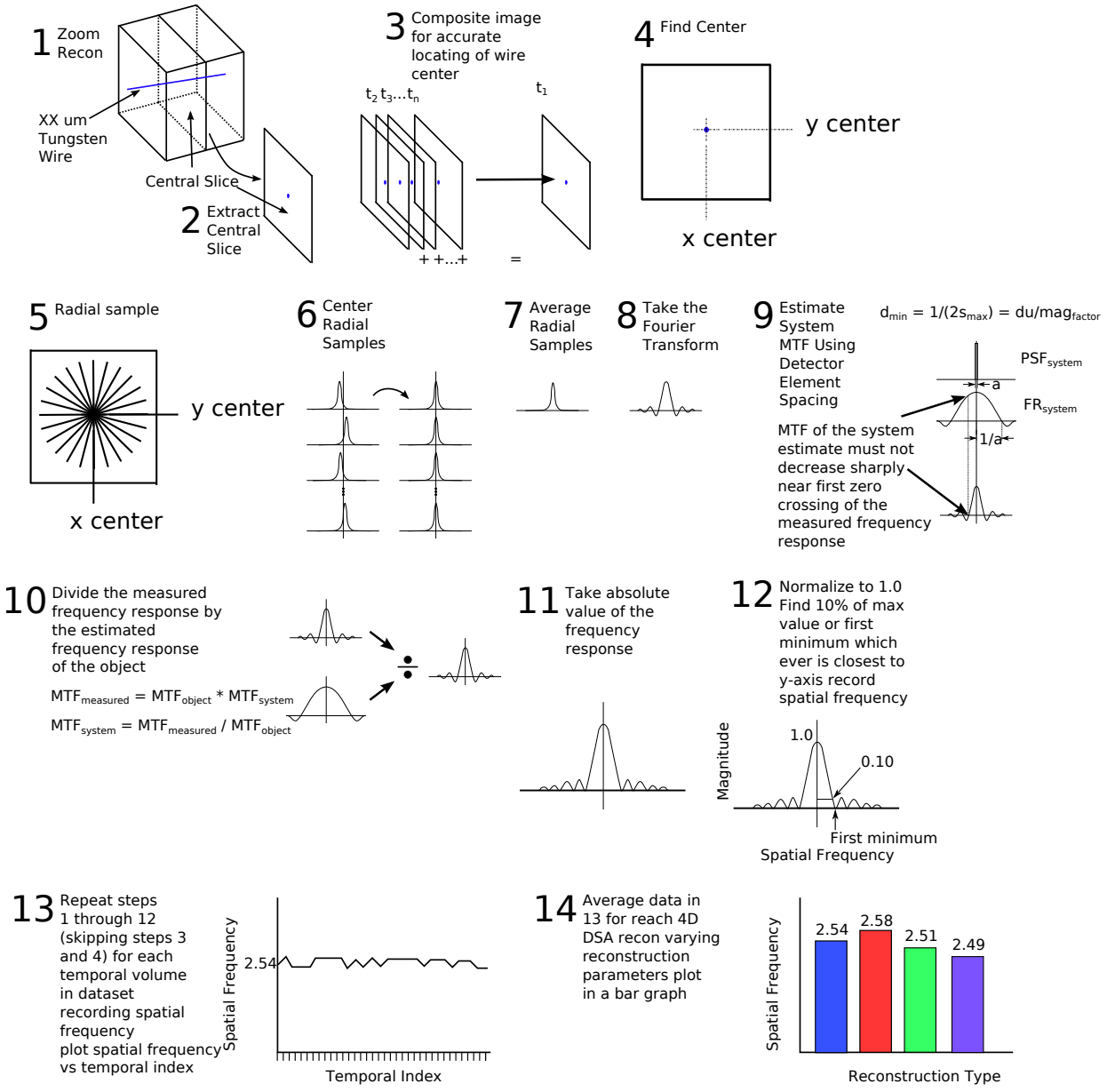

Figure A.1: Graphical representation for a method for determining spatial resolution in image space. The frequency space approach as shown has fewer steps and less prone to error as the frequency space appraoch eliminates the need to center the data before radially sampling. Step 3 in the Frequency space appraoch has the effect of automatically centering the data in frequency space where results depend on Steps 4 through 6 in the image space appraoch where the data must be centered and aligned.

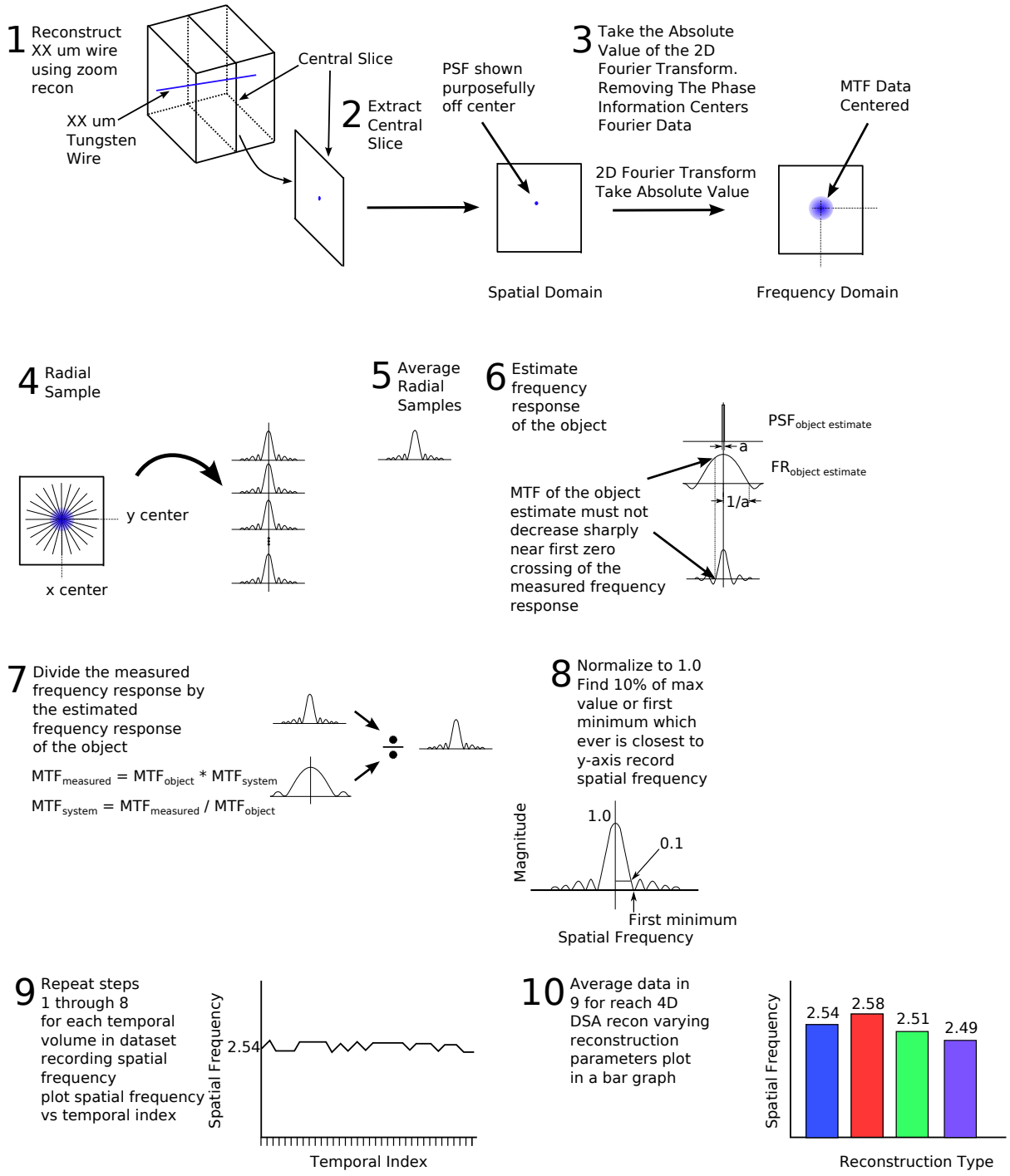

Figure A.2: Graphical representation for a method for determining spatial resolution in frequency space.

B 4D DSA Timing Data

Table B.1: Reconstruction Parameters And Reconstruction Times For Various Cases

Case	Sparse Number of Voxels	Sparsity Factor	4D DSA Sparse Reconstruction	4D DSA Window Level	4DDSA Min_max	GPU Back-projection
1021	5111814	95.00	1292.00	28.00	520.00	10625.00
1021	204476	99.80	201.00	1.00	519.00	10533.00
1021	20450	99.98	163.00	0.00	528.33	10422.00
1021	5113	99.99	173.00	0.00	530.33	9942.00
1022	5111812	95.00	1169.00	28.00	521.67	10344.00
1022	204475	99.80	199.00	1.00	517.33	10448.00
1022	20449	99.98	161.00	0.00	521.33	10588.00
1022	5113	99.99	176.00	0.00	519.67	10617.00
343	5111810	95.00	1200.00	30.00	512.67	9918.00
343	204476	99.80	245.00	1.00	520.00	9607.00
343	20450	99.98	184.00	0.00	508.67	9378.00
343	5114	99.99	136.00	0.00	515.67	10124.00
Carotid Stenosis	5111810	95.00	1121.00	28.00	481.67	10012.00
Carotid Stenosis	204474	99.80	185.00	1.00	491.67	9558.00
Carotid Stenosis	20449	99.98	132.00	0.00	477.00	10184.00

Table B.1: Reconstruction Parameters And Reconstruction Times For Various Cases

Case	Sparse Number of Voxels	Sparsity Factor	4D DSA Sparse Recon-struction	4D DSA Window Level	4DDSA Min_max	GPU Back-projection
Carotid Stenosis	5114	99.99	139.00	0.00	489.67	9654.00
AVM	5111810	95.00	2493.00	31.00	726.00	20166.00
AVM	204474	99.80	433.00	1.00	701.67	20696.00
AVM	20450	99.98	281.00	0.00	713.67	20617.00
AVM	5113	99.99	288.00	0.00	709.67	20754.00
Carotid	5111812	95.00	3143.00	30.00	443.33	15874.00
Carotid	204475	99.80	296.00	1.00	438.00	15739.00
Carotid	20451	99.98	223.00	0.00	441.67	15668.00
Carotid	5114	99.99	208.00	0.00	434.33	15672.00
283-R75671	5111810	95.00	2488.00	30.00	756.67	22076.00
283-R75671	204475	99.80	374.00	1.00	764.67	20868.00
283-R75671	20449	99.98	313.00	0.00	761.67	21997.00
283-R75671	5113	99.99	315.00	0.00	760.00	21528.00
618	5111811	95.00	1516.00	28.00	552.67	13066.00
618	204474	99.80	217.00	1.00	555.67	11997.00
618	20449	99.98	174.00	0.00	545.00	12163.00
618	5113	99.99	175.00	0.00	548.00	12982.00
679-R36224	5111809	95.00	2603.00	27.00	756.67	21783.00
679-R36224	204474	99.80	375.00	1.00	759.33	23152.00
679-R36224	20450	99.98	323.00	0.00	765.00	21831.00
679-R36224	5114	99.99	288.00	0.00	755.00	22993.00
756-R36224	5111810	95.00	2497.00	28.00	757.33	23211.00
756-R36224	204475	99.80	387.00	1.00	761.00	22299.00
756-R36224	20450	99.98	496.00	0.00	757.67	22970.00
756-R36224	5113	99.99	310.00	0.00	753.33	22407.00

Table B.1: Reconstruction Parameters And Reconstruction Times For Various Cases

Case	Sparse Number of Voxels	Sparsity Factor	4D DSA Sparse Reconstruction	4D DSA Window Level	4DDSA Min_max	GPU Back-projection
756-R75894	5111810	95.00	2454.00	28.00	751.00	22406.00
756-R75894	204475	99.80	469.00	1.00	762.00	23014.00
756-R75894	20450	99.98	349.00	0.00	759.67	22542.00
756-R75894	5113	99.99	344.00	0.00	760.67	21812.00

C 4D Fluoroscopy Participant Briefing

What follows is the participant briefing document that was explained and provided for review to the participant during the interactive demonstration.

Protocol:	4D-Endo Participant Briefing	Revision:	2
Number:	Endo-5	Revision Date:	Aug 27, 2018
Author(s):	Brian J. Davis	Print Date	June 22, 2021
		Page	1 of 5

4D-Endo Participant Briefing

- 4D-Endo Participant Briefing
    a. Discus the goal of navigating the phantom with both 2D standard fluoro practices and 3D endo by reading the following paragraph(s). The participant shall also be allowed to read and refer back to the statements throughout the experiment at any time the participant need not refer to sections labeled researcher as these sections involve tasks the researcher is to perform or topics to discuss:

Goal

The goal of this experiment has two phases. The first phase is to obtain a base line for device navigation of 2D fluoro of a complex vascular structure with features closely resembling, but not identical to, those that can be found in human subjects. Then 4D-Endo/Fluoro capabilities will be activated and the participant will asked to utilize these features as much as is possible to complete a similar task as was performed during the 2D-Fluro phase while relying on 2D-fluoro as little as is possible.

The Vascular phantom that will be used for the navigation task is shown and labeled in Figure 1. There a total of six (6) paths. Only five (5) of these paths labeled A, B, C, D, and E are navigable due to a manufacturing defect in the phantom. Path F is not navigable past the labeled point. The task will therefore be limited to the possible paths. These five (5) paths will be navigated using two approaches. The one approach will be to use standard 2D-DSA methods and the other approach will be to utilize both 4D Virtual Endoscopic View and 4D Virtual Fluoro View (simply referred to combined as 4D-Fluoro) in conjunction with standard 2D DSA approaches with some restrictions on the 2D DSA methods.

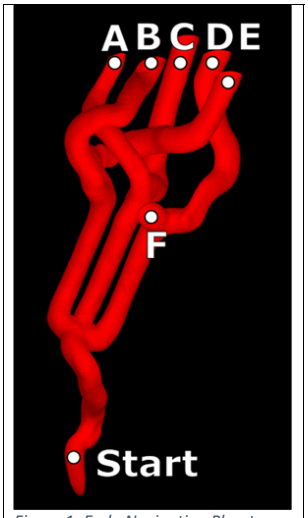

Figure 1: Endo Navigation Phantom with Start location and end paths labeled A-F labeled. Path F is not navagable past the labeld point due to manufacturing defect.

Recording of Data

During this experiment the participant may be asked to record selected 2D Fluoro sequences. This is to say that any time the pedal is pressed and navigation or roadmap is performed the 2D fluoros may be recorded if requested. The experiment will also be recorded using audio and video equipment.

Device type and use.

The device(s) used can be any device or combination and configuration of devices the participant deems is necessary to complete the task. There is a recommendation based on previous use with the phantom

and discussions with medical staff a configuration that has served the purpose well. The configuration consists of the following items:

- Introducer sheath
- (2) Rotatable side arm adapter optionally with thumb depress seal
- Base catheter
- Micro catheter
- Micro wire (device)
- (3) 5ml syringes

The introducer sheath is the only item that must remain fixed due to the cylinder phantom housing design and pluming devices leading up to the phantom. The recommended configuration is shown in Figure 2. It is recommended to depress the syringes to inject water at both locations after any contrast injections to help in lubricating the interface between base catheter and micro catheter and between the micro catheter and the device.

It is also recommended to remove the micro catheter micro wire from the base catheter before performing any contrast puffs for road maps. An alternate to using the base catheter for contrast injections is to utilize the syringe at the catheter sheath inserter located nearest to phantom where the injector is connected, however this requires removal of the base catheter.

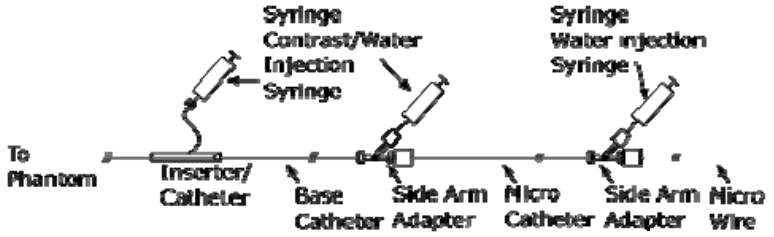

Figure 2: Suggested device configuration

Researcher:

Introduce participant to device configuration and demonstrate:

- Side arm adapter operation. How to hold and operate.
- Discuss stiffness differences from having all devices aligned at their tips
- Discuss navigation using the three devices

2D Fluoro phase

Protocol:	4D-Endo Participant Briefing	Revision:	2
Number:	Endo-5	Revision Date:	Aug 27, 2018
Author(s):	Brian J. Davis	Print Date	June 22, 2021
		Page	3 of 5

2D fluoro is currently the gold standard on bi-plane systems. In this experiment a vascular phantom has been designed and 3D printed which is has similar features to those of complex real anatomy based on actual human scans. During the 2D fluoro phase you the participant will be allowed to use any process or procedure currently used in 2D device navigation including contrast puffs, changing machine C-Arm orientation of either or both A and B planes, and patient table movements. The goal is to navigate the vascular phantom using standard 2D fluoro practices to obtain a base line.

4D-Endo/Fluoro phase

The next phase will entail activating 4D-Endo/Fluoro capabilities using prototype software and hardware. During the 4D-Endo/Fluoro endo phase various capabilities will be made available to you as a participant. The following methods will diverge from standard 2D Fluoro phase above:

- During this phase the C-Arm and patient table positions will remain fixed.
- The participant is asked not to lean on or change position of the patient table.
- The participant may find that contrast injection puffs for the creation of road maps may not be needed during this segment.
- The participant is asked to utilize 4D-Endo and 4D-Fluoro screens as much as is possible the duration of this segment of the experiment. Use of 2D fluoro(s) is allowed when necessary or if they are preferred for any reason by the participant.
- The participant is asked to keep an approximate mental record of the percentages of use of the various modes, 2D Fluoro, 4D-Fluoro, and 4D-Endoscopic View.
- The participant is asked that if a desired view does not seem or obtainable from the prototype 4D-Endo/Fluoro system to then ask the researcher for assistance in obtaining the view with the 4D-Endo/Fluoro prototype software.

Researcher:

Describe and discuss and the prototype software user interface:

The prototype software interface is shown in Figure 1. The software consists of three main software panels. These panels are the buttons, Endoscopic Display (4D Endo), and External 4D Displays (4D Fluoro). The layout can be modified to suit the display so the layout shown is not the same as what will be used during the experiment. The buttons can be hovered over to allow hover over text to appear which describes the button feature. The first four (4) buttons control the external 4D Displays (4D Fluoro) while the remaining buttons with the “E” in the upper right corner are used for controlling the Endoscopic Display (4D Endo).

The Endoscopic Display has two main modes which include a 3D external view mode and the endoscopic “down the pipe view” mode (shown in figure). Endoscopic Display can be used for path planning when in 3D external view. When in endoscopic down the pipe view the device is drawn blue, the vascular red, and optionally can display centerline yellow, and the target location (not shown).

Protocol:	4D-Endo Participant Briefing	Revision:	2
Number:	Endo-5	Revision Date:	Aug 27, 2018
Author(s):	Brian J. Davis	Print Date	June 22, 2021
		Page	4 of 5

The external 4D Displays (4D Fluoro) show a Maximum Intensity Projection (MIP) view of the vasculature shown white/gray and overlay of the device shown red. Both displays shown top and bottom in can be rotated to any view and can be zoomed.

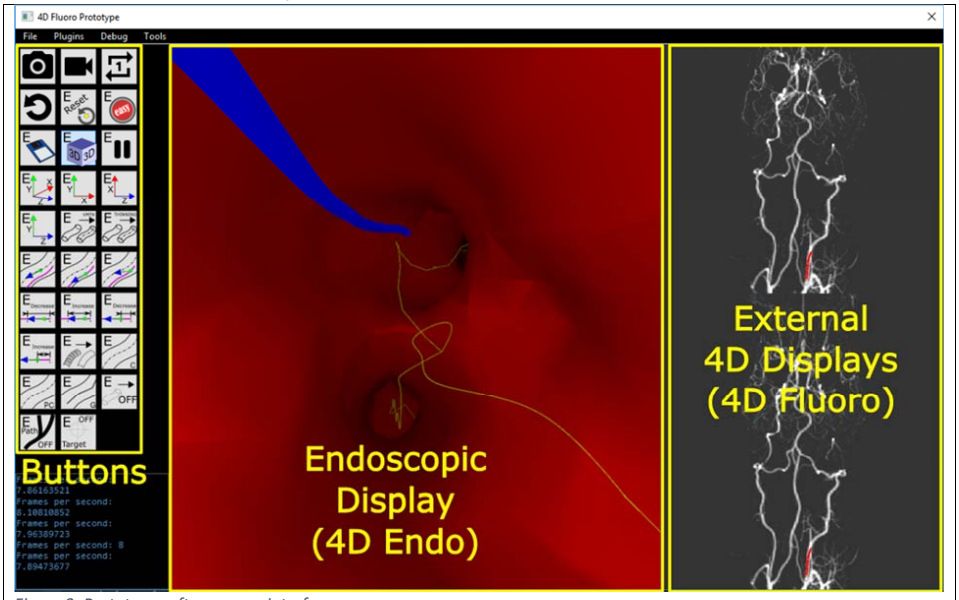

Figure 3: Prototype software user interface.

Introduce participant to 4D Endoscopic View software and demonstrate for the participant and allow them to interact with the system and experience at each step:

- State to participant: "This is not a test of the participant's ability to use the software, rather it is a test of the system, and that at any time the user can ask the researcher to perform any of the actions required to get the desired view in the prototype 4D Fluoro software. However if the participant would like to interact with the software directly this is allowed."
- Demonstrate use of mouse interaction
- Discuss hovering over buttons to see hover over text descriptions appear form buttons.
- Endoscopic View Modes/Features
    - Discuss Endo reset button and how it can be used to "reset the view"
    - Discuss Endo view buttons
    - Demonstrate the use of 3D mode and Endo mode in Endo view.
    - Demonstrate ability to rotate vascular network in both Fluoro and Endo views
    - Demonstrate Target endpoint in path planning

  - Demonstrate the ability to show/hide the target using the button.
  - Discuss the two current methods of operation including
    - Slow motion at bifurcations
    - Fast motion "follow yellow brick road' utilizing Endoscopic View path planning feature.
  - Endoscopic view pause mode
  - Endoscopic view look at modes
    - On centerline look at device
    - On device Look at device
    - On centerline look at centerline
  - Endoscopic view enable/disable centerline
  - Endoscopic view enable disable vessel mesh
  - Path planning – participant will not be expected to perform this action they will only have to ask researcher to plan/select the next path
  - Discuss ability to move the view back from tip of the device or closer to the device tip if desired. Show and demonstrate use of UI buttons.
  - Discuss endo cam look around mode allowing user to rotate camera and look in various directions.
- Discuss temporal averaging of the RM Glue mode and slight delay as a balance between responsiveness and smooth motion video
- Discuss need to limit the device from looping back on itself. State that Virtual Fluoro can handle this situation and the Endoscopic views will yield a view, though it may not be a desirable down range view.
- Demonstrate ability to rotate both (2) External 4D displays (4D Fluoro).
- Demonstrate ability to zoom both (2) External 4D displays (4D Fluoro).
- State to participant (AGAIN): "This is not a test of the participant's ability to use the software, rather it is a test of the system, and that at any time the user can ask the researcher to perform any of the actions required to get the desired view in the prototype 4D Fluoro software. However if the participant would like to interact with the software directly that this is allowed."

Researcher: Lab book

a. Record any questions the participant has about the experiment.
b. Record answers provided to participant.

D 4D Fluoroscopy Participant Survey

Protocol:	Endo Survey	Revision:	4
Number:	Endo-9	Revision Date:	Sept 17, 2018
Author(s):	Brian J. Davis	Print Date	May 7, 2020

Participant ID:_____

Navigational Method (check one): □ 2D only □ 2D and 4D

Complete these questions after performing <u>each task</u>

1. To what degree did the shape of the vasculature influence your ability to perform the task?

Rank / Task	1 not at all	2 slightly	3 moderately	4 considerably	5 extremely	Comment
A						
B						
C						
D						
E						

2. To what degree did the style of catheter devices influence your ability to perform the task?

Rank / Task	1 not at all	2 slightly	3 moderately	4 considerably	5 extremely	Comment
A						
B						
C						
D						
E						

3. Did you find that your ability to complete the task was dependent on obtaining appropriate viewing angles or non-overlapping views of the vasculature?

Rank / Task	1 not at all	2 slightly	3 moderately	4 considerably	5 extremely	Comment
A						
B						
C						
D						
E						

4. Overall, did you find this task to be simple or difficult to perform?

Rank / Task	1 very simple	2 simple	3 challenging	4 difficult	5 very difficult	Comment
A						
B						
C						
D						
E						

Protocol:	Endo Survey	Revision:	4
Number:	Endo-9	Revision Date:	Sept 17, 2018
Author(s):	Brian J. Davis	Print Date	May 7, 2020

Also complete these questions for each task when using the 2D plus 4D display method

5. To what degree did you use the conventional 2D display during the task?

Rank / Task	1 never	2 seldom	3 sometimes	4 often	5 almost always	Comment
A						
B						
C						
D						
E						

6. To what degree did you use the different 4D fluoroscopic displays (of any type; endoscopic or external view) during the task?

Rank / Task	1 never	2 seldom	3 sometimes	4 often	5 almost always	Comment
A						
B						
C						
D						
E						

7. When using 4D fluoroscopy, to what degree did you use the external view?

Rank / Task	1 never	2 seldom	3 sometimes	4 often	5 almost always	Comment
A						
B						
C						
D						
E						

8. When using 4D fluoroscopy, to what degree did you use the endoscopic view?

Rank / Task	1 never	2 seldom	3 sometimes	4 often	5 almost always	Comment
A						
B						
C						
D						
E						

Protocol:	Endo Survey	Revision:	4
Number:	Endo-9	Revision Date:	Sept 17, 2018
Author(s):	Brian J. Davis	Print Date	May 7, 2020

9. When you viewed the 4D fluoroscopy display, why did you choose to view it over the 2D display? Check all (if any) that apply.

Reason / Task	To view parts of the vasculature	To view the path to target	To view the device in relation to the vasculature	To view the device in real time	Other reason (Briefly describe)
A					
B					
C					
D					
E					

Protocol:	Endo Survey	Revision:	4
Number:	Endo-9	Revision Date:	Sept 17, 2018
Author(s):	Brian J. Davis	Print Date	May 7, 2020

Complete these questions after completing the 2D + 4D experiment

1. How many years of clinical interventional experience do you have (fractional years are acceptable)?

_____

2. What types of interventional procedures do you perform, primarily?
   [Body / Neuro / Cardiac / Other / None]

_____

3. If 4D fluoroscopy were developed into a clinical system, would you find it useful in your clinical practice? Are there particular clinical applications or imaging tasks where you would want to use 4D fluoroscopy? If there are applications or tasks which would potentially benefit which features of the 4D fluoroscopy system would you find useful for the purpose?

_____

_____

_____

_____

_____

_____

_____

_____

_____

_____

_____

_____

_____

_____

_____

_____

_____

Protocol:	Endo Survey	Revision:	4
Number:	Endo-9	Revision Date:	Sept 17, 2018
Author(s):	Brian J. Davis	Print Date	May 7, 2020

4. Rank the utility of the following features of the Endoscopic display of 4D fluoroscopy.

Rank / Task	1 not at all useful	2 slightly useful	3 moderately useful	4 Very useful	5 extremely useful	Comment
Display of 3D vessel surface (red)						
Display of device (blue)						
Display of path to target (green)						
Display of vessel centerline (yellow)						
Manual movement of the camera viewpoint						
Ability to pause endoscopic camera						
Ability to show/hide 3D vessel surface						

5. Rank the utility of the following features of the External display of 4D fluoroscopy display.

Rank / Task	1 not at all useful	2 slightly useful	3 moderately useful	4 very useful	5 extremely useful	Comment
Display of 3D vessel (white)						
Display of device (red)						
Ability to rotate each view for optimal view angle						
Ability to zoom in/out						

E Additional Qualitative Results

The aggregation of both 2D and 4D data from figure 6.14 in Chapter 6 is further expanded on a per path basis in figures E.1 and E.2. Due to the low N (3) as the question is aggregated by path only very subjective conclusions could be drawn if any. This data is provided here for completeness of the data reviewed during the research.

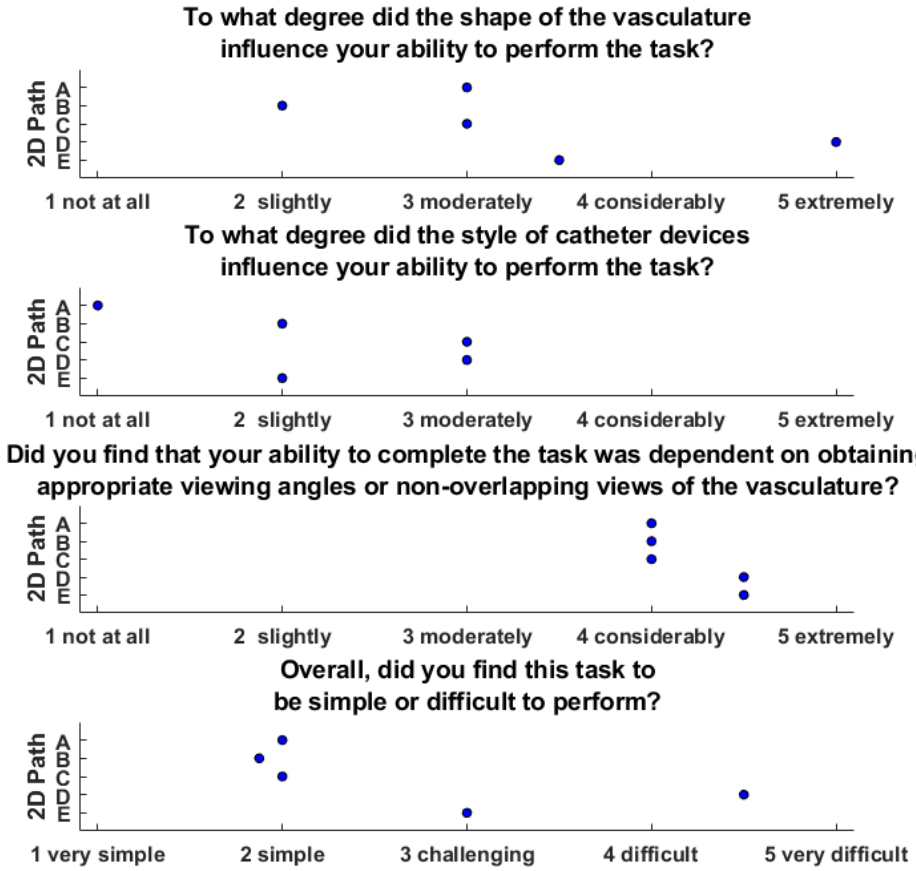

Figure E.1: 2D per path aggregated results

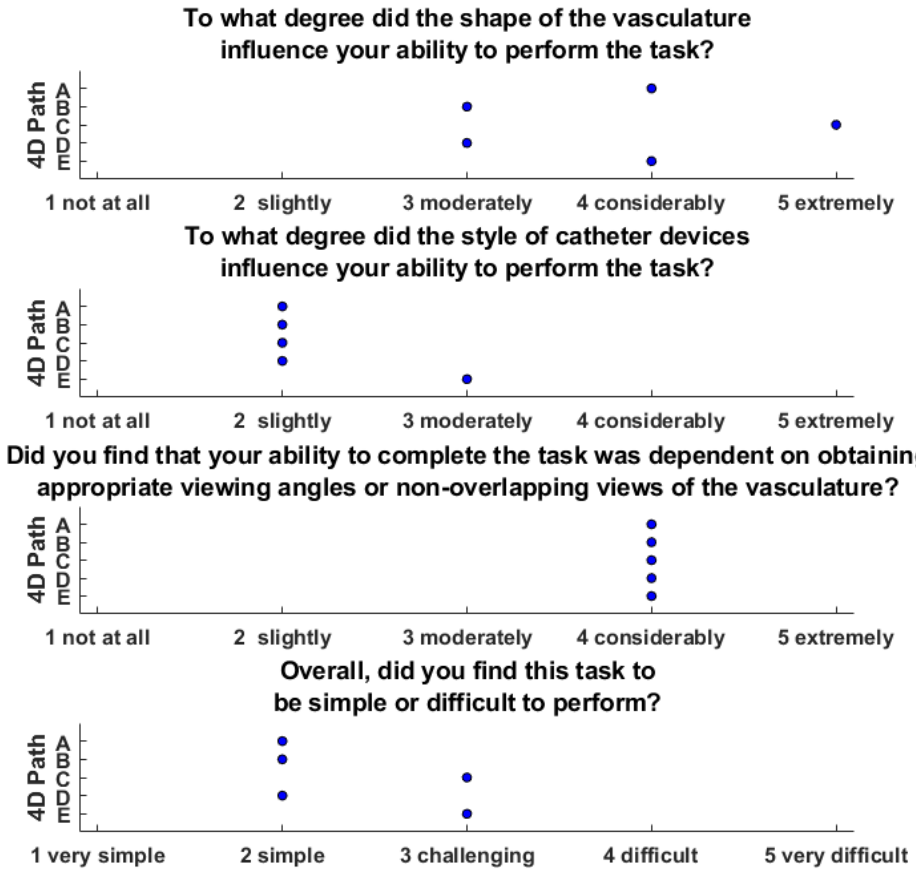

Figure E.2: 4D per path aggregated results

Bibliography

[1] Brian J. Davis, Erick Oberstar, Kevin Royalty, Sebastian Schafer, and Charles Mistretta. Volumetric limiting spatial resolution analysis of four-dimensional digital subtraction angiography. *Journal of Medical Imaging*, 3(1):013503–013503, 2016.

[2] B. Davis, K. Royalty, M. Kowarschik, C. Rohkohl, E. Oberstar, B. Aagaard-Kienitz, D. Niemann, O. Ozkan, C. Strother, and C. Mistretta. 4D Digital Subtraction Angiography: Implementation and Demonstration of Feasibility. *American Journal of Neuroradiology*, April 2013.

[3] David Niemann. 4D Omniplane Fluoroscopy: A Technique For Obtaining Unlimited Working Projections and Virtual Endoscopic Views During Endovascular Procedures, November 2015.

[4] Jonathan L. Brisman, Joon K. Song, and David W. Newell. Cerebral Aneurysms. *New England Journal of Medicine*, 355(9):928–939, August 2006.

[5] Andrew Molyneux and Richard Kerr. International Subarachnoid Aneurysm Trial (ISAT) of neurosurgical clipping versus endovascular coiling in 2143 patients with ruptured intracranial aneurysms: A randomized trial. *Journal of Stroke and Cerebrovascular Diseases*, 11(6):304–314, November 2002.

[6] C M Strother, J F Sackett, A B Crummy, F G Lilleas, W J Zwiebel, W D Turnipseed, M Javid, C A Mistretta, R A Kruger, D L Ergun, and C G Shaw. Clinical applications of computerized fluoroscopy: the extracranial carotid arteries. *Radiology*, 136(3):781–783, September 1980.

[7] C. A. Mistretta, E. Oberstar, B. Davis, E. Brodsky, and C. M. Strother. 4D-DSA and 4D fluoroscopy: preliminary implementation. volume 7622, pages 762227–762227–8. SPIE, 2010.

[8] Gabe Shaughnessy, Carson Hoffman, Sebastian Schafer, Paul Laeseke, Charles A. Mistretta, and Charles M. Strother. Precision blood flow measurements in vascular networks with conservation constraints. In *Medical Imaging 2018: Image-Guided Procedures, Robotic Interventions, and Modeling*, volume 10576, pages 644–653. SPIE, March 2018.

[9] Brian J. Davis, Martin G. Wagner, Sarvesh Periyasamy, Charles A. Mistretta, Charles M. Strother, Paul F. Laeseke, and Michael A. Speidel. Evaluation of real-time guidewire navigation using virtual

endoscopic 4D fluoroscopy. In *Medical Imaging 2020: Image-Guided Procedures, Robotic Interventions, and Modeling*, volume 11315, page 1131515. International Society for Optics and Photonics, March 2020.

[10] Charles A. Mistretta and Andrew B. Crummy. Diagnosis of Cardiovascular Disease by Digital Subtraction Angiography. *Science*, 214(4522):761–765, November 1981.

[11] R. A. Kruger, C. A. Mistretta, J. Lancaster, T. L. Houk, M. Goodsitt, C. G. Shaw, S. J. Riederer, J. Hicks, J. Sackett, A. B. Crummy, and D. Fleming. A Digital Video Image Processor for Real-Time X-Ray Subtraction Imaging. *Optical Engineering*, 17(6):176652–176652–, 1978.

[12] C. A. Mistretta, R. A. Kruger, T. L. Houk, S. J. Riederer, C. G. Shaw, D. Ergun, W. Kubal, A. B. Crummy, W. Zwiebel, G. Rowe, W. Zarnstorff, and D. Flemming. Computerized Fluoroscopy Techniques For Non-Invasive Cardiovascular Imaging. volume 0152, pages 65–71, 1978.

[13] C G Shaw, D L Ergun, P D Myerowitz, M S Van Lysel, C A Mistretta, W C Zarnstorff, and A B Crummy. A technique of scatter and glare correction for videodensitometric studies in digital subtraction videoangiography. *Radiology*, 142(1):209–213, January 1982.

[14] William D. Turnipseed, Charles A. Jistretta, Andrew B. Crummy, Charles M. Strother, Joseph F. Sackett, P. David Myerowitz, Choring G. Shaw, and David L. Ergun. Arterial imaging with computerized fluoroscopy. *Cardiovascular Diseases*, 8(3):427–434, September 1981.

[15] C. M. Strother, F. Bender, Y. Deuerling-Zheng, K. Royalty, K. A. Pulfer, J. Baumgart, M. Zellerhoff, B. Aagaard-Kienitz, D. B. Niemann, and M. L. Lindstrom. Parametric Color Coding of Digital Subtraction Angiography. *American Journal of Neuroradiology*, 31(5):919–924, May 2010.

[16] R. Fahrig, A. J. Fox, S. Lownie, and D. W. Holdsworth. Use of a C-arm system to generate true three-dimensional computed rotational angiograms: preliminary in vitro and in vivo results. *American Journal of Neuroradiology*, 18(8):1507–1514, September 1997.

[17] R. Fahrig, M. Moreau, and D. W. Holdsworth. Three-dimensional computed tomographic reconstruction using a C-arm mounted XRII: Correction of image intensifier distortion. *Medical Physics*, 24(7):1097–1106, July 1997.

[18] Robert C. Orth, Michael J. Wallace, and Michael D. Kuo. C-arm Cone-beam CT: General Principles and Technical Considerations for Use in Interventional Radiology. *Journal of Vascular and Interventional Radiology*, 19(6):814–820, June 2008.

[19] Kevin Royalty, dissertant. *4D DSA : new methods and applications for 3D time-resolved angiography for C-arm CT interventional imaging.* [Madison, Wis.] : [University of Wisconsin–Madison], 2014., 2014.

[20] M. Spiegel, T. Redel, T. Struffert, J. Hornegger, and A. Doerfler. A 2D driven 3D vessel segmentation algorithm for 3D digital subtraction angiography data. *Physics in Medicine and Biology*, 56(19):6401, 2011.

[21] W. J. van Rooij, M. E. Sprengers, A. N. de Gast, J. P. P. Peluso, and M. Sluzewski. 3D Rotational Angiography: The New Gold Standard in the Detection of Additional Intracranial Aneurysms. *American Journal of Neuroradiology*, 29(5):976–979, May 2008.

[22] Pa Turski, Mf Stieghorst, Cm Strother, Ab Crummy, Rp Lieberman, and Ca Mistretta. Digital subtraction angiography "road map". *American Journal of Roentgenology*, 139(6):1233–1234, December 1982.

[23] Nassir Navab, Ali R. Bani-Hashemi, Matthias M. Mitschke, David W. Holdsworth, Rebecca Fahrig, Allan J. Fox, and R. Graumann. Dynamic geometrical calibration for 3D cerebral angiography. volume 2708, pages 361–370, 1996.

[24] Anne Rougee, Catherine L. Picard, Yves L. Trousset, and Cyril Ponchut. Geometrical calibration for 3D x-ray imaging. volume 1897, pages 161–169, 1993.

[25] K. Wiesent, K. Barth, N. Navab, P. Durlak, T. Brunner, O. Schuetz, and W. Seissler. Enhanced 3-D-reconstruction algorithm for C-arm systems suitable for interventional procedures. *IEEE Transactions on Medical Imaging*, 19(5):391–403, May 2000.

[26] Charles A. Mistretta. Sub-Nyquist acquisition and constrained reconstruction in time resolved angiography. *Medical Physics*, 38(6):2975–2985, June 2011.

[27] A. Ganguly, A. Fieselmann, M. Marks, J. Rosenberg, J. Boese, Y. Deuerling-Zheng, M. Straka, G. Zaharchuk, R. Bammer, and R. Fahrig. Cerebral CT Perfusion Using an Interventional C-Arm Imaging System: Cerebral Blood Flow Measurements. *AJNR. American journal of neuroradiology*, 32(8):1525–1531, September 2011.

[28] Brian Davis, Erick Oberstar, Kevin Royalty, Sebastian Schafer, Charles Strother, and Charles Mistretta. Volumetric limiting spatial resolution analysis of four dimensional digital subtraction angiography (4D-DSA). In *Physics of Medical Imaging*, volume 9412, pages 94121B–94121B–10. SPIE, 2015.

[29] C. A. Mistretta, O. Wieben, J. Velikina, W. Block, J. Perry, K. Wu, Y.Johnson, and Y. Wu. Highly constrained backprojection for time-resolved MRI. *Magnetic Resonance in Medicine*, 55(1):30–40, 2006.

[30] Carolina Sandoval-Garcia, Kevin Royalty, Pengfei Yang, David Niemann, Azam Ahmed, Beverly Aagaard-Kienitz, Mustafa K. Baskaya, Sebastian Schafer, and Charles Strother. 4D DSA a new tech-

nique for arteriovenous malformation evaluation: a feasibility study. *Journal of NeuroInterventional Surgery*, pages neurintsurg–2014–011534, January 2015.

[31] Martin Wagner, Paul Laeseke, Colin Harari, Sebastian Schafer, Michael Speidel, and Charles Mistretta. Feasibility of intra-acquisition motion correction for 4D DSA reconstruction for applications in the thorax and abdomen. In *Medical Imaging 2018: Image Processing*, volume 10574, pages 285–292. SPIE, March 2018.

[32] Nils Daniel Forkert, Jens Fiehler, Till Illies, Dietmar P.F. Möller, Heinz Handels, and Dennis Säring. 4D blood flow visualization fusing 3D and 4D MRA image sequences. *Journal of Magnetic Resonance Imaging*, 36(2):443–453, 2012.

[33] Toshi Abe, Masaru Hirohata, Norimitsu Tanaka, Yusuke Uchiyama, Kazuyuki Kojima, Kiminori Fujimoto, Alexander M. Norbash, and Naofumi Hayabuchi. Clinical Benefits of Rotational 3D Angiography in Endovascular Treatment of Ruptured Cerebral Aneurysm. *American Journal of Neuroradiology*, 23(4):686–688, April 2002.

[34] Michael Söderman, D. Babic, R. Homan, and T. Andersson. 3D roadmap in neuroangiography: technique and clinical interest. *Neuroradiology*, 47(10):735–740, July 2005.

[35] Brian Davis Erick Oberstar. ASNR 2012, Presentation #: Paper 587, 4D Omni-Plane Fluoroscopy Alleviating The Problem Of Unobtainable Working Projections, 2012.

[36] L. Frank Baum and W. W Denslow. *The wonderful wizard of Oz*. G.M. Hill Co., Chicago; New York, 1900. OCLC: 9506808.

[37] Y. Peng, W. Zhao, X. Lu, and J. Shi. Research and Realization of Virtual Endoscopy. In *2010 4th International Conference on Bioinformatics and Biomedical Engineering*, pages 1–4, June 2010.

[38] Erick Oberstar. RSNA 2013 - Feasibility of 4D endoscopic rendering of interventional devices - LL-PHS-MO9B Poster Presentation, 2013.

[39] Martin Wagner, Sebastian Schafer, Charles Strother, and Charles Mistretta. 4D interventional device reconstruction from biplane fluoroscopy. *Medical Physics*, 43(3):1324–1334, March 2016.

[40] Martin Wagner, Pengfei Yang, Sebastian Schafer, Charles Strother, and Charles Mistretta. Noise reduction for curve-linear structures in real time fluoroscopy applications using directional binary masks. *Medical Physics*, 42(8):4645–4653, August 2015.

[41] Martin G. Wagner, Paul F. Laeseke, Tilman Schubert, Jordan M. Slagowski, Michael A. Speidel, and Charles A. Mistretta. Feature-based respiratory motion tracking in native fluoroscopic sequences for

dynamic roadmaps during minimally invasive procedures in the thorax and abdomen. In *Medical Imaging 2017: Image-Guided Procedures, Robotic Interventions, and Modeling*, volume 10135, pages 382–390. SPIE, March 2017.

[42] Martin G. Wagner, Charles M. Strother, Sebastian Schafer, and Charles A. Mistretta. Biplane reconstruction and visualization of virtual endoscopic and fluoroscopic views for interventional device navigation. In *Medical Imaging 2016: Image-Guided Procedures, Robotic Interventions, and Modeling*, volume 9786, page 978613. International Society for Optics and Photonics, March 2016.

[43] S.A.M. Baert, E.B. van de Kraats, T. Van Walsum, M.A. Viergever, and W.J. Niessen. Three-dimensional guide-wire reconstruction from biplane image sequences for integrated display in 3-D vasculature. *IEEE Transactions on Medical Imaging*, 22(10):1252–1258, October 2003.

[44] H.-J. Bender, R. Männer, C. Poliwoda, S. Roth, and M. Walz. Reconstruction of 3D Catheter Paths from 2D X-ray Projections. In Chris Taylor and Alain Colchester, editors, *Medical Image Computing and Computer-Assisted Intervention - MICCAI 99*, number 1679 in Lecture Notes in Computer Science, pages 981–989. Springer Berlin Heidelberg, September 1999.

[45] Raja N. Ghanem, Charulatha Ramanathan, Ping Jia, and Yoram Rudy. Heart-Surface Reconstruction and ECG Electrodes Localization Using Fluoroscopy, Epipolar Geometry and Stereovision: Application to Noninvasive Imaging of Cardiac Electrical Activity. *IEEE transactions on medical imaging*, 22(10):1307–1318, October 2003.

[46] Matthias Hoffmann, Alexander Brost, Carolin Jakob, Martin Koch, Felix Bourier, Klaus Kurzidim, Joachim Hornegger, and Norbert Strobel. Reconstruction method for curvilinear structures from two views. page 86712F, March 2013.

[47] Kevin T. Foley, David A. Simon, and Y. Raja Rampersaud. Virtual fluoroscopy: computer-assisted fluoroscopic navigation. *Spine*, 26(4):347–351, 2001.

[48] Alexander R Vaccaro, Philip S Yuan, Harvey E Smith, Jonathon Hott, Rick Sasso, and Stephen Papadopoulos. An Evaluation of Image-Guided Technologies in the Placement of Anterior Thoracic Vertebral Body Screws in Spinal Trauma: A Cadaver Study. *The Journal of Spinal Cord Medicine*, 28(4):308–313, 2005.

[49] Yu-Po Lee, C. Max Hoshino, and Choll W. Kim. Virtual Fluoroscopy. *Seminars in Spine Surgery*, 20(3):195–202, September 2008.

[50] Lichan Hong, Shigeru Muraki, Arie Kaufman, Dirk Bartz, and Taosong He. Virtual voyage: interactive

navigation in the human colon. In *Proceedings of the 24th annual conference on Computer graphics and interactive techniques - SIGGRAPH '97*, pages 27–34, Not Known, 1997. ACM Press.

[51] Y. Peng, Y. Wang, and J. Shi. Research on Key Technologies of Virtual Endoscopy. In *2010 International Conference on Biomedical Engineering and Computer Science*, pages 1–4, April 2010.

[52] Y. Peng, W. Zhao, X. Lu, and J. Shi. Research on Virtual Endoscopy System. In *2009 Fifth International Conference on Image and Graphics*, pages 602–607, September 2009.

[53] Li-Ping Yao, Ju Mei, Fang-Bao Ding, Li Zhang, Hui-Ming Li, Ming Ding, Xin Yang, Xiao-Ming Li, and Kun Sun. Application of cardiovascular virtual endoscopy: a pilot study on roaming path planning for diagnosis of congenital heart diseases in children. *Scientific Reports*, 8(1):1424, January 2018.

[54] Li-Ping Yao, Li Zhang, Ju Mei, Fang-Bao Ding, Hui-Ming Li, Ming Ding, Xin Yang, Xiao-Ming Li, and Kun Sun. A pilot study of a cardiovascular virtual endoscopy system based on multi-detector computed tomography in diagnosing tetralogy of Fallot in pediatric patients. *Experimental and Therapeutic Medicine*, 15(2):1552–1559, February 2018.

[55] A.D. Copeland, R.S. Mangoubi, M.N. Desai, S.K. Mitter, and A.M. Malek. Spatio-Temporal Data Fusion for 3D+T Image Reconstruction in Cerebral Angiography. *IEEE Transactions on Medical Imaging*, 29(6):1238–1251, June 2010.

[56] H. Schmitt, M. Grass, V. Rasche, O. Schramm, S. Haehnel, and K. Sartor. An X-ray-based method for the determination of the contrast agent propagation in 3-D vessel structures. *IEEE Transactions on Medical Imaging*, 21(3):251–262, March 2002.

[57] Holger Schmitt, Michael Grass, Rolf Suurmond, Thomas Köhler, Volker Rasche, Stefan Hähnel, and Sabine Heiland. Reconstruction of blood propagation in three-dimensional rotational X-ray angiography (3D-RA). *Computerized Medical Imaging and Graphics*, 29(7):507–520, October 2005.

[58] Karl Wiesent, Ali R. Bani-Hashemi, and Nassir Navab. X-ray imaging system, March 2000.

[59] R. R Galigekere, K. Wiesent, and D. W Holdsworth. Cone-beam reprojection using projection-matrices. *IEEE Transactions on Medical Imaging*, 22(10):1202–1214, October 2003.

[60] Jared Hoberock and Nathan Bell. Thrust - C++ Template Library of Parallel Algorithms.

[61] Holger Scherl, Markus Kowarschik, Hannes G. Hofmann, Benjamin Keck, and Joachim Hornegger. Evaluation of state-of-the-art hardware architectures for fast cone-beam CT reconstruction. *Parallel Computing*, 38(3):111–124, March 2012.

[62] Willi A Kalender. Computed Tomography: Fundamentals, System Technology, Image Quality, Applications, November 2000.

[63] E. L. Nickoloff. Measurement of the PSF for a CT scanner: appropriate wire diameter and pixel size. *Physics in Medicine and Biology*, 33(1):149, January 1988.

[64] C. J. Bischof and J. C. Ehrhardt. Modulation transfer function of the EMI CT head scanner. *Medical Physics*, 4(2):163–167, 1977.

[65] David A. P. Dunkerley. *Development of a 3D Device Guidance Platform for the Scanning-Beam Digital X-Ray (SBDX) System*. Ph.D., The University of Wisconsin - Madison, United States – Wisconsin, 2017.

[66] Reiza Rayman, Serguei Primak, Rajni Patel, Merhdad Moallem, Roya Morady, Mahdi Tavakoli, Vanja Subotic, Natalie Galbraith, Aimee van Wynsberghe, and Kris Croome. Effects of Latency on Telesurgery: An Experimental Study. In David Hutchison, Takeo Kanade, Josef Kittler, Jon M. Kleinberg, Friedemann Mattern, John C. Mitchell, Moni Naor, Oscar Nierstrasz, C. Pandu Rangan, Bernhard Steffen, Madhu Sudan, Demetri Terzopoulos, Dough Tygar, Moshe Y. Vardi, Gerhard Weikum, James S. Duncan, and Guido Gerig, editors, *Medical Image Computing and Computer-Assisted Intervention – MICCAI 2005*, volume 3750, pages 57–64. Springer Berlin Heidelberg, Berlin, Heidelberg, 2005.

[67] Shan Zhu and Kai-Kuang Ma. A new diamond search algorithm for fast block-matching motion estimation. *IEEE Transactions on Image Processing*, 9(2):287–290, February 2000.

[68] William E. Lorensen and Harvey E. Cline. Marching Cubes: A High Resolution 3D Surface Construction Algorithm. In *Proceedings of the 14th Annual Conference on Computer Graphics and Interactive Techniques*, SIGGRAPH '87, pages 163–169, New York, NY, USA, 1987. ACM.

[69] T. C. Lee, R. L. Kashyap, and C. N. Chu. Building Skeleton Models via 3-D Medial Surface Axis Thinning Algorithms. *CVGIP: Graphical Models and Image Processing*, 56(6):462–478, November 1994.

[70] Michael Kerschnitzki, Philip Kollmannsberger, Manfred Burghammer, Georg N Duda, Richard Weinkamer, Wolfgang Wagermaier, and Peter Fratzl. Architecture of the osteocyte network correlates with bone material quality. *Journal of Bone and Mineral Research*, 28(8):1837–1845, August 2013.

[71] Nikhil Gagvani and Deborah Silver. Parameter-Controlled Volume Thinning. *Graphical Models and Image Processing*, 61(3):149–164, May 1999.

[72] Luca Antiga. Patient-specific modeling of geometry and blood flow in large arteries. *Politecnico di Milano*, 2002.

[73] Martin G. Wagner. Real-time thinning algorithms for 2D and 3D images using GPU processors. *Journal of Real-Time Image Processing*, May 2019.

[74] Giovanni Mauri, Luca Cova, Stefano De Beni, Tiziana Ierace, Tania Tondolo, Anna Cerri, S. Nahum Goldberg, and Luigi Solbiati. Real-Time US-CT/MRI Image Fusion for Guidance of Thermal Ablation of Liver Tumors Undetectable with US: Results in 295 Cases. *CardioVascular and Interventional Radiology*, 38(1):143–151, February 2015.

[75] Susan Jamieson. Likert scales: how to (ab)use them. *Medical Education*, 38(12):1217–1218, December 2004.

[76] Christoph Baur, Fausto Milletari, Vasileios Belagiannis, Nassir Navab, and Pascal Fallavollita. Automatic 3D reconstruction of electrophysiology catheters from two-view monoplane C-arm image sequences. *International Journal of Computer Assisted Radiology and Surgery*, 11(7):1319–1328, July 2016.

[77] Matthias Hoffmann, Alexander Brost, Martin Koch, Felix Bourier, Andreas Maier, Klaus Kurzidim, Norbert Strobel, and Joachim Hornegger. Electrophysiology Catheter Detection and Reconstruction From Two Views in Fluoroscopic Images. *IEEE Transactions on Medical Imaging*, 35(2):567–579, February 2016. Conference Name: IEEE Transactions on Medical Imaging.

[78] Alfonso Fiorelli, Antonio Raucci, Roberto Cascone, Alfonso Reginelli, Davide Di Natale, Carlo Santoriello, Antonio Capuozzo, Roberto Grassi, Nicola Serra, Mario Polverino, and Mario Santini. Three-dimensional virtual bronchoscopy using a tablet computer to guide real-time transbronchial needle aspiration. *Interactive CardioVascular and Thoracic Surgery*, 24(4):567–575, April 2017. Publisher: Oxford Academic.

[79] Jay D. Patel and Kevin J. Chang. The role of virtual colonoscopy in colorectal screening. *Clinical Imaging*, 40(2):315–320, March 2016.

[80] Y. Wu, G. Shaughnessy, C. A. Hoffman, E. L. Oberstar, S. Schafer, T. Schubert, K. L. Ruedinger, B. J. Davis, C. A. Mistretta, C. M. Strother, and M. A. Speidel. Quantification of Blood Velocity with 4D Digital Subtraction Angiography Using the Shifted Least-Squares Method. *American Journal of Neuroradiology*, September 2018.

[81] Ece Meram, Colin Harari, Gabe Shaughnessy, Martin Wagner, Chris L. Brace, Charles A. Mistretta, Michael A. Speidel, and Paul F. Laeseke. Quantitative 4D-Digital Subtraction Angiography to Assess Changes in Hepatic Arterial Flow during Transarterial Embolization: A Feasibility Study in a Swine Model. *Journal of Vascular and Interventional Radiology*, 30(8):1286–1292, August 2019.

[82] Sarvesh Periyasamy, Carson A. Hoffman, Colin Longhurst, Georgia C. Schefelker, Orhan S. Ozkan, Michael A. Speidel, and Paul F. Laeseke. A Quantitative Digital Subtraction Angiography Technique for Characterizing Reduction in Hepatic Arterial Blood Flow During Transarterial Embolization. *CardioVascular and Interventional Radiology*, 44(2):310–317, February 2021.

[83] Carson Hoffman, Sarvesh Periyasamy, Colin Longhurst, Rafael Medero, Alejandro Roldan-Alzate, Michael A. Speidel, and Paul F. Laeseke. A technique for intra-procedural blood velocity quantitation using time-resolved 2D digital subtraction angiography. *CVIR Endovascular*, 4(1):11, December 2021.

[84] Joseph F. Whitehead, Carson A. Hoffman, Martin G. Wagner, Grace M. Minesinger, Ethan P. Nikolau, Paul F. Laeseke, and Michael A. Speidel. Interleaved x-ray imaging: A method for simultaneous acquisition of quantitative and diagnostic digital subtraction angiography. *Medical Physics*, n/a(n/a), September 2023. _eprint: https://onlinelibrary.wiley.com/doi/pdf/10.1002/mp.16794.